ΠΑΝΕΠΙΣΤΗΜΙΟ ΚΡΗΤΗΣ

ΤΜΗΜΑ ΧΗΜΕΙΑΣ

ΓΕΝΙΚΟ ΜΕΤΑΠΤΥΧΙΑΚΟ ΠΡΟΓΡΑΜΜΑ ΧΗΜΕΙΑΣ

ΕΡΓΑΣΤΗΡΙΟ ΧΗΜΙΚΗΣ ΔΥΝΑΜΙΚΗΣ

ΜΕΤΑΠΤΥΧΙΑΚΟ ΔΙΠΛΩΜΑ ΕΙΔΙΚΕΥΣΗΣ

ΜΕΛΕΤΗ ΤΗΣ ΔΥΝΑΜΙΚΗΣ ΦΩΤΟΔΙΕΓΕΡΣΗΣ ΜΙΚΡΩΝ ΜΟΡΙΩΝ ΣΕ ΥΨΗΛΕΣ ΕΝΕΡΓΕΙΕΣ

Κουμαριανού Γεωργία

Υπεύθυνος Καθηγητής: Θεοφάνης Κιτσόπουλος

ΗΡΑΚΛΕΙΟ 2018

UNIVERSITY OF CRETE
DEPARTMENT OF CHEMISTRY

GENERAL GRADUATE PROGRAM IN CHEMISTRY

CHEMICAL DYNAMICS LAB

Master Thesis

HIGH-ENERGY PHOTOEXCITATION DYNAMICS OF SMALL MOLECULES

GEORGIA KOUMARIANOU

Master Thesis Supervisor: Theofanis Kitsopoulos

HERAKLION 2018

Εξεταστική Επιτροπή (αλφαβητικά)

Δημήτριος Άγγλος
Καθηγητής Τμήματος Χημείας, Πανεπιστήμιο Κρήτης

Θεοφάνης Κιτσόπουλος(Επιβλέπων)
Καθηγητής Τμήματος Χημείας, Πανεπιστήμιο Κρήτης

Πέτρος Σαμαρτζής
Ερευνητής Γ, ΙΗΔΛ-ΙΤΕ

ΒΙΟΓΡΑΦΙΚΟ ΣΗΜΕΙΩΜΑ

Κουμαριανού Γεωργία (Γκρέτα)

Γενικές Πληροφορίες

Διεύθυνση Ηλ.Ταχυδρομείου: gr.koumarianou@gmail.com

Τηλέφωνο: +306955484299

Skype ID: greta.koumarianou

Εκπαίδευση

2016-σήμερα | Μεταπτυχιακό Δίπλωμα Ειδίκευσης στη Χημεία (Τομέας Φυσικοχημείας) , *Πανεπιστήμιο Κρήτης*

2012-2016 | Πτυχίο Χημείας , *Πανεπιστήμιο Κρήτης*

2009-2012 | Γενικό Λύκειο Μυκόνου, Κυκλάδες

Ερευνητική Εμπειρία

2016-σήμερα | Εργαστήριο Χημικής Δυναμικής στο Ινστιτούτο Ηλεκτρονικής Δομής και Λέιζερ –Ίδρυμα Τεχνολογίας και Έρευνας (ΙΤΕ), **Υπεύθυνος Καθηγητής: Θεοφάνης Κιτσόπουλος**

2014 - 2016 | Εργαστήριο Χημικής Δυναμικής στο Ινστιτούτο Ηλεκτρονικής Δομής και Λέιζερ –Ίδρυμα Τεχνολογίας και Έρευνας (ΙΤΕ)**, Υπεύθυνος Καθηγητής: Θεοφάνης Κιτσόπουλος**

Τίτλος Διπλωματικής Εργασίας : Μελέτη της φωτοδιάσπασης του CH_3NO_2 *στο υπεριώδες με την τεχνική απεικόνισης ιόντων .*

Πειραματικές Δεξιότητες

- Συστήματα Λέιζερ (λέιζερ διεγερμένων διμερών, χρωστικών, Nd: YAG, διόδων , διατάξεις OPO)
- Μέθοδοι Δημιουργίας Κενού
- Τεχνικές Απεικόνισης Ιόντων
- Μηχανικό Σχέδιο

Διδακτική Εμπειρία

Σεπτέμβριος– Δεκέμβριος (2016)

Βοηθός στο Προπτυχιακό Εργαστήριο Φυσικοχημείας Ι (Ατομική Φασματοσκοπία)

Ιανουάριος-Ιούνιος (2017)

Βοηθός στο Προπτυχιακό Εργαστήριο Φυσικοχημείας ΙΙ (Χημική Ισορροπία-Διαγράμματα Φάσεων, Ιξώδες)

Δημοσιεύσεις

1.D. Sofikitis, P. Glodic, G. Koumarianou, H. Jiang, L. Bougas, P.C. Samartzis, A. Andreev, and T.P. Rakitzis, Highly Nuclear-Spin-Polarized Deuterium Atoms from the UV Photodissociation of Deuterium Iodide.*Phys. Rev. Lett*. 2017,118, 233401.

2.Hafliðason, A.; Glodic, P.; Koumarianou, G.; Samartzis, P.; Kvaran, Á. Multiphoton Rydberg And Valence Dynamics of CH_3Br Probed by Mass Spectrometry And Slice Imaging.*Physical Chemistry Chemical Physics,20*, 17423-17433.

Επιπρόσθετες Πληροφορίες

Γλώσσες: Ελληνικά, Αγγλικά (Cambridge and Michigan PE, IELTS:8), Γαλλικά(DELF-B2)

Υπολογιστικές Δεξιότητες: OriginLab Software, LabView, Gaussian (Computational Chemistry software), Fortran

Εθελοντισμός: TEDxHeraklion (2015), Παρουσιάσεις πειραμάτων Χημείας σε τοπικά σχολεία (2016)

Αναφορές

1. **Πέτρος Σαμαρτζής**

Ερευνητής Γ στο ΙΗΔΛ-ΙΤΕ.

Email: sama@iesl.forth.gr

2.**Θεοφάνης Κιτσόπουλος**

Καθηγητής, Τμήμα Χημείας ,Πανεπιστήμιο Κρήτης

Email: theo@iesl.forth.gr

3. **Δημήτριος Άγγλος**

Καθηγητής, Τμήμα Χημείας, Πανεπιστήμιο Κρήτης

Email: anglos@iesl.forth.gr

CURRICULUM VITAE

Georgia (Greta) Koumarianou

PERSONAL INFORMATION

Email gr.koumarianou@gmail.com

Phone +306955484299

Skype ID : greta.koumarianou

EDUCATION

2016-present | MSc of Chemistry (Physical Chemistry), *University of Crete*, Greece

2012-2016 | BSc of Chemistry, *University of Crete*, Greece

2009-2012 | High School of Mykonos, Cyclades, Greece

RESEARCH EXPERIENCE

2016-present | Chemical Dynamics Lab at the Institute of Electronic Structure & Laser (IESL) Foundation for Research Hellas (FORTH), Supervisor: Prof. Theofanis Kitsopoulos.

2014 - 2016 | Chemical Dynamics Lab at IESL-FORTH with Prof. Theofanis Kitsopoulos.

Bachelor Diploma Thesis:

Study of CH_3NO_2 photodissociation in UV using the ion imaging technique.

OVERVIEW OF EXPERIMENTAL SKILLS

- Laser systems (Excimers, Dye lasers, Nd: YAG, diode lasers, OPO setups)

- High Vacuum Generation Methods

- Ion imaging techniques

- Mechanical Design

TEACHING EXPERIENCE

September 2016- December 2016

TA in Physical Chemistry Undergraduate Lab I (Atomic Spectroscopy)

January 2017 – June 2017

TA in Physical Chemistry Undergraduate Lab II(Chemical Equilibrium, Phase Diagrams, Viscosity)

PUBLICATIONS

1.D. Sofikitis, P. Glodic, G. Koumarianou, H. Jiang, L. Bougas, P.C. Samartzis, A. Andreev, and T.P. Rakitzis, Highly Nuclear-Spin-Polarized Deuterium Atoms from the UV Photodissociation of Deuterium Iodide.*Phys. Rev. Lett*. 2017,118, 233401.

2.Hafliðason, A.; Glodic, P.; Koumarianou, G.; Samartzis, P.; Kvaran, Á. Multiphoton Rydberg And Valence Dynamics of CH_3Br Probed By Mass Spectrometry And Slice Imaging.*Physical Chemistry Chemical Physics*,*20*, 17423-17433.

OTHER INFORMATION

Languages: Greek (Native) , English (Cambridge and Michigan PE, IELTS:8) , French (DELF-B2)

Computer Skills: OriginLab Software, LabView, Gaussian (Computational Chemistry software) ,Fortran programming language, MATLAB

Volunteering Work: TEDxHeraklion volunteer (2015), Chemistry Demonstrations in local schools (2016)

REFERENCES

1. **Petros C. Samartzis**

Researcher at IESL-FORTH, Greece

Email: sama@iesl.forth.gr

2.**Theofanis Kitsopoulos**

Professor,Department of Chemistry, University of Crete, Greece
Email: theo@iesl.forth.gr

3. **Demetrios Anglos**

Professor, Department of Chemistry, University of Crete, Greece
Email: anglos@iesl.forth.gr

Περίληψη

Η παρούσα μεταπτυχιακή διατριβή περιλαμβάνει πειράματα κατά τα οποία μελετήθηκε η δυναμική αντιδράσεων φωτοδιάσπασης μικρών μορίων σε υψηλές ενέργειες. Διερευνήθηκαν τρία διαφορετικά συστήματα μικρών μοριών που περιέχουν ένα άτομο αλογόνου: το ιωδομεθάνιο (CH_3I), το βρωμομεθάνιο (CH_3Br) και το δευτεριωμένο υδροιώδιο(DI). Το κίνητρο για την παραπάνω έρευνα ήταν η επέκταση της γνώσης για τη δυναμική φωτοδιάσπασης σε αυτές τις ενέργειες, και πιο συγκεκριμένα η ταυτοποίηση των κβαντικών καταστάσεων των προιόντων αλλα και των ενεργών καναλιών φωτοδιάσπασης από τα οποία παράγονται. Με βάση τα παραπάνω δεδομένα, πιθανοί μηχανισμοί για την κάθε αντίδραση μπορούν να προταθούν.

Στο πρώτο Κεφάλαιο, γίνεται μια σύντομη περιγραφή της θεωρίας και των πειραματικών τεχνικών που είναι απαραίτητες για την κατανόηση των πειραμάτων που περιγράφονται στα επόμενα κεφάλαια. Συγκεκριμένα,ο αναγνώστης εισαγάγεται στον τομέα της Δυναμικής Αντιδράσεων και στη βασική περιγραφή των αντιδράσεων φωτοδιάσπασης. Τα μόρια προς ανάλυση διεγείρονται σε υψηλά διεγερμένες καταστάσεις ,κατ'επέκταση γίνεται μια εισαγωγή στις μοριακές ηλεκτρονιακές καταστάσεις με έμφαση στις υψηλά ενεργειακές καταστάσεις Rydberg.Στη συνέχεια, περιγράφονται λεπτομερώς η μέθοδος απεικόνισης ιόντων , η πειραματική διαδικασία και η ανάλυση των δεδομένων.

Στο δεύτερο Κεφάλαιο, παρουσιάζονται τα δεδομένα από τη μελέτη της δυναμικής φωτοδιάσπασης του μεθυλοβρωμιδίου (CH_3Br) έπειτα από διέγερση σε υψηλά διεγερμένες Rydberg καταστάσεις χρησιμοποιώντας την τεχνική Απεικόνισης Ιόντων. Αναλύονται εικόνες ιόντων και φωτοηλεκτρονίων έπειτα από διέγερση σε δέκα διαφορετικές καταστάσεις Rydberg από τις οποίες ταυτοποιούνται τα προιόντα και τα πιθανά ενεργά κανάλια και προτείνεται ένας πιθανός μηχανισμός φωτοδιάσπασης.

Στο τρίτο Κεφάλαιο, αναλύεται μία παρόμοια μελέτη κατά την οποία μελετήθηκε η δυναμική φωτοδιάσπασης του μεθυλοιωδίου (CH_3I) έπειτα από διέγερση σε υψηλές καταστάσεις Rydberg. Παρουσιάζονται εικόνες ιόντων και φωτοηλεκτρονιων από τις οποίες ταυτοποιούνται τα προιόντα φωτοδιάσπασης. Στο τέλος, προτείνονται πιθανοί μηχανισμοί φωτοδιάσπασης και πραγματοποιείται σύγκριση των αποτελεσμάτων με τα αντίστοιχα για το μόριο του μεθυλοβρωμιδίου.

Τέλος, στο κεφάλαιο 4, περιγράφεται η μελέτη της φωτοδιάσπασης του δευτεριωμένου υδροιωδίου και παρουσιάζονται δεδομένα που αποδεικνύουν ότι η φωτοδιάσπαση του DI στα 270 nm με κυκλικά πολωμένο φως μπορεί να λειτουργήσει ως πηγή υπερπολωμένου D σε τιμές αριθμητικής πυκνότητας ικανοποιητικές γα εφαρμογή σε αντιδράσεις πυρηνικές σύντηξης με δευτέριο.

Abstract

This Master thesis investigates the Photodissociation Dynamics of small molecules in high energies (the Rydberg state regime). Three different molecular systems were analyzed containing one halogen atom: methyl iodine (CH_3I), methyl bromide (CH_3Br) and deuterium iodide (DI). The goal of these experiments was the extension of knowledge on high energy dynamics and more specifically the identification of the quantum states of the products and the active photodissociation channels from which they are produced. Based on these data, information on possible mechanisms for each reaction were extracted.

Chapter I serves to provide a brief introduction of the theory and the experimental methods necessary for the understanding of the experiments described in the following chapters. Specifically, the reader is introduced to the field of Reaction Dynamics and the concept of photodissociation. Moreover, since the research focuses on high energy states, an outline of the molecular electronic states and the concept of the Rydberg states is presented. Finally, a detailed illustration of the Ion Imaging technique including the experimental apparatus and the image analysis is provided.

In the second chapter, data from the study of photodissociation dynamics of CH_3Br after excitation to selected Rydberg states using the Ion Imaging technique are presented and discussed. Images from the ion products and the respective photoelectrons after their ionization are analyzed after excitation to ten different states. For each state, the quantum states of the products are identified and potential dissociation channels and underlying dissociation mechanisms are suggested.

In the third part of this thesis, the data from a similar study on the photodissociation dynamics of CH_3I after excitation to selected Rydberg states are presented and analyzed. Ion and photoelectron images were recorded and the quantum states of the products are identified along with potential dissociation channels and the underlying dissociation mechanisms are suggested. In the end, the results are compared with the ones from CH_3Br.

In the last chapter, data from the DI photodissociation are presented as evidence that DI photodissociation at 270 nm with circularly polarized light can be used as a source of high nuclear spin polarized D atoms in number densities high enough for nuclear fusion reaction applications.

Table of Contents

1 Introduction

1.1 Photodissociation Dynamics

In the heart of Physical Chemistry lies the field of Reaction Dynamics, which investigates the forces that govern chemical reactions.[1] This thesis focuses on the dynamics of photodissociation reactions, where a molecule absorbs n photons (n>=1) and bond rupture occurs, leading to products referred to as photoproducts (Eq. (1)):

$$AB + nhv \rightarrow A + B \qquad (1)$$

Identifying key parameters of this process, such as what molecular states of AB molecule are involved, in which quantum states the photoproducts A and B are and how these are related to the energy and the number of the photons absorbed, provides fundamental insight into how molecules interact with light, and specific details on how energy is redistributed within a molecule after photoexcitation.

All this information is represented in a Potential Energy Surface (PES): a model representation of the potential energy of the molecule as a function of its intermolecular coordinates. The PES is essentially a map of the chemical reaction in detail. Bound electronic states are represented on the PES as lines with a well (see red and black lines in Fig. 1 below).

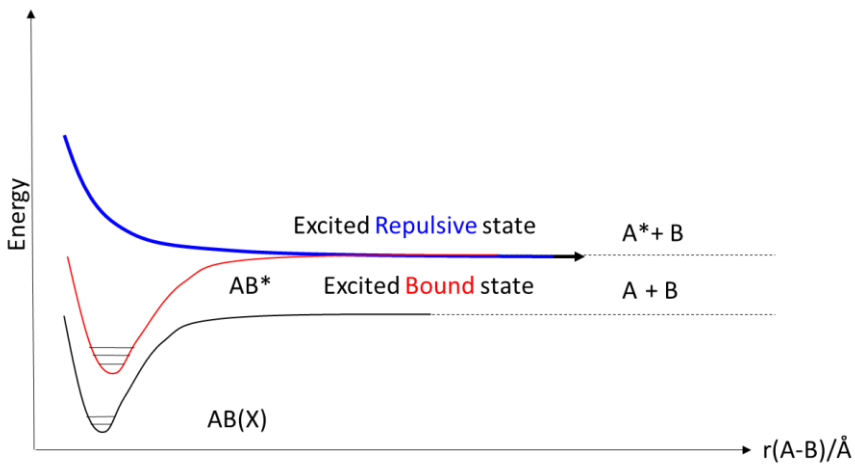

Figure 1.1: Schematic representation of a PES for a diatomic molecule A-B consisting of the ground state (black line), an excited bound state (red line) and an excited repulsive state (blue line).

Horizontal lines within the well represent vibrational and rotational energy levels of the molecule. Repulsive (unbound) states are represented with repulsive potentials (lines with no minima). In a photodissociation process a photon excites the ground state X of the molecule to a repulsive state, or –for a bound state- to the resulsive wall above the dissociation limit. In this excited state, the molecule is unstable and bond rupture occurs.[2]

1.2 Notation for Molecular Electronic States

Before we begin a much more detailed discussion about molecular transitions leading to photodissociation, the notation describing molecular states should be introduced. The simplest case is the description of states in a diatomic (or a linear polyatomic) molecule.

A molecular term symbol outlines the three main types of angular momentum: a) the spin of the electrons S, b) the orbital angular momentum Λ, and c) the total angular momentum Ω as predicted by Russel-Saunders coupling, along with some symmetry properties deduced from Group Theory.[3] In some cases, the spin of the nucleus I is included. The general formula of a molecular term symbol is given below:

$$^{2S+1}\Lambda^{(+/-)}_{\Omega,(g/u)} \quad (2)$$

whereas, specifically:

- S is the electron spin, and the term (2S+1) is the spin multiplicity.
- Λ ≡ | ML| is the projection of orbital angular momentum along z (internuclear axis). The greek letters Π, Δ, Φ, … are used for Λ=0,1,2,…,respectively.
- Ω is the projection of the total angular momentum along z; Ω≡|Λ+ S|.
- g/u describes the parity, whether an orbital is symmetric or antisymmetric after the operation of inversion, therefore it is only relevant for molecules with a center of symmetry, and
- +/- indicates whether symmetry is sustained or not upon reflection along an arbitrary plane containing the z-axis for Σ states (Λ=0).

The ground state of the molecule is usually denoted with the letter X. For the description of excited states with the same multiplicity as the ground state the letters A, B,

C,..are used as a prefix to the term. If the multiplicity is different, lowercase letters a, b, c are prefixed instead.[4]

1.3 Highly Excited States

The majority of photodissociation dynamics studies in the literature explore excited states close in energy (5-6 eV) to the ground electronic state of the molecule. When excitation energy gets higher than that (but still lower than the ionization limit), additional excited states such as Rydberg, ion pair and high-energy valence states become accessible.

Rydberg states in atoms are defined as electronically excited states derived by exciting one of the electrons into an orbital with a principal quantum number n larger than that of the valence shell.[5] Rydberg states resemble the states of the hydrogen atom in a relationship summarized by the Rydberg formula (Eq. 3), which describes the convergence of the Rydberg series in many-electron atoms to their ionization energies (IE):2

$$E_{ex} = IE - \frac{Ryd}{(n-\delta)^2} \quad (3)$$

where E_{ex} is the excitation energy of the Rydberg state (in eV), Ryd is the ionization energy of H (13.61 eV), n is the principal quantum number and δ is the quantum defect parameter accounting for the penetration of the excited Rydberg electron to the cation core.

Molecular Rydberg states are excited states in which the excited electrons occupy diffuse (Rydberg) orbitals. In conjunction with the atomic Rydberg states, a molecular Rydberg state can be thought of as the energy configuration where an electron is weakly bound to the rest of the molecular core. The Rydberg formula can still be used satisfactorily for assigning excited states in molecules, even though the core is not spherically symmetric. For this reason, assigning s, p, d character to a molecular Rydberg state is an approximation only valid in specific cases.[6]

The notation used for the description of molecular Rydberg states is the following:

$$[\Omega_c]nl; \omega, (v_i, \dots) \ (4)$$

where,

- Ω_c is the total angular momentum of the molecular core
- nl the principal quantum number and the azimuthal quantum number of the orbital of the Rydberg electron, and
- v_i refers to vibrational normal modes like v_1 = symmetric stretch.

Not all highly-excited states of an AB molecule are of Rydberg nature. Valence (bound) or repulsive states exist that could end up (upon dissociation) to ion pair formation:

$AB + nhv \rightarrow A^+ + B^-$

In addition, other valence or repulsive states may end up to electronically excited neutral photoproducts:

$AB + nhv \rightarrow A^{**} + B$

$AB + nhv \rightarrow A + B^{**}$

It is known that at high energies, the density of states increases, raising spectral complexity due to state-to-state interactions. Manifestation of Rydberg to Rydberg and valence to Rydberg interactions enriches the photochemical behavior of a molecular system making the study of its photolysis in high energy regimes a fruitful domain of high interest. Processes like predissociation and autoionization can take place, in addition to the direct photolysis channels through repulsive states.[7] Excitation to states close to or even above the ionization potential may also display interesting behavior.

One could examine exactly how the state mingling influences photolytic paths, defining the states and ratios of the final photoproducts. Namely, state interactions can affect the shape of the PES in numerous ways altering its electronic properties (e.g. coupling to other states). These interactions can give rise to multiple minima across the dissociation coordinate via avoided crossings or conical intersections that could couple the transition dipole moment of dissociative states to specific geometries.[8] For example, coupling can be affected via a vibrational excitation between states of different symmetry, a transition otherwise considered as forbidden. These types of coupling can be easily monitored with techniques like Ion Imaging, which can resolve

vibrational spectral features, as in the case of vibrational autoionization thoroughly reviewed by Pratt.[9]

1.4 Reaction Product Imaging techniques

As mentioned in the previous sections, mapping and understanding the PESs is the main task of Reaction Dynamics. Experimentally, we "access" the PES in two ways: (a) by controlling the excitation of the "reactant" molecule, thus determining what excited states it can reach and (b) by measuring the kinetic and internal energy as well as the spatial distribution of the reaction (in our case: photolysis) products.

Reaction product imaging techniques combine molecular beams, laser excitation and ionization, time-of-flight (TOF) mass spectrometry and position-sensitive detection/imaging to measure kinetic energy and angular distribution of quantum-state-selected reaction photoproducts. In the next sections we examine how that works.

1.4.1 Molecular Beams

It is essential to have well defined conditions (in position and energy) for the reactant molecules in order to evaluate the results of their interaction with light during a photodissociation event. Molecular Beams are used to ensure that the parent molecules are prepared in a known quantum state or a small number of quantum states. This is achieved by cooling the target molecules at a low temperature (several Kelvins) in a collissionless environment. Target molecules are seeded into an inert carrier gas and are expanded through a nozzle into a vacuum chamber. After the nozzle, a skimmer is placed to collimate the initial divergent beam. The expansion of the gas proceeds adiabatically resulting in a cold molecular beam.

During the expansion through the nozzle, energy transfer occurs between the gas molecules through collisions. However, right after the nozzle there is a zone called 'silent zone' where molecules travel in supersonic speeds (faster than the speed of sound) in a parallel manner (no collisions). These are the ideal conditions of the beam and they are maintained if the skimmer is placed inside the silent zone.[10]

Creating a supersonic molecular beam means that the reactant molecules are prepared in their ground electronic and vibrational states, with only the lower few rotational

states being populated. Vibrational cooling happens in a lesser extent because the spacing between adjacent lowlying vibrational levels is usually bigger than the collision energy of the expanding molecules. Under no cluster formation conditions, the final velocity of the molecular beam is determined by the mass of the carrier gas molecules.[11]

1.4.2 Photodissociation energetics

A laser photodissociates the target molecules AB in the molecular beam and atomic or molecular photofragments A, B are produced:

$$AB + nhv \rightarrow AB^{*} \rightarrow A + B \ (5)$$

Because the reactant molecule is prepared in its ground electronic state, in the molecular beam (or at least in a state that is known for all the molecules in the sample before dissociation), the states of the product fragments can be deduced.

From energy conservation, it follows that the total kinetic energy release (TKER) of the fragments will be equal to:

$$TKER = T_A + T_B = nhv - D_o(AB) - E_{int}(A) - E_{int}(B) \ \ (6)$$

Where hv the photon energy, n the number of photons, D_o the bond dissociation energy and E_{int} each fragment's internal energy (electronic or rovibrational).

The laser-molecular beam interaction point defines the origin of the photofragments, working in the center of mass frame, momentum conservation, in the simplest case where AB thermal motion is neglected, dictates the following equation (where u_A and u_B are vectors):

$$m_A \boldsymbol{u_A} + m_B \boldsymbol{u_B} = m_{AB} \boldsymbol{u_{AB}} = 0 \ \ (7)$$

The following relationship about each photofragment's translational energy can be derived from Eq. (7):

$$T_A = \frac{m_B}{M} TKER \ \ and \ \ T_B = \frac{m_A}{M} TKER \ (8)$$

$$where \ M = m_A + m_B, \mathrm{T_A} = \frac{1}{2} \mathrm{m_A u_A^2} \ and \ \mathrm{T_B} = \frac{1}{2} \mathrm{m_B u_B^2}$$

Thus from eqs. 6 and 8, we conclude that if fragment A is produced in a known quantum state and we measure its kinetic energy T_A we can calculate the kinetic energy

(T_B) and internal energy E_{int}(B) of its counterfragment B. Imaging all quantum states of A provides info on all states of their counterfragments B.

It is also important to note that fragments A of the same quantum state have the same kinetic energy release $T_A=1/2m_Au_A^{2,}$ therefore at any given time t after the photolysis they will lay on the surface of a sphere of radius $r=u_A*t$, where u_A is the center of mass velocity that A obtained from the photolysis event. This sphere is called Newton sphere. Fragments A of a different quantum state will be on another Newton sphere with different radius but with the same center (concentric Newton spheres). The center of the Newton spheres is the area in space where the laser photolyzed the parent molecule A-B.

Newton sphere characteristics such as size and surface ion distribution pattern, provide valuable information regarding the dissociation process. The size of the Newton sphere is directly proportional to the fragment's speed (scalar quantity). As we will see in the following sections, the imaging techniques we use image a central “slice” of the Newton sphere containing its center, therefore the above discussion in the center of mass frame is also valid for the lab frame images: the center of the image is the center of mass position in the lab frame.

The surface distribution pattern of the fragments on the Newton sphere, usually referred to as “angular distribution” shows –under certain conditions- the relationship between the transition dipole moment, μ and the breaking bond, thus it is indicative of the (“directionality“ of the dissociation. How that works is discussed in the next section.

1.4.3 Photofragment Angular Distributions

The distribution of photofragments on the Newton sphere will be isotropic if molecules are randomly oriented in space (i.e. not preferentially aligned in one or another direction) and they are photolyzed with equal probability. The latter is determined by the absorption probability of a laser photon by a randomly oriented molecule.

The probability of absorption for an electric dipole transition is given by

$$P_{abs} \propto cos^2\theta \quad (9)$$

where θ is the angle between the transition dipole moment μ and the electric vector e of the photolysis laser.

As the transition dipole moment μ is always parallel to the electric field, if a linearly polarized laser is used, parent molecules whose internuclear axis is parallel to the electric vector will be preferentially excited creating a preferential orientation in space of the resulting photoproducts in a $\cos^2\theta$ distribution. This is the case only when the recoil time of the fragments is short compared to the parent molecule's rotational period and there is no substantial delay between the moment of the optical excitation and the bond rupture. This type of transition is described as parallel. Likewise, a perpendicular transition would yield a $\sin^2\theta$ distribution.

If the transition moment is not oriented in a parallel or perpendicular manner to the molecular axis, the transition displays a mixture of parallel and perpendicular character. Same result can be obtained in the cases where the dissociation is slow compared to the parent's rotational period (predissociation): then the resulting angular distribution will deviate from the parallel/perpendicular limits.

The general form of the photofragment angular distribution in a one-photon dissociation process may be expressed as a differential cross section [12,13]

$$\frac{d\sigma}{d\Omega} = \frac{\sigma}{4\pi}\left[\sum_{1}^{n} \beta_n P_n \cos\theta\right] \quad (10)$$

where σ is the absorption cross sections, β_n the anisotropy parameter, $P_n(x)$ the n-th order Legendre polynomial (where n must be an even integer for the linear polarized lasers used here) and θ the angle between the electric vector e and the recoil velocity vector v.

Usually the expansion is truncated at n=2:

$$I(\theta) = \frac{1}{4\pi}[1 + \beta_2 P_n \cos\theta] \quad (11)$$

The angular distribution can be characterized by the β_2 parameter, which ranges between -1 (for a perpendicular transition) and +2 (for a parallel transition). If β=0, the distribution is isotropic.

1.4.4 Ion imaging

In 1987, the Chandler and Houston groups revolutionized the field of Chemical Physics by introducing the ion imaging technique.[14] Using a uniform electric field they projected on a polaroid film the Newton sphere of the CH_3 photoproducts of the unimolecular reaction

$$CH_3I + 266\,nm \rightarrow CH_3(X, v = 0) + I/I^*$$

and showed that simultaneous information about the kinetic and angular distribution of the fragments can be obtained by analyzing the raw image using mathematics (inverse Abel transform) to go from the 2D projection to the 2D central slice of the 3D Newton sphere. The nascent fragments were created between the repeller plate and two grounded grids and extracted by a homogeneous field. In this original work, the resolution in velocity was 10% mainly because it was limited by the physical dimensions of the interaction region (molecular beam width and laser beam size at its focus on the molecular beam).

Ten years later, Eppink and Parker made an ingenuous improvement to the original set by achieving velocity focusing in a way that was independent of where the product ions where formed in the plane perpendicular to the TOF axis, succeeding in raising the velocity resolution an order of magnitude (~ 1%). They used three electrodes: a repeller, an extractor and a ground electrode without any fine mesh grids. Due to the inhomogeneity of the field between the three electrodes, the last two functioned as an electrostatic lens. As a result, all the ions formed with the same velocity were focused in the same spot of the detector irrespective of their place of formation. Although velocity mapping brought down the energy resolution, it still required mathematics (such as inv. Abel transform) in obtaining the slice of the 3D Newton sphere from its 2D projection. As these mathematics required the projected image to be parallel to the laser polarization vector, experiments with different polarizations (useful to study vector correlation phenomena like alignment and orientation) were not easily feasible. Moreover, inverse Abel transform introduced noise in the image, lowering the energy and angular resolutions.

In 2001, Gebhardt *et al.* demonstrated Slice Imaging using a pulsed repeller electric field to allow the Newton sphere to get large enough in order to be sliced using electronics instead of math. This allowed the use of different laser polarization orienta-

tions and enabled studies of alignment and orientation as well as bimolecular reaction dynamics. Shortly after Liu *et al.* [15] and Suits *et al.*[16] came up with an equivalent variation using multiple extractor electrodes instead of a pulsed repeller in order to enlarge the Newton sphere.

Since then, ion imaging and related techniques facilitated access to a wealth of dynamical information on gas phase reactions. It enabled the state-selective measurements of energy and angular/spatial distributions of reaction products from a single image. Combined with time-resolved techniques it also allowed the probing of unstable intermediates with ultrashort lifetimes (> 20 fs).[17]

As a result, unprecedented access into information about the dynamics and the nature of the electronic states controlling the photodissociation mechanisms was made possible, since each product could be probed and imaged quantum-state-selectively with great energy and spatial resolution. Determination of the quantum states of the products, thus information on how energy is partitioned towards the electronic (and vibrational or rotational) degrees of freedom in resulting atomic (or molecular) photofragments provided insight into the processes governing the bond rupture and the subsequent events promptly after the fragmentation, delving into the heart of Chemistry.

Consequently, imaging became the technique of choice for investigating photodissociation dynamics in different energy regimes. The photoproducts created via initial excitation to a lowlying excited state or a Rydberg state can be monitored and identified quantum-selectivity with high resolution in velocity, thus direct information on the dynamical picture of the molecule under study can be obtained in each case.

In the current thesis, experiments were performed using the Single Field Slice Imaging and Velocity Mapping, demonstrated by Kitsopoulos and Papadakis.[18]The single field component is an improvement of the initial Velocity Map Imaging technique[19] and the Slice Imaging of Gebhard *et al.*[20] The main alteration was that the extractor was removed and step-edged repeller and ground electrodes were utilized, providing focusing and slicing capability without sacrificing the resolution in velocity. In the single field approach, focusing condition of the ions is executed by translating the laser position along the TOF axis independently from the repeller voltage. This is achieved by introducing a small step on both the electrode and extractor voltages. Unlike using an ion lens, the velocity spread plays minimal role on the focusing. Photoe-

lectron and photofragment imaging is achieved with resolution of 1% in velocity.[18] The resolution limiting factor is the detector 'spot' resolution.

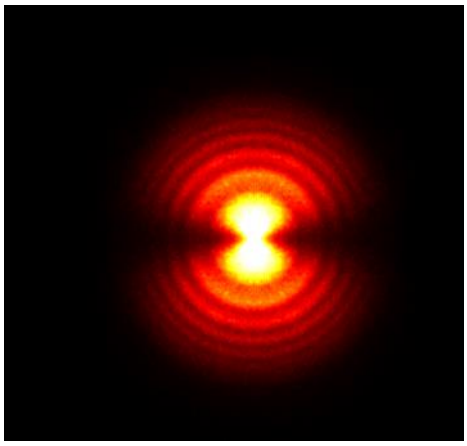

Figure 1.2: Image of CH_3^+photofragments after the photodissociation of CH_3Br at 66503 cm-1 recorded with the Slice Imaging setup.

Slice Imaging provides an additional advantage, except for the resolution and the simplification of the experimental setup on the analysis of the final image. The analysis of a recorded VMI image requires complicated mathematical transformations like Abel transform in order for the real 3D ion sphere to be reconstructed from the 2D projection. As mentioned above, mathematical transformations can introduce unwanted noise and are valid only for specific symmetry requirements (cylindrical symmetry). In Slicing mode, the Newton sphere is let to expand while travelling towards the detector which is gated in the appropriate time delay for only a slice to be selected and imaged. In this way, a 2D center 'slice' of the ion sphere is the only one recorded instead of the whole Newton sphere crushing onto the 2D screen. It should be noted that while Slice Imaging works very well for ions (even for ions as small as H^+), it does not work for electrons. The main reason is that, for ns laser ionization, the electron Newton sphere becomes too large (touching the extraction electrodes) too quickly (within the duration of the laser pulse) to be sliced effectively.

1.5 Slice Imaging Apparatus

A schematic of the photofragment imaging setup, where the experiments presented here were conducted, is presented in Figure 1.3.The apparatus consists of two differentially pumped regions, the source chamber (Region A) and the detector chamber

(Region B). A gate valve separates the two regions which are maintained in high vacuum UHV (10^{-6} -10^{-7} Torr) by different pumping configurations.

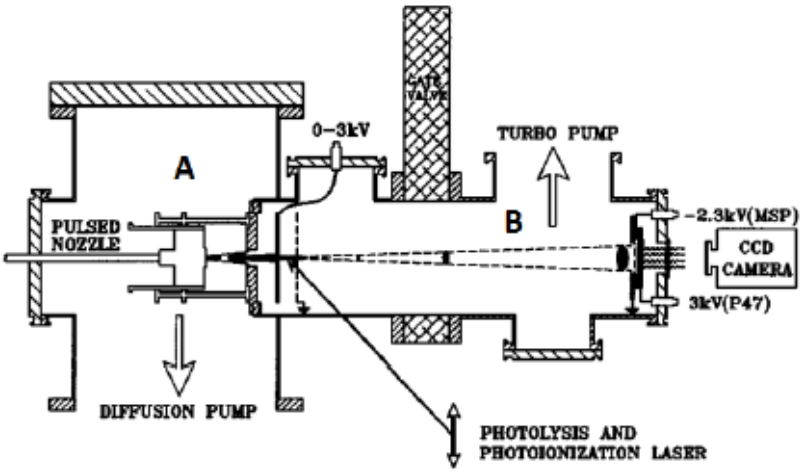

Figure 1.3 : Schematic representation of the experimental apparatus.

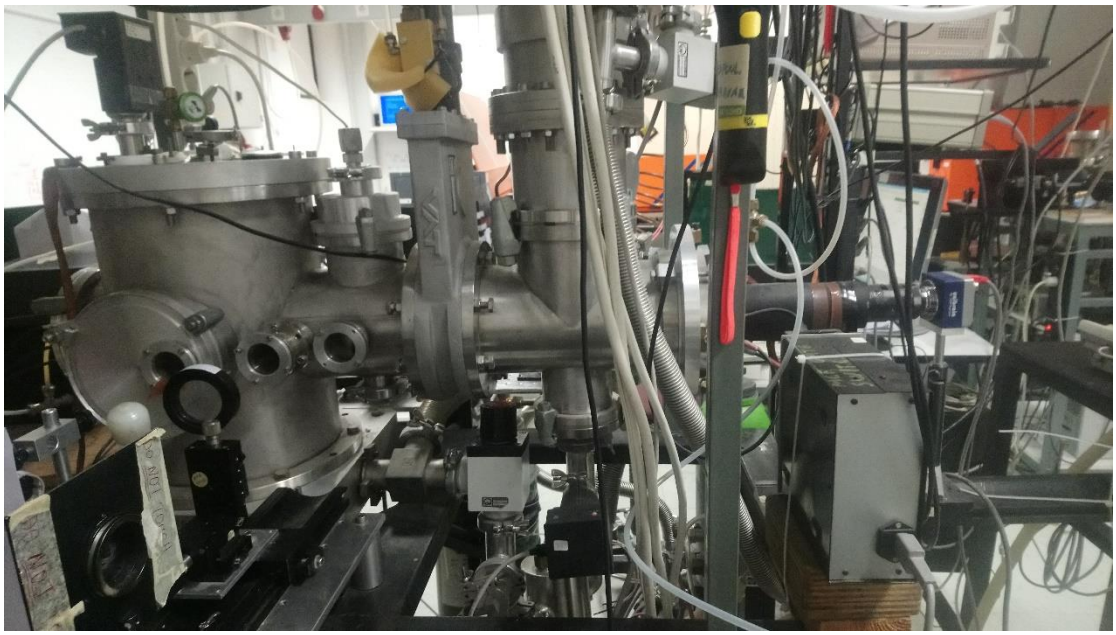

Figure 1.4 Photograph of the actual experimental apparatus used in the experiments presented here.

The source chamber is pumped by a baffled 3000 L/s oil diffusion pump (Leybold, DI 3000) that is backed by a Leybold Trivac D65B rotary mechanical pump at a speed of 65 m^3/h. In the source chamber, a home-built piezoelectrically actuated nozzle valve (0.8 mm diameter) operating at 10 Hz, is placed for the molecular beam generation. The basic valve design is based on original work of Proch and Trickl[21] with a modifi-

cation similar to work of Liu and co-workers[22] and similarly Wodtke and co-workers[23]. A supersonic molecular beam is formed by supersonic expansion into the source vacuum chamber via the nozzle valve where gas molecules of a stagnation pressure of P_o=1 bar enter the chamber. At a distance of 1-2 cm from the nozzle orifice, a Ø1.5 mm diameter skimmer (-Beam Dynamics) is placed to select the colder part of the molecular beam. The skimmer orifice is the differential pumping point between the source and detector chambers.

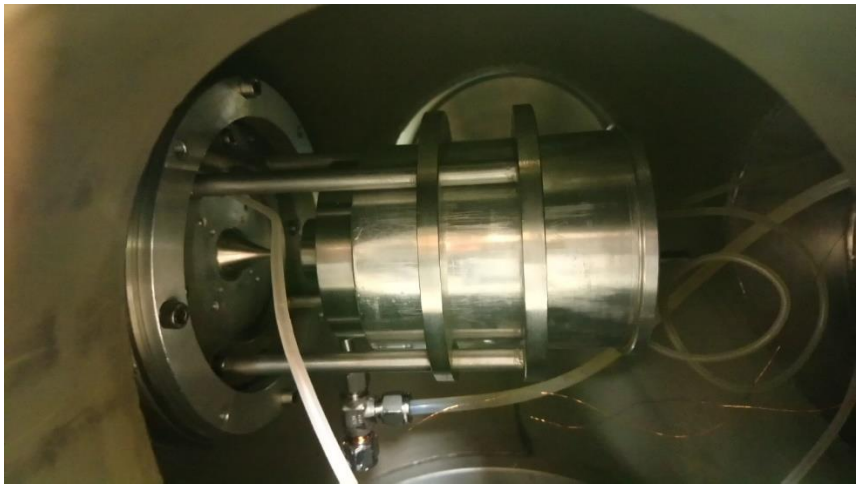

Figure 1.5 : Photograph of the nozzle and the skimmer configuration in the setup used here.

The detector chamber is pumped by a 600 *l*/s turbo-molecular pump (Leybold, Turbovac 600) that is backed by a Leybold Trivac D25B rotary pump with pumping speed of 25 m^3/h. The chamber is equipped with an ion optics setup (repeller and extractor electrodes with ~2 mm diameter holes in a 35 mm distance).

After passing through the repeller electrode, the molecular beam is intersected at right angles by the photolysis/ionization lasers focused with a 30 cm lens. The interaction region is located halfway between the repeller and extractor electrodes. By reversing the extraction voltage polarity, photoelectrons or negative ions can be detected as well.

The particle focusing is achieved at the geometric focus obtained by translating the laser beam along the TOF axis with a standard translation stage (1 full turn = 500 μm). After the ion formation, photofragments are accelerated due to the potential V of

the repeller electrode (usually 3kV) and traverse a 45cm field free TOF region before they reach a 2D position sensitive detector. Ions with different m/z ratios hit the detector in different times.

The homebuilt imaging detector is comprised of two MCPs (BASPIK) coupled to an phosphor anode (P47, Proxitronix) of an effective 50 mm diameter. The detector is gated, while on Slicing Mode, in 10-20 ns pulses so as only the center 'slice' of the ion sphere to be collected. For photoelectrons, the repeller is negatively charged and both the repeller electrode and the detector are not gated and are always ON.

The relative time delays for the experiments are controlled by a pulse generator (Berkeley Nucleonics, model BCN 565) and the experimental parameters are further improved by monitoring the ion signals in a 100 MHz oscilloscope (Hameg HM1007).

The raw images (intensity and surface pattern of electrons hitting onto the phosphor anode) are recorded asynchronously every second (approximately 10 laser shots) by a CCD camera (Unibrain i702b) equipped with a lens with zoom 50 mm fl.4 and are saved in a computer. Several thousands of frames are averaged to form images. Each image is further analyzed to extract the speed and angular distribution of the photofragments. Background images are obtained by turning the molecular beam off while keeping all the other conditions unchanged. These images are subtracted from the signal images to get the final raw image.

Laser radiation is generated by two pulsed laser systems operating at a repetition rate of 10 Hz.

(1) a Nd^{3+}:YAG (Spectra Physics, model Quanta Ray Pro 250) pumping a master oscillator-power oscillator system (Spectra Physics MOPO, 730D10),

and (2) an excimer-pumped (Lambda Physik LPX300, operating with XeCl) pulsed-dye laser (Lamda Physik LPD3000) .

1.5.1 Mass separation: Time-of-Flight Mass Spectrometry

Mass spectrometry (MS) is a method of quantitative, qualitative, isotopic and structural chemical analysis, based on the difference in arrival time introduced when charged species of different m/z ratio with the same initial velocity are left to travel in a field-free region.

Time-of-flight (TOF) mass spectrometers are the most common tools for distinguishing fragments with different mass-to-charge (m/z) ratios, therefore it is of no surprise that they are a valuable part of a chemical reaction dynamics setup.

The most well-known spectrometer of this kind is the Wiley McLaren spectrometer.[24] In the ion imaging apparatus used in this thesis, the original design with a few modifications is used.

The analyzer consists of two accelerating regions (*s* and *d*) and a field-free region D, as shown in *Figure 1.6*: Schematic representation of a Wiley-McLaren TOF mass spectrometer . The Wiley-McLaren spectrometer originally uses two flat ring electrodes covered with a very fine mesh grid to form a homogeneous electric field along the TOF axis. In our setup, the grids are removed.

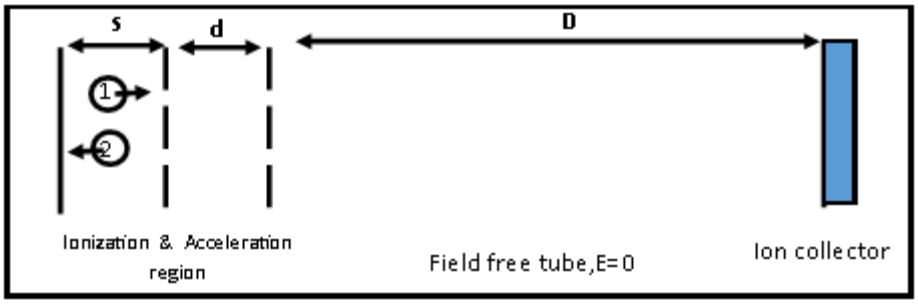

Figure 1.6: Schematic representation of a Wiley-McLaren TOF mass spectrometer

Ion formation takes place between the repeller (first electrode) and the extractor (second electrode). Afterwards, each ion, with mass m and total charge $q = ez$, is accelerated out of the source region towards the detector due to a potential difference V, the distance between the two plates is denoted as d.

The electric potential energy is converted to kinetic energy and the following equation stands.

$$E_{el} = E_K \ ,$$
$$\frac{zeV}{d} = \frac{qV}{d} = \frac{1}{2}mu^2 \ (12)$$

In our case, the masses start halfway into the field, therefore d≡d/2.

Thus, all the ions with the same charge acquire the same kinetic energy. Following their acceleration, the ions move in a field-free region towards the detector. They will reach the detector in time t that can be calculated from the following equation:

$$t_{TOF} = \frac{D}{v} \quad (13)$$

where D is the field-free region mentioned above and v is their lab velocity along the TOF axis. From the above relations, one can express the TOF time as a function of the m/z ratio:

$$\sqrt{\frac{m}{z}} = \frac{\sqrt{2eV}}{L} t_{TOF} \ (14)$$

1.5.2 Formation of fragment ions-Detection schemes

The most widely used technique for photoproduct ionization in imaging studies is the Resonance Enhanced Multiphoton Ionization (REMPI) scheme.[25] ((and references therein.).

REMPI has two very important advantages over other methods for chemical reaction product analysis applications. First, multiphoton transitions with photons in the visible and ultraviolet regime are used for ionization, instead of one high energy VUV photon. Secondly, the first step involves a resonant process. The fragments absorb one to three photons and the system is resonantly transferred to an excited state. Then, further absorption of one or two photons results to excitation above the ionization limit. This means that product analysis can occur in a state-selective manner, a crucial capability for reaction mechanism investigation.

The notation used for a REMPI process appears in the form (m + n), where m is the number of photons used for the excitation step and n the number of photons used for the ionization step. Photons of the same or different energy hv can be used for each step. In the latter case, the notation changes to (m + n').

As mentioned before, single high energy vacuum ultraviolet (VUV) photons are also used for ionization of the resultant neutral species. This scheme is widely known as

‘universal detection’ and allows simultaneous ionization of all the photoproducts. This method can be of great use for product characterization but state-selectivity is sacrificed.

Alternative routes to ion formation may occur. Non resonant multiphoton ionization (MPI), is possible if the intensity of the laser field is high enough. Also, ion pair formation (15), where neutral species absorb n photons, forming the equivalent ion pair without any intermediate steps can also lead to product ions:

$$AB + nhv \rightarrow A^{+} + B^{-}\ ion\ pair\ formation \quad (15)$$

Similarly, dissociative ionization or photolysis of the parent ion, where the ion formation precedes the photodissociation step, might also occur in some systems.[26,27]

1.5.3 Image processing and Analysis

In this subsection, the methods for obtaining the speed distributions (KERs) and the angular distributions from the raw image will be discussed. On slicing mode, there is no need for image reconstruction, therefore information is obtained directly from the image without any mathematical transformation.

The speed distribution P(u) of the photofragments is defined as the total amount of photofragments in arbitrary units with speed u and is calculated by integrating the symmetrized raw image from the image center ((center of mass of the reaction) over radius.

The radial position ρ of the photofragments is related to its speed u via the relationship

$$\rho = \mathrm{ut}\ (16)$$

where t is the TOF time. Time t is essentially constant for all ions of the same Newton sphere, as the laboratory velocity (extraction energy ~ 1.5 keV) is much greater than the center-of-mass velocity of the photofragments (typically 0.5 – 3 eV).

As for obtaining KER, we know that the pixel position is proportional to $\sqrt{E_{kin}}$ thus we can relate the kinetic energy with pixels as follows:

$$E = \mathrm{K_{cal}}(\mathrm{pix})^2\ (17)$$

In this equation K_{cal} is a calibration factor weighting for experimental parameters like repeller voltage and spatial position of the photolysis laser. Energy units are arbitrary.

The calibration factor K_{cal} can be determined experimentally using a well-known photodissociation process displaying optimally more than 3 sharp rings that belong to known photodissociation channels.

The surface pattern (angular distribution) of the ions is obtained similarly by integrating the symmetrized raw image from the center over a defined maximum radius from 0° to 90° or from 0° to 180°.

1.6 Scope of the thesis

The work presented in this thesis includes two topics on photodissociation dynamics. First, the photodissociation dynamics study of two benchmark systems for photolysis studies: CH_3I and CH_3Br, after excitation to the high energy Rydberg series region. Properties studied were the kinetic and angular distributions of the photofragments and photoelectrons upon the dissociation event using velocity map and slice imaging techniques. The key point of the analysis was the study of how the excess energy given to the system is partitioned to the photofragments (CH_3 and I or Br). Possible photodissociation mechanisms were proposed based on the accessible photodissociation channels identified. Secondly, the photodissociation of DI (deuterium iodide) at 270 nm was examined as a potential source of highly nuclear-spin-polarized deuterium source for nuclear fusion applications.

1.7 Chapter 1 References

1 Levine, R. Molecular Reaction Dynamics; Cambridge University Press: Cambridge, U.K., 2009.

2 G. Herzberg. Molecular Spectra and Molecular Structure III. Spectra of Polyatomic Molecules. Van Nostrand, New York, 1967.

3 Harris, D., & Bertolucci, M. (1978). *Symmetry and Spectroscopy: An introduction to vibrational and electronic spectroscopy*. New York: Oxford University Press.

4 Barrow, G. *Introduction To Molecular Spectroscopy*; McGraw-Hill: Auckland, 1962.

5 T. F. Gallagher, Rydberg Atoms (Cambridge Monographs on Atomic, Molecular and Chemical Physics, Cambridge, 1994.

6 Reisler, H.; Krylov, A. Interacting Rydberg and Valence States In Radicals and Molecules: Experimental And Theoretical Studies. *International Reviews in Physical Chemistry* 2009, 28, 267-308.

7 H. Hróðmarsson, A. Kartakoullis, D. Zaouris, P. Glodic, H. Wang, P. Samartzis and Á. Kvaran, *Physical Chemistry Chemical Physics*, 2017, 19, 11354-11365.

8 Stolow, A.; Bragg, A.; Neumark, D. Femtosecond Time-Resolved Photoelectron Spectroscopy. *Chemical Reviews* 2004, 104, 1719-1758.

9 Pratt, S. Vibrational Autoionization in Polyatomic Molecules. *Annual Review of Physical Chemistry* 2005, 56, 281-308.

10 J. J. H. van den Biesen, "Elastic Scattering I: Integral Cross Sections", *In Atomic and Molecular Beam Methods*, Vol. I, ed. G. Scoles, (Oxford University Press, New York, 1988) p472.

11 Scoles, G. (1988). *Atomic and molecular beam methods*. New York: Oxford University Press.

12 Rakitzis, T.; Zare, R. Photofragment Angular Momentum Distributions In The Molecular Frame: Determination And Interpretation. *The Journal of Chemical Physics* 1999, 110, 3341-3350.

13 Zare, R.; Herschbach, D. Doppler Line Shape of Atomic Fluorescence Excited By Molecular Photodissociation. *Proceedings of the IEEE* 1963, 51, 173-182.

14 Chandler, D.; Houston, P. Two-Dimensional Imaging of State-Selected Photodissociation Products Detected by Multiphoton Ionization. *The Journal of Chemical Physics* 1987, 87, 1445-1447.
15 Lin, J.; Zhou, J.; Shiu, W.; Liu, K. Application Of Time-Sliced Ion Velocity Imaging To Crossed Molecular Beam Experiments. *Review of Scientific Instruents* 2003, 74, 2495-2500.
16 Townsend, D.; Minitti, M.; Suits, A. Direct Current Slice Imaging. *Review of Scientific Instruments* 2003, 74, 2530-2539.
17 de Nalda, R.; Durá, J.; García-Vela, A.; Izquierdo, J.; González-Vázquez, J.; Bañares, L. A Detailed Experimental and Theoretical Study of The Femtosecond A-Band Photodissociation Of CH3I. *The Journal of Chemical Physics* 2008, 128, 244309.
18 Papadakis, V.; Kitsopoulos, T. Slice Imaging and Velocity Mapping Using A Single Field. *Review of Scientific Instruments* 2006, 77, 083101.
19 Eppink, A.; Parker, D. Velocity Map Imaging of Ions and Electrons Using Electrostatic Lenses: Application in Photoelectron And Photofragment Ion Imaging Of Molecular Oxygen. *Review of Scientific Instruments* 1997, 68, 3477-3484.
20 Gebhardt, C.; Rakitzis, T.; Samartzis, P.; Ladopoulos, V.; Kitsopoulos, T. Slice Imaging: A New Approach To Ion Imaging And Velocity Mapping. *Review of Scientific Instruments*2001, 72, 3848-3853.
21 D. Proch and T. Trickl. A high-intensity multi-purpose piezoelectric pulsed molecular beam source. *Review of Scientific Instruments* 1989, 60(4), 713-716.
22 F. Dong, S.-H. Lee, and K. Liu, “F. Dong, S.-H. Lee, and K. Liu. Reactive excitation functions for and the vibrational branching for F + HD”, *J. Chem. Phys*. 2000, 113, 3633.
23 Q. Ran, D. Matsiev, D. J. Auerbach, and A. M. Wodtke, “An advanced molecule-surface scattering instrument for study of vibrational energy transfer in gas-solid collisions”, *Rev. Sci. Instrum.*2007, 78, 104.
24 W. C. Wiley and I. H. McLaren, “Time-of-flight mass spectrometer with improved resolution”, *Rev. Sci. Instrum.*1955, 26, 12, 1150.
25 Ashfold, M.; Howe, J. Multiphoton Spectroscopy of Molecular Species. *Annual Review of Physical Chemistry* 1994, 45, 57-82.

26 Peterka, D.; Ahmed, M.; Ng, C.; Suits, A. Dissociative Photoionization Dynamics of SF_6 By Ion Imaging with Synchrotron Undulator Radiation. *Chemical Physics Letters* 1999, 312, 108-114.
27 Greene JR, Francisco JS, Huang J, Xu D, Jackson WM. Photodissociation studies of $CBr_4^+$and CBr_3^+ at 267 nm using ion velocity imaging. *The Journal of Chemical Physics*. 121: 5868-73.

2 Multiphoton Rydberg and valence dynamics of CH_3Br probed by slice imaging

2.1 Introduction

The methyl halides play an important role in the chemistry of the atmosphere.[1,2,3,4]Although far less abundant than methyl chloride in the stratosphere, methyl bromide is found to be much more efficient in ozone depletion.4 Furthermore, bromocarbons are known to have a high global warming potential.[5] This has triggered a considerable interest in the spectroscopy[3,6,7,8,9,10,11] and photofragmentation dynamics[11,12,13,14,15,16,17,18,19,20]of methyl bromide over the last few decades. Additionally, the molecule is a simple prototype of a halogen-containing organic molecule for fundamental studies of photodissociation and photoionization involving formation of the cornerstone fragment CH_3.[15,18,20]

The basic picture for the electronic configuration of hydrogen and alkyl halides was given by Mulliken.[21]The ground state molecular orbital configuration of CH_3Br for the outer valence is $a_1^2e^4$ (C_{3v}) or $\sigma^2\pi^4$ ($C_{\infty v}$). The overall symmetry is $^1A_1$. Excitation of one of the electrons of the lone pair orbitals e to the anti-bonding orbital a_1* gives rise to the ^3E and ^1E molecular states. Excitation of one of the electrons of the bonding pair orbitals a_1 to the anti-bonding orbital a_1* gives rise to the repulsive states $^3A_1$ and $^1A_1$ molecular states. Higher energy excitations of the lone pair electrons or a_1 valence electrons to 5s or 5p Rydberg orbitals create the molecular Rydberg states. In the first case, the potential energy surfaces of the Rydberg states and the ones from the molecular ion CH_3Br^+ are expected to be similar since the bonding a_1 valence electrons remain unchanged. The Rydberg potentials minima have been calculated to be 3.7 a.u. close to the one of the CH_3Br^+ molecular ion.[28]

Lepetit *et al.*[28], conducted detailed configuration interaction ab initio calculations on the valence and 5*s* and 5*p* Rydberg bands of the CH_3Br molecule as a function of the methyl-bromide distance. Inclusion of spin-orbit interaction increases the complexity of the curves due to a decrease in the degree of degeneracy of each band.

The $^{1,3}Q_{a,b}$ notation for CH_3X states, was introduced by Mulliken[21] as an analogy to the states of hydrogen halides . The numbers 1, 3 describe the spin multiplicity and the a, b the projection of the total angular momentum on the C-X bond in C_{3v} geometry. States $^3Q_1$ (E),$^3Q_{0+}$ (A) and ^1Q(E) are analogous to $^3\Pi_1$,$^3\Pi_{0+}$ and $^1\Pi$ for HX molecules.

Potential Energy Surface for the ground state and low-lying excited states of CH_3Br has been calculated recently via ab initio methods by Fujihara *et al.*[40] In low energies, the photodissociation process is well understood. A nonbonding lone-pair electron from the Br atom is promoted to a σ* orbital of the C-Br bond. Due to spin-orbit coupling, degeneracy is broken and the states $^1Q_1$, $^3Q_0$ and $^3Q_1$ arise. All these excited states are repulsive and lead to rapid dissociation (compared to molecular rotation time scales) to CH_3 and Br. Exclusive production of ground state Br atoms ($^3P_{3/2}$) is linked to perpendicular transitions via the $^1Q_1$ and $^3Q_1$ states. Production of spin-orbit excited Br* atoms ($^3P_{1/2}$) is linked to the excitation to the $^3Q_0$ state via a parallel transition. Distortion of the molecular geometry can result to lower symmetry (C_s group) and lead to strong coupling between the $^1Q_1$ and $^3Q_0$.

Photofragmentation studies of methyl bromide can be classified into two groups. One group focuses on the characterization of photofragments CH_3 + Br($^2P_{3/2}$)/Br*($^2P_{1/2}$) resulting from photodissociation in the A band[13-15,18,22,23,24]whereas the other group concerns the involvement of higher energy Rydberg and ion-pair states (‘‘the Rydberg state region’’).[11,16,17,19,20] In the first group, single-wavelength excitation studies (193 and 222 nm,[12,24] 205 nm,[13] 213 and 230 nm,[15,25] and 216 nm[15]) as well as wavelength range excitations (215–251 nm[14] and 240–280 nm[23]) have been performed by the use of time-of-flight[12,23] and imaging[13-15,24,25] techniques. In the second group the emphasis has been on the involvement of Rydberg and ion-pair states in photodissociation processes to form ion pairs.[11,16,17,20]Photoionization studies are focused on the lowest energies of the ion and its breakdown.[11,26,27] Multiphoton dissociation studies focus on excitations to the lowest Rydberg states (5s) of the molecule.[19] The energetics of methyl bromide (CH_3Br) in the Rydberg state region have been studied quite thoroughly to map the Rydberg state structure of the molecule both by absorption spectroscopy7 and by Resonance Enhanced MultiPhoton Ionization (REMPI),[11,20] as well as theoretically.[28]

Recently, the effect of state interactions within the Rydberg state region on photofragmentation processes for the hydrogen halides has been explored.[29,30,31,32,33,34] These studies have revealed effect of Rydberg to valence as well as Rydberg to Rydberg state interactions on both the photodissociation and photoionization mechanisms within the molecules on a rotational and vibrational energy level basis. We now expand this approach to polyatomic molecules, starting with methyl bromide (CH_3Br).

Here we present Slice imaging and Velocity map imaging data for product ions and photoelectrons upon two-photon resonant excitation of CH_3Br to selected np and nd Rydberg states in the 66 000–80 000 cm^{-1} by a one-color excitation scheme (see Table 2.1). Despite the initial step being two-photon resonant excitation, three-photon excitations followed by dissociations to form Rydberg states of CH_3 are found to dominate the dynamics. For the three highest energy excitations an additional three-photon channel opens, generating translationally hot $CH_3(X)$ and Br/Br* and for two of these three excitations one-photon processes are also observed. These results are discussed in view of previous work on the low and high energy excited state dynamics of CH_3Br.

2.2 Experimental

The Velocity Map Imaging (VMI)/Slicing setup used in this work has been described in detail in Chapter 1 and elsewhere.[35,36] Hence, only a brief description will be given here. A supersonic molecular beam, typically a mixture of 20% CH_3Br in He, is expanded through a home-made piezoelectrically-actuated nozzle valve ((1 mm orifice) and skimmed ((1.5 mm, Beam Dynamics) prior to entering the interaction region where the photodissociation occurs. A stagnation pressure of P_0 = 1 bar was used. The photolysis/ionization laser beam was focused (f = 30 cm) on the geometric focal point of a single-electrode repeller-extractor plate arrangement where it intersected the collimated molecular beam at right angles. The laser beam (typically 1.5 mJ per pulse) was generated by a pulsed Nd^{3+}: YAG laser (Spectra Physics Quanta Ray Pro 250) pumping a master oscillator–power oscillator system (Spectra Physics MOPO 730-10) set at the appropriate wavelength.

For the slicing experiments, reported here, the repeller is pulsed ON at the appropriate time delay (~300 ns) following the photolysis/ionization. The charged photofragments

traverse a field-free time-of-flight region (45 cm) before hitting a gated, position- sensitive detector (dual, imaging-quality Micro-Channel Plates (MCP) array coupled to a phosphor screen) where images of the center slice of the photofragment sphere are recorded. The image frame is recorded asynchronously every second (~10 laser shots) by a Charge- Coupled Device (CCD) camera and several thousand frames are averaged to form images. Each final image is integrated from its center over radius to extract the speed and over angle to extract the angular distributions of the corresponding fragments. For photoelectrons, the repeller has reversed polarity and both the repeller electrode and the detector are not gated (*i.e.* they are always ON).

2.3 Results

2.3.1 Mass Resolved MPI

(2 + m) as well as (3 + m) REMPI spectra and spectral assignments for CH_3Br have been reported in ref. 20 and 11. The (2 + m) REMPI spectrum for CH_3^+ ion detection from ref. 11 for the two-photon resonant excitation region of 66 000–80 000 cm^{-1} is reproduced in Fig. 2.1 along with mass spectra for selected molecular Rydberg state resonances normalized to the CH_3^+ signal intensity. All the mass spectra show the CH_3^+ ion mass signal ($I(CH_3^+)$) to be the strongest and the signal intensities to vary as, $CH_3^+ > CH_2^+ > CH^+ > (Br^+, CBr^+)$. The relative ion intensities, $I(M^+)/I(CH_3^+)$, for $M^+ = CH_2^+$, CH^+ and Br^+ are found to vary with the excitation energy and to reach maxima as the wavenumber values get closer to the ion-pair threshold ($CH_3^+ + Br^-$; Fig. 2.1b). Closer inspection of the REMPI spectra shows that there are two major contributions, an underlying continuum, gradually increasing with excitation wavenumber, superimposed with the REMPI peaks.

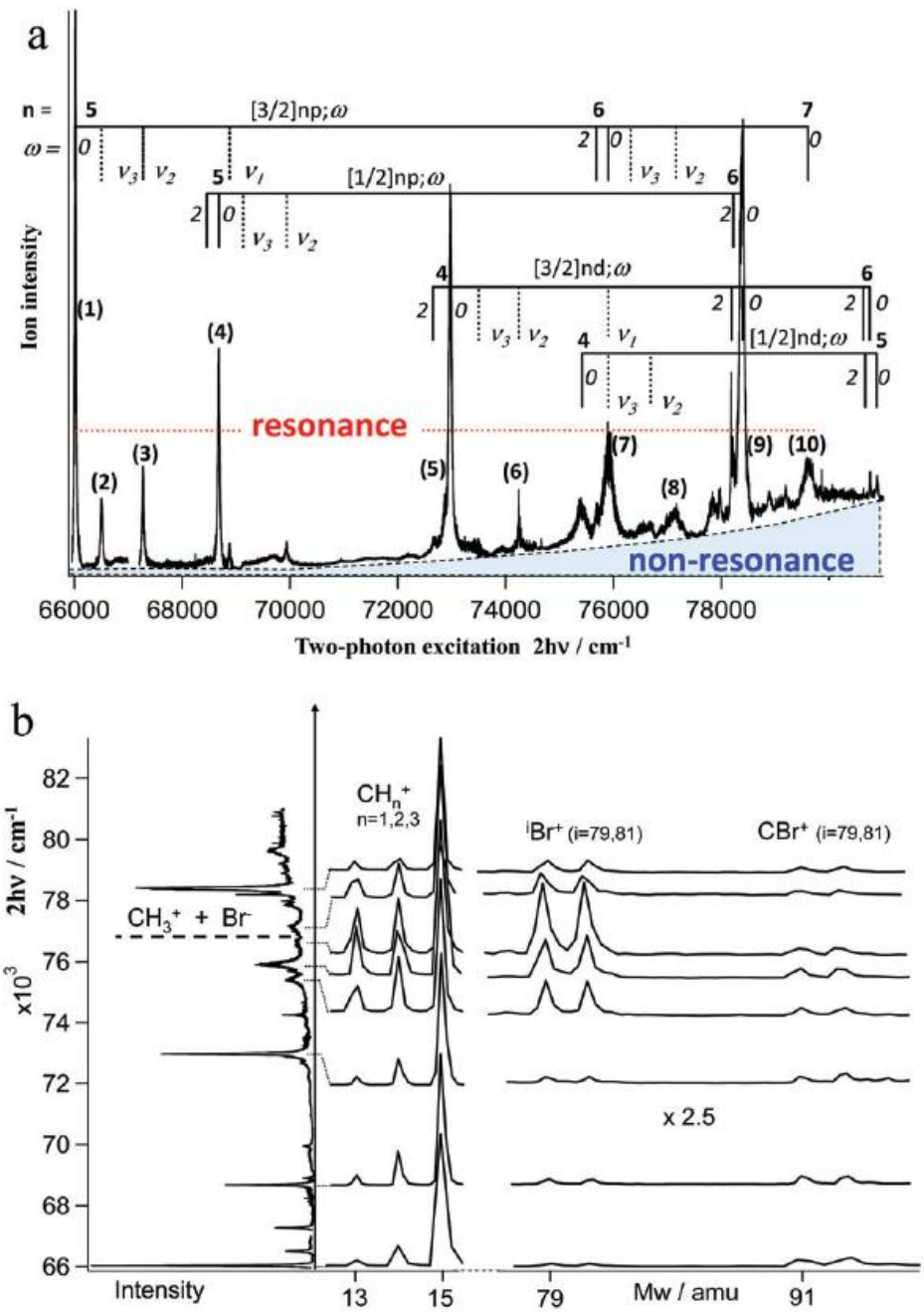

Figure 2.1 MassResolved (MR) MPI for CH_3Br: (a) CH_3^+ signal (MPI spectrum) for the two photon wavenumber range of 66000-80000 cm^{-1} and CH_3Br Rydberg state (CH3Br) assignments. Separation of the spectrum into resonant and non-resonant contributions is indicated (See Table 1). (b) Mass spectra of selected CH_3Br Rydberg state resonances. Signals for masses larger than 78 amu have been expanded by a factor of 2.5.**

The latter correspond to two-photon resonant transitions to the parent molecular Rydberg states as an initial excitation[11,20] prior to further excitation/dissociation/ionization processes (*i.e.* (2 + *m*) REMPI). The continuum, on the other hand, involves transitions to non- quantized energy levels, *i.e.* non-resonant transitions (Fig. 1a), of which initial one-photon transitions to repul-

sive molecular valence states are likely.[14,15,23] Such transitions are followed by dissociation (*i.e.* one-photon photodissociation) to form CH_3 in the ground electronic state (X) and bromine atoms in their ground (Br($^2P_{3/2}$), henceforth denoted Br) or spin–orbit excited (Br($^2P_{1/2}$), henceforth denoted Br*) states, which are subsequently ionized by (non-resonant) multiphoton ionization (MPI). From now on these two contributions will be referred to as the resonant and the non-resonant contributions to the MPI spectrum, respectively.

2.3.2 Slice images and Kinetic Energy Release spectra (KERs)

CH_3^+ ion slice images (Figure 2.2) were recorded for MPI of CH_3Br corresponding to (2 + m) REMPI for resonant excitation to a total of ten molecular Rydberg states (with np and nd Rydberg electron configurations and different vibrational states), converging to both spin–orbit components of the ground ionic states X($^2P_{3/2}$) and X*($^2P_{1/2}$) in the two-photon excitation region of 66000–80000 cm^{-1} (see Table 2-1 Number labeling for the ten CH_3Br Molecular Rydberg states with the corresponding one-photon excitations (nm) and two photon excitations (cm^{-1}) along with the state of Rydberg state CH3 detected upon each excitation.Table 2-1). Kinetic energy release spectra (KERs) were derived from the images (See Figure 2.3).

Table 2-1 Number labeling for the ten CH_3Br Molecular Rydberg states with the corresponding one-photon excitations (nm) and two photon excitations (cm^{-1}) along with the state of Rydberg state CH3 detected upon each excitation.

Image no.	CH_3Br Rydberg states; $[\Omega_c]nl$; ω,$(\nu_1\nu_2\nu_3)$[a]	One-photon excitation/nm	Two-photon excitation/cm^{-1}	CH_3 Rydberg states detected
1	[3/2]5p; 0, (000)	302.943	66 019[c]	3p; $^2A_2$
2	[3/2]5p; 0, (001)	300.738	66 503[d]	3p; $^2A_2$
3	[3/2]5p; 0, (010)	297.287	67 275[d]	3p; $^2A_2$
4	[1/2]5p; 0, (000)	291.188	68 684[c]	3p; $^2A_2$
5	[3/2]4d; 0, (000)	274.059	72 977[c]	3d; $^2E/^2A_1$
6	[3/2]4d; 0, (010)	269.364	74 249[d]	3d; $^2E/^2A_1$
7	[3/2]6p; 0, (000)/[3/2]4d; 0, (100)/[1/2]4d; 0, (001)[b]	263.487	75 905[c]	4p; $^2A_2$, 3d; $^2E/^2A_1$
8	[3/2]6p; 0, (010)[b]	259.185	77 165[d]	4p; $^2A_2$, 3d; $^2E/^2A_1$
9	[1/2]6p; 0, (000)/[3/2]5d; 0, (000)	255.199, 255.099	78 370[c], 78 401[c]	4p; $^2A_2$, 3d; $^2E/^2A_1$, 4f; 2E
10	[3/2]7p; 0, (000)	251.225	79 610[c]	4p; $^2A_2$, 3d; $^2E/^2A_1$

[a] $[\Omega_c]$: total angular momentum quantum number for the core ion. n: principal quantum number for the Rydberg electron. l: Rydberg electron orbital (p,d). ω: total angular momentum quantum number for the Rydberg electron. (ν_1, ν_2, ν_3): vibrational quantum numbers referring to vibrational modes, ν_1 (symmetric stretch), ν_2 (umbrella) and ν_3 (C–Br stretch). [b] Spectral overlap. [c] Ref. 20. [d] Ref. 11.

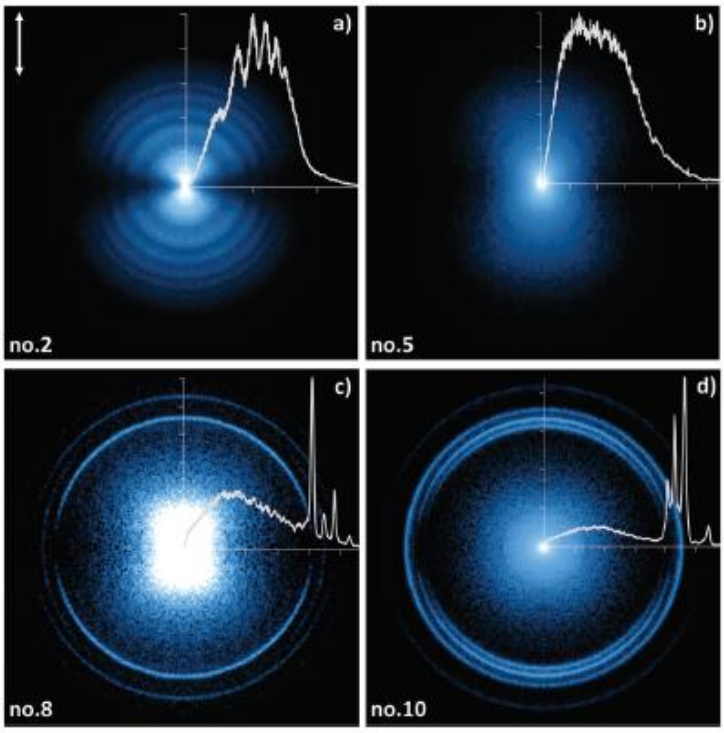

Figure 2.2 CH_3^+ slice images and the corresponding kinetic energy release spectra (KERs) for excitation numbers 2(a), 5 (b), 8(c) and 10 (d) (see Table 2-1). The image intensity scale has been adjusted to show all major features. The KERs are normalized to the strongest peak in each spectrum. The laser polarization is indicated by the double arrow in panel (a).

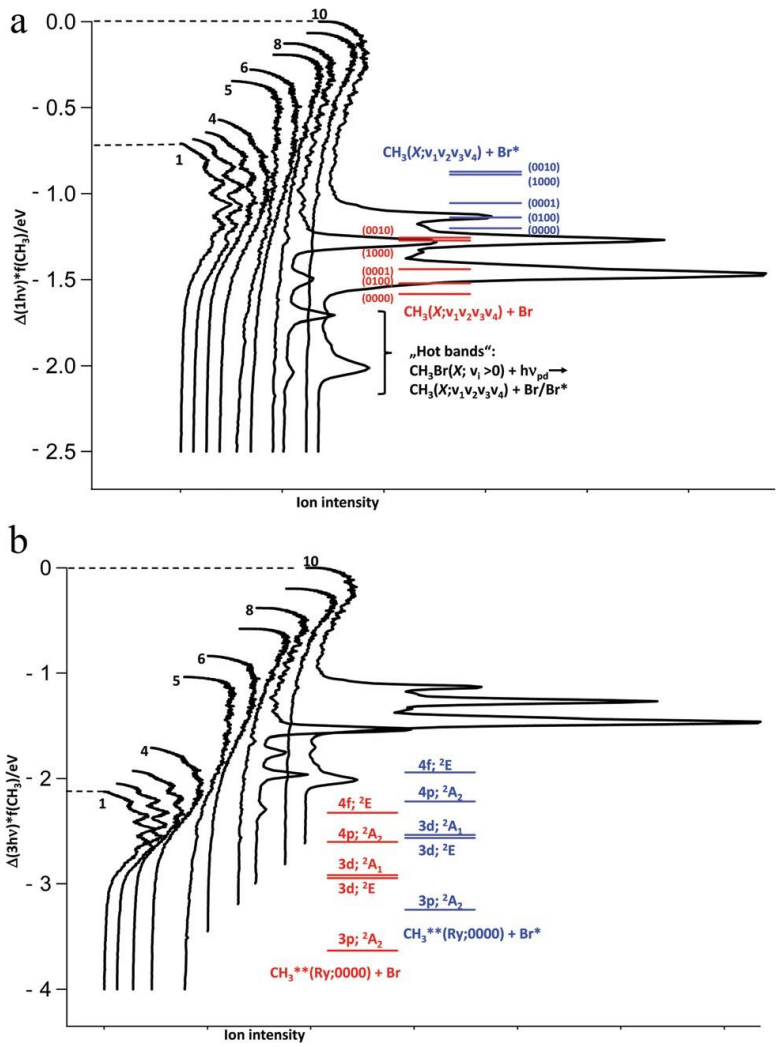

Figure 2.3 CH_3^+ Kinetic Energy Pelease spectra (KERs) derived from images no. 1–10 (see Table 2-1 and Fig. 2.1a). The spectra are normalized to the height of the lowest KER spectra contributions, corresponding to resonant contributions (see main text) in each spectrum. The spectra are plotted as a function of a relative (a) 1hν and (b) 3hν shift.

3 3

Two major spectral components could be identified from the images/KERs corresponding to the non-resonant and resonant contributions mentioned above. Large non-resonant contributions are observed at two of the highest energy two-photon resonant excitations only (77165 cm^{-1} and 79 610 cm^{-1}; transitions no.8 and 10 in Table 1). The non-resonant MPI spectral contributions (see Fig. 1a) appear as clear rings in the images/sharp peaks in the KERs (Fig. 2 and 3) as to be expected for direct nonresonant photodissociation processes (see further discussion in Section IV.B). Very small non-resonant spectral contributions were also observed for the excitations 75905 cm^{-1} (7) and 78370/78401 cm^{-1} (9).

The MPI spectral contributions (Fig. 1a) due to the resonant transitions are observed for all the data as broad ‘‘underlying’’ KER spectral structures peaking at low KER as to be expected for resonance excitations followed by delayed dissociation processes (see further discussion in Section 2.4.1)Vibrational structure is exhibited for the lowest four energy excitations (66019-68684cm^{-1}) (Fig. 3).

The non-resonant contributions observed can be assigned to the stepwise processes,

$CH_3Br + 1hv \rightarrow CH_3Br^*$; non-resonant transition (1a)

$CH_3Br^* \rightarrow CH_3\,(X; v_1v_2v_3v_4) + Br/Br^*$; dissociation (1b)

$CH_3\,(X; v_1v_2v_3v_4) + 3hv \rightarrow CH_3^+ + e^-$; photoionization (1c)

where CH_3(X; $v_1v_2v_3v_4$) refers to the ground electronic state of CH_3(X) and vibrational levels v_1, v_2,v_3,v_4 and Br/Br* refer to the ground (Br) and spin–orbit excited (Br*) states of bromine, respectively.

Since the kinetic energy release by the CH3 $^+$ ions formed is determined by the initial step (1a) it is convenient to compare the corresponding KERs contributions on a relative one-photon energy scale (Δ(1hv) = 1hv$_i$-1hv$_o$ where v$_o$ and v$_i$ are one-photon excitation frequencies of a reference spectrum (v$_o$) and a spectrum i (v$_i$) for v$_o$>v$_i$) weighted by the mass ratio factor for CH_3, f(CH_3) =m(^{j}Br)/m($CH_3{}^j$Br) ((j = 79, 81), to take account of the conservation of momentum. Thus, spectral peaks due to the formation of the same species/thresholds, CH_3(X; v$_1$v$_2$v$_3$v$_4$) + Br/Br*, will match. This has been carried out in Fig. 3a, which shows the KERs shifted by the weighted one-photon energy difference Δ(1hv)*f(CH_3) where the ‘‘zero kinetic energy released’’ for the two-photon excitation to the [3/2]7p; 0, (000) CH3Br Rydberg state (image/KER no. 10/79 610 cm $^{-1}$; see Table 1) has been set to zero (reference spectrum). Thresholds corresponding to the ‘‘maximum possible kinetic energy released’’ for formation of the various CH_3(X; v$_1$v$_2$v$_3$v$_4$) species (along with Br/Br*) are also marked in Figure 2.3.

All sharp peaks observed in spectrum no. 8/77 165 cm^{-1} are found to match peaks in no. 10/79 610 cm^{-1}. Some overlap of the peaks is observed in spectrum no. 10/79 610 cm^{-1}. The peaks observed in the region of Δ(1hv) *f (CH_3) =-1.6 to 0.0 eV are due to excitations of CH_3Br(X) in its ground vibrational state, whereas those of Δ(1hv)*f

(CH_3)<-1.6 eV are due to excitations of vibrationally excited $CH_3Br(X)$ molecules (''hot bands''). We assign the peaks at about Δ(1hν)*f (CH_3) =-1.49 eV (Figure 2.3), both in spectra no. 8 and 10 and at about Δ(1hν)*f (CH_3) = -1.13 eV in no. 10 to the formation of a vibrationally excited $CH_3(X)$ in the out-of-plane bending (umbrella) mode (v_2 = 1), i.e. CH_3(X; 0100) along with Br and Br*, respectively. The peaks at about Δ(1hν)*f (CH_3) = -1.27 eV (Fig. 3a), both in spectra no. 8 and 10 are due to the formation of a vibrationally excited $CH_3(X)$ in stretching modes (v1 = 1 and/or v3 = 1), i.e. CH_3(X; 1000) and/or CH_3(X; 0010), along with Br.

Comparison of the KERs of the resonant contributions as well as analysis of the corresponding photoelectron spectra (PES, see below) reveals that the kinetic energy released by the CH_3^+ ions is determined by dissociation after an initial three photon excitation step. Therefore, in Fig. 3b, the corresponding KER spectra are compared on a weighted relative three-photon energy scale ((3hν)*f (CH_3); (Δ(3hν) = 3hvi-3hvo. Furthermore, analysis of the photoelectron spectra (see below) suggests that electrons are released by one-photon ionization of Rydberg states of CH_3 (CH_3**). We, therefore, propose that the overall excitation process involves formation of CH_3** along with Br/Br* by three-photon photodissociation (two photons to an intermediate Rydberg state (see Table 2-1 Number labeling for the ten CH_3Br Molecular Rydberg states with the corresponding one-photon excitations (nm) and two photon excitations (cm^{-1}) along with the state of Rydberg state CH3 detected upon each excitation.Table 2-1) plus one additional photon to reach one or more ''superexcited'' repulsive state denoted here as $CH_3Br^{\#}$) followed by one-photon ionization of CH_3** to form CH_3^+ as follows,

$$CH_3Br + 2hv \rightarrow CH_3Br^{**}\,(Ry; v_1v_2v_3); \qquad \text{resonant transition (2a)}$$

$$CH_3Br^{**}\,(Ry; v_1v_2v_3) + 1hv \rightarrow CH_3Br^{\#}; \qquad \text{photoexcitation (2b)}$$

$$CH_3Br^{\#} \rightarrow CH_3^{**} + Br/Br^{*}; \qquad \text{dissociation (2c)}$$

$$CH_3^{**} + 1hv \rightarrow CH_3^{+} + e^{-}; \qquad \text{photoionization (2d)}$$

where CH_3Br**(Ry; $v_1v_2v_3$) represents vibrational levels v_1, v_2, v_3 of a parent molecular Rydberg state and $CH_3Br^{\#}$ represents one or more superexcited state(s).

The vibrational structure with a progression frequency corresponding to about 1300 cm^{-1} observed for the lowest excitation KERs (no. 1–4; Fig. 3) resembles that to be expected for transitions to vibrational levels of a CH_3** Rydberg state of an out of plane/umbrella mode.[37,38] The position of the thresholds for CH_3**($3p^2A_2$) + Br/Br* formation following the three photon excitation process (Figure 2.3; see also text above) in the tail of the KER spectra on the high energy side of the vibrational structure, as well as analysis of the corresponding photoelectron spectra (see below) suggests that the vibrational structure corresponds to the formation of CH_3**($3p^2A_2$; $v_1v_2v_3v_4$) for varying quantum levels of the out-of-plane bending mode (v_2).Structure analysis of the four lowest excitation energy KER spectra in the two-photon region of 66019–68684 cm^{-1} revealed the vibrational constants ω_e = 1311 ±5 cm^{-1} and $\omega_e x_e$ = 11±1 cm^{-1} for the out-of-plane (v_2) vibrational mode of CH_3**($3p^2A_2$). This is to be compared with the vibrational wavenumber value of 1323 cm^{-1} reported for CH_3**($3p^2A_2$) in NIST.[37,38]

Br^+ ion slice images were recorded following CH_3Br resonance excitations to Rydberg states in the two-photon excitation region of 66000 -80000 cm^{-1} listed in Table 1 (except for no. 2/66 503 and no. 6/74 249 cm^{-1}). KERs were derived from the images (see Fig. 4). All the KERs exhibit a broad spectral structure peaking at low kinetic energies in the region of about 0.2 eV KER. The peak shifts to lower KER as the excitation energy increases. An additional broad peak is present at around 1 eV KER for the excitations no. 8/77 165 cm^{-1}, no. 9/78 370 cm^{-1} and no. 10/79 610 cm^{-1} spectra (**Figure 2.4**). For the no. 10/79 610 cm-1 spectrum there is also a sharp peak at about 0.27 eV KER. We attribute the sharp peak in the no. 10/79610 cm^{-1} KER spectrum to the non-resonant contribution producing Br ground state along with CH_3(X; $v_1v_2v_3v_4$) by one-photon dissociation, i.e.

$$CH_3Br + 1hv \rightarrow CH_3Br^*; \qquad \text{non-resonant transition (3a)}$$

$$CH_3Br^* \rightarrow CH_3\,(X; v_1v_2v_3v_4) + Br\,; \quad \text{dissociation (3b)}$$

$$Br + 3hv \rightarrow Br^+ + e^-\,; \qquad \text{photoionization (3c)}$$

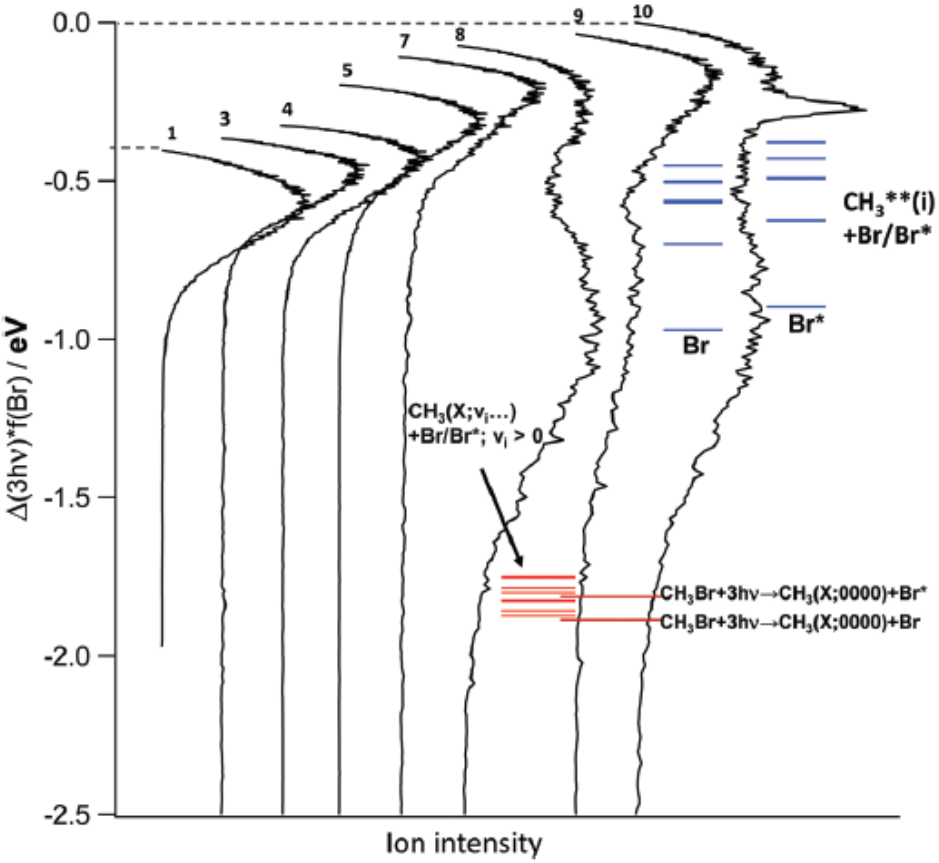

Figure 2.4 Br^+ Kinetic Energy Release spectra (KERs) derived from images no. 1, 3–5, and 7–10 (see Table 1 and Fig. 1a). The spectra are normalized to the height of the lowest KER spectra contributions, corresponding to resonant contributions (see main text) in each spectrum. The spectra are plotted as a function of a relative scale D(3hv)*f (Br) (for $CH_3{}^{79}Br$) (see explanation in main text of Section IV) and tilted to the right (i.e. plotted vertically). Common energy thresholds for the formation of CH_3(Ry, v1v2v3v4) + Br/Br* as well as CH_3(X, $v_1v_2v_3v_4$) + Br/Br* after three-photon photodissociation of CH_3Br via resonant excitation to CH_3Br Rydberg states are indicated.**

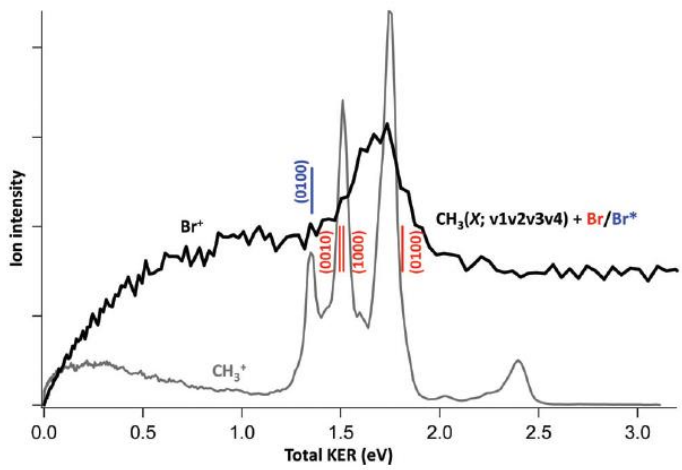

Figure 2.5 Br^+ (black,above) and CH_3+ (grey,below) kinetic energy release spectra (KERs) as a function of total kinetic energy released, Common energy thresholds for the formation of CH3 (X,$v_1v_2v_3v_4$) + Br/Br* after non-resonant one-photon photodissociation of CH_3Br are indicated.

Comparison of the total KERs (see Figure 2.5) derived from the no.10 images of Br^+ and $CH_3{}^+$ shows a sharp peak for Br to match the strongest sharp peak for CH_3, which corresponds to the formation of CH_3 with one quantum in the umbrella mode (CH_3(X; 0100)).The broad low kinetic energy peak present in all KERs (**Figure 2.4**) fits energetically the production of Br/Br* along with CH_3** Rydberg states (channels (2a)–(2c)). As discussed for CH_3 this is a three-photon process in two steps: First CH_3Br is excited resonantly with two photons (channel 2a) to a Rydberg state (Table 1), which subsequently absorbs an additional photon towards a superexcited $CH_3Br^{\#}$ state (or states; 2b) dissociating to CH_3** + Br/Br*. The broad, high kinetic energy contribution, only seen in the no. 8/77 165 cm^{-1}, no. 9/78 370 cm^{-1} and no. 10/79 610 cm^{-1} spectra (**Figure 2.4**), on the other hand, is due to Br/Br* formed along with CH_3(X, $v_1v_2v_3v_4$) after a three-photon photodissociation process via the molecular Rydberg states ((2a) and (2b)). In both cases, Br^+ is subsequently generated by three-photon-MPI of Br/Br*.Relevant energy thresholds for these two processes are shown in Fig. 4 along with the KERs plotted on a Δ(3hν)*f(Br) scale.

2.3.3 Angular Distributions

Significant variations in angular distributions are observed for the CH_3^+ ions depending on the channels involved (see Figure 2.2). Signals associated with the resonant excitations, mostly display shapes corresponding to parallel or isotropic distributions, whereas those due to the non-resonant excitations are found to display shapes corresponding to both parallel and perpendicular transitions. In an attempt to quantify the anisotropy of the rings, angular distributions, in the form of signal intensities as a function of the angle from 0 to 180°, derived from the images, were fitted by the simplified expression corresponding to a one-step photodissociation,

$$P(\theta) = A[1 + \beta_2 P_2 \cos\theta + \beta_4 P_4 \cos(\theta) \quad (4)$$

where P_2 and P_4 are the second and fourth order Legendre polynomials and β_2 and β_4 are the corresponding anisotropy parameters. A is a scaling factor. For prompt dissociation of a diatomic molecule, the b_2 parameter, can be in the range between +2 (purely parallel transition) and -1 (purely perpendicular transition), therefore the β_2 parameter extracted from the fit can then be related to the symmetry of the states in-

volved in the photolysis and the corresponding dynamics. In the case of the processes reported here, the β_2 parameter is the average of several steps (two-photon excitation to Rydberg state, further photon absorption then photolysis) therefore it does not quantify individual transition dynamics but shows an average and a "trend" of those dynamics. The b_4 parameter is usually associated with vector correlation effects, however considering the complexity of the processes involved (see eqn (1)–(3) above) it is unrealistic to interpret them in this way here.

Figure 2.6a shows β_2 values plotted for the various rings detected in images no. 8 and 10 (see Table 2-1) for the non-resonant process. These are shown along with the corresponding KERs plotted on a relative one-photon energy scale. A reasonably good agreement is found between the parameter values derived from the rings/KERs peaks of both images (no. 8 and 10) which have been assigned to common channels (see above), which further supports the validity of the assignments. The β_2 range from a value near +2, corresponding to a purely parallel transition for the CH_3(X; 0100) + Br* intermediates, to a negative value of about -0.2 corresponding to a significant contribution of a perpendicular transition for CH_3(X;0100) + Br.

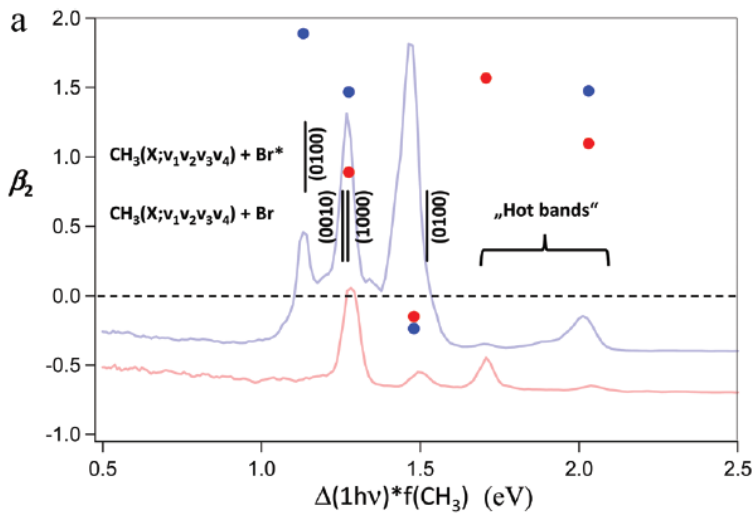

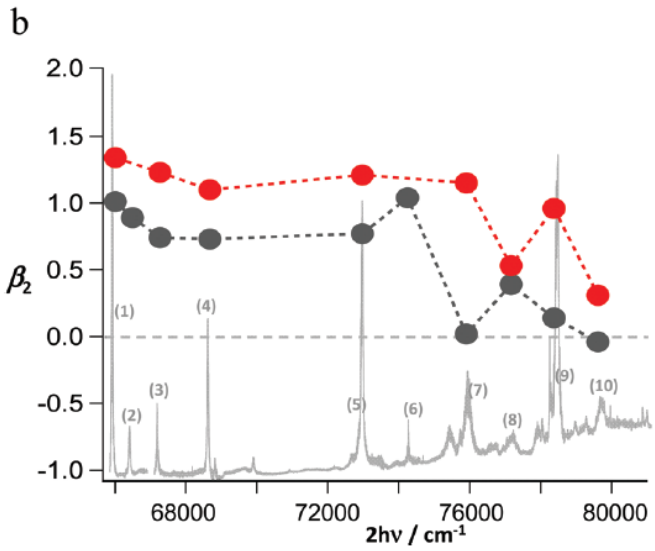

Figure 2.6 (a) Anisotropy parameters β_2 extracted from CH_3^+ images no. 8 (red dots) and 10 (blue dots) (see Table 1) as a function of the kinetic energy released (eV) along with the corresponding KER spectra plotted on a relative energy scale Δ(1hν)*f(CH3). Common energy thresholds for one-photon photodissociation process to form CH_3 (X;$\nu_1\nu_2\nu_3\nu_4$) + Br/Br* labelled as ($\nu_1\nu_2\nu_3\nu_4$) are indicated. ''Hot bands'': see Fig. 3a. (b) Anisotropy parameters β_2 extracted from CH_3^+ (grey dots) and Br^+ (red dots) images as a function of two-photon resonant excitations to CH_3Br Rydberg states along with the corresponding CH_3^+ REMPI spectrum. Image numbers are indicated (see Table 2-1).

Positive values of β_2 in the range of +0.8 to +1.6 obtained for CH_3 (X; 1000/0010) + Br and high KER hot bands which form CH_3(X; $\nu_1\nu_2\nu_3\nu_4$) + Br suggest dominating parallel transitions mixed with some character of perpendicular transitions. Since the ion formation mechanism involves a simple one-photon photodissociation step, the anisotropy will be largely determined by the symmetry change of the initial photoexcitation step from the ground state of CH_3Br(X; $\nu_1\nu_2\nu_3$) to the repulsive valence states $^3Q_1$, $^3Q_0$ and $^1Q_1$ which correlate with CH_3(X; $\nu_1\nu_2\nu_3\nu_4$) + Br/Br*.[23]

Considering symmetry alterations in possible transitions and the known shape of the potential energy surfaces involved[22] the following initial photoexcitation processes are proposed:

(i) Formation of CH_3(X; 0100) + Br*, where CH_3 is vibrationally excited by one quantum in the out-of-plane bending mode (ν_2), mainly occurs by a parallel transition to the $^3Q_0$ state followed by a dissociation on the same (i.e. the diabatic) potential curve.

(ii) Formation of CH_3(X; 1000/0010) + Br, where CH_3 is vibrationally excited by one quantum in a stretching mode (ν_1 and/or ν_3), occurs largely by a parallel transition to the $^3Q_0$ state followed by a curve crossing, i.e. a dissociation on the adiabatic potential curve.

(iii) Formation of CH_3(X; 0100) + Br, where CH_3 is vibrationally excited by one quantum in the out-of-plane bending mode (ν_2), occurs to a significant extent by perpendicular transitions to the $^3Q_1$ and/or $^1Q_1$ states followed by a dissociation on the same/diabatic potential curve.

(iv) Formation of CH_3(X; $v_1v_2v_3v_4$) + Br from vibrationally excited CH_3Br(X; $v_1v_2v_3$) largely occurs by a parallel transition to the $^3Q_0$ state followed by a dissociation on the adiabatic potential curve.

Since the resonant contributions to the CH_3^+ images and KERs mostly involve three-photon excitations via molecular Rydberg states prior to dissociation to form CH_3** Rydberg states (channel (2)) the anisotropy of the images will depend on the two-photon resonant step as well as the one-photon dissociation step and possible mixing of states involved.

Therefore it cannot be easily interpreted. We observe a trend (Figure 2.6, grey dots) of decreasing β_2 parameter (more perpendicular contribution) with increasing excitation energy. A correlation with the symmetry of the parent Rydberg state seems to exist: transitions through 5p and 4d Rydberg states of CH_3Br generate CH_3^+ with rather parallel distributions (β_2 ranging between 1.3 and 0.7) whereas 6p and 7p Rydberg states of CH_3Br generate CH_3^+ with almost isotropic distributions.

Br^+ images associated with the resonant excitations, both low and high KER components (see above), mostly display shapes corresponding to parallel transitions with positive values of b_2. Figure 2.6b (red dots) shows the b_2 values derived for the broad low KER peaks of the resonant transitions along with the corresponding values for the CH_3^+ signals. Comparison of the b_2 parameters of the signals for Br^+ and CH_3^+ reveals some correlation (common trend and analogous values of b_2) between the signals. This is to be expected for fragments formed by the same channel, prior to ionization, as proposed for CH_3** and Br/Br* (see eqn (2a)–(2c) above). Although close in value they are not identical; this can be attributed to the existence of some additional smaller contributions affecting the CH_3^+ and Br^+ distributions, such as dissociation of CH_3^+

(we do observe CH_2^+, CH^+ and C^+ ions as minor channels; discussion of these results was not included in this thesis and will be presented in a separate publication).

The no. 10 excitation Br^+ signal due to the non-resonant transition cannot be separated from the underlying resonant contribution of the same KER (~0.27 eV) which makes up about 2/3 of the signal (**Figure 2.4** and Figure 2.5). The total signal however, is found to display a close to isotropic shape (Figure 2.2d) with β_2 of about +0.24, suggesting that the non-resonant part of it (1/3 of the total) is significantly perpendicular in nature. This matches the observed angular distribution (and b_2 = 0.2) of the signal for CH^+ due to the formation of the corresponding CH_3(X, 0100) fragment which we believe to be the major fragment produced along with Br prior to ionization (see above and Figure 2.5).

2.3.4 Photoelectron Spectra

Images of photoelectrons were recorded for the excitations listed in Table 1. No negative ions were found to be present in the time-of-flight KER distributions (Figure 2.7) derived from the images. It is convenient to compare the photoelectron spectra with respect to the non-resonant contributions on a relative three-photon energy scale ($\Delta(3h\nu)*f(e)^3$; $\Delta(3h\nu) = 3h\nu_0 — 3h\nu_i$; $f(e) = m(CH^+)/m(CH_3) \sim 1$; see text above for comparison and definitions) and those with respect to the resonant contributions on a relative one-photon energy scale ($D(1h\nu) = 1h\nu_0 — 1h\nu_i$).

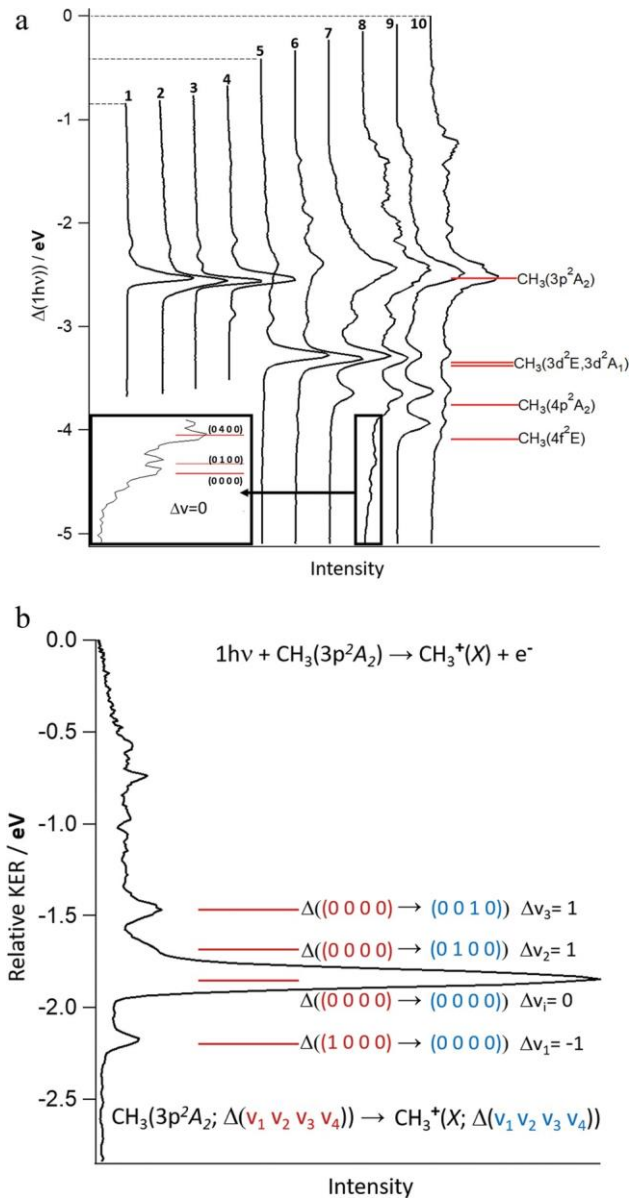

Figure 2.7 Photoelectron spectra (PES), (a) derived from images no. 1–10 (see Table 1), plotted as a function of a relative energy scale Δ(1*h*ν) (see explanation in the main text) and tilted to the right (*i.e.* plotted vertically). Common energy thresholds (energy maxima) for ionization of Rydberg states of CH_3 (CH_3(Ry)) after its formation along with Br/Br* by three- photon photodissociation of CH_3Br are indicated. The inset shows detail of the PES no. (8) at high energy with thresholds for ionization of CH_3(X; $v_1v_2v_3v_4$) and its formation along with Br/Br*. (b) For image no. 4 plotted as a function of the relative kinetic energy released (eV) tilted to the right (*i.e.* plotted vertically). Energy thresholds (energy maxima) for specific one- photon ionization processes of CH_3**($3p^2A_2$; $v_1v_2v_3v_4$) states to form CH_3^+(X; $v_1v_2v_3v_4$), after its formation along with Br/Br* by three-photon photodissociation of CH_3Br, are indicated by ($v_1v_2v_3v_4$) numbers. Assignments of ionization processes with respect to changes in vibrational quantum numbers (Δv_i) are shown, furthest to the right.**

Figure 2.7 shows the photoelectron spectra plotted on the relative one-photon energy scale, where the zero kinetic energy release of no. 10/79 610 cm^{-1} has been set to zero (reference spectrum). Thresholds corresponding to ionization of specific

CH_3** states (formed along with Br/Br*) line up in the plot. One photoelectron peak dominates the four lowest energy excitations (*i.e.* images/KERs no. 1–4; Table 1) which match in Fig. 7a. The peaks correspond to the formation of the CH_3** ($3p^2A_2$) Rydberg state. These PESs correspond to the images/KERs which show vibrational structures (see above). Small satellite peaks close by are indicative of vibrational excitations and hot bands as shown in Fig. 7b for excitation no. 4. The next two excitations (no. 5 and 6) generate photoelectron peaks that shift to higher energy but also match each other, corresponding to one-photon ionization of the CH_3 ** ($3d^2E$) and/or CH_3 ** ($3d^2A$) states that lie close in energy. Finally, excitations no. 7–10 exhibit several photoelectron peaks corresponding to ionization of different CH_3 Rydberg states ($3p^2A_2$, $3d^2E$, $3d^2A_1$, $4p^2A_2$) as listed in Table 1. The PES structures of no. 8/77 165 and no. 10/ 79610 cm^{-1}, which correspond to significant non-resonant contributions, are less clear. However, there are some indications of ionization/formation of $CH_3(X; v_1v_2v_3v_4)$ species based on weak high kinetic energy electron peaks as shown by the inserted figure expansion for no. 8 in Figure 2.7.

2.4 Discussion

As noted in the previous section, REMPI, slice and photoelectron imaging data converge on the existence of two major pathways when CH_3Br is excited at wavenumbers corresponding to two-photon transitions to reach rovibrational levels of molecular Rydberg states in the 66 000 to 80 000 cm^{-1} region:

(a) two-photon-resonant transitions, followed by one-photon absorption to give $CH_3(X)/CH_3$** + Br/Br* and

(b) non-resonant, one-photon photolysis towards $CH_3(X)$ + Br/Br*. These two pathways will now be discussed.

2.4.1 Resonant processes

The results relevant to the resonant spectra contributions, as presented above, can be interpreted as being due to dissociations on excited state potential energy surfaces to form (a) Rydberg states of CH_3 (CH_3**) along with Br/Br* or (b) ground state $CH_3(X)$ along with Br/Br* prior to ionization of either CH_3 or Br. This occurs after a total of three-photon excitation to metastable superexcited molecular states ($CH_3Br^{\#}$)

via two- photon accessible Rydberg states (Figure 2.8). Formation of $CH_3(X)$ directly following the two-photon resonant excitation (*i.e.* by predissociation of the resonance-excited molecular Rydberg states) was not detected. Whereas a minor contribution of such a channel cannot be ruled out, the results suggest that its probability is low.

In the case of the metastable molecular state(s) ($CH_3Br^{\#}$), prior to dissociation the excess energy can be redistributed among the molecule's internal degrees of freedom to form fragments of relatively low translational energy but high internal (rovibrational) energy, typically appearing as broad KER spectral peaks for the CH_3 and Br fragments. The relatively low KER, broad spectral structures of the KERs observed for the resonant contributions suggests that step (2b) involves such a mechanism. The $CH_3Br^{\#}$ state(s), being higher in energy than the ionization limit, is (are) most likely one or more super- excited state(s) belonging to a Rydberg series converging to an excited ionic state (*i.e.* $CH_3Br^{\#} = [CH_3Br^{+}*]nl;o$). This involves an one-photon excitation within the ion core of the resonant Rydberg state ($CH_3Br** = [CH_3Br^{+}]nl;o$) to make an overall two-electron transfer to form $CH_3Br^{\#}$.

Looking at a summary of the CH_3** Rydberg states detected (Table 1) there seems to be a correlation between the formation of CH_3**(Ry) and excitations to CH_3Br**(Ry) with respect to the Rydberg electron orbital symmetries (*l* quantum numbers). Thus, the 3p Rydberg state of CH_3 (CH_3**($3p^2A_2$)) is primarily formed *via* excitation to the 5p Rydberg state of CH_3Br and the 3d Rydberg state(s) of CH_3 (CH_3**($3d^2E$; $3d^2A_1$)) is (are) largely formed *via* excitation to the 4d Rydberg state of CH_3Br. This must be associated with a conservation of momentum during the combined process of one-photon excitation of CH_3Br** to $CH_3Br^{\#}$ and its dissociation on an excited state potential sur- face to form CH_3** and Br/Br*. Furthermore, an increasing number and changing proportion of CH_3** states are formed as the excitation energy increases (Table 1 and Figure 2.7a). This should be associated with an opening of an increasing number of channels to form CH_3** + Br/Br* and/or changes in transition probabilities along different surfaces as the energy increases. The disappearance of the vibrational structure assigned to the CH_3**($3p^2A_2$) state (see Section III.B) for excitation energies beyond that for no. 4 (Figure 2.3) is a further indication of an increasing contribution of CH_3** states and overlapping vibrational structures.

Whereas, no multiphoton dissociation studies for resonant excitations *via* p and d Rydberg states of CH_3Br exist in the literature, Wang *et al.* have reported studies of excitations *via* lower energy 5s Rydberg states.[19] Images and corresponding KERs for CH_3^+ are found to show comparable structures to those reported here, appearing as broad peaks with vibrational structures at low KERs and sharp peaks at medium high kinetic energies. These observations, however, are interpreted differently as being due to photodissociation of the parent molecular ions $CH_3Br^+(X)$ to form $CH_3^+(X)$ along with Br* and Br, respectively. Furthermore, rings/sharp KER peaks observed at still higher KERs are proposed to be due to two-photon resonant photodissociations to form $CH_3(X)$ along with Br and Br*.

2.4.2 Non-resonant processes

The results relevant to the non-resonant contributions, as presented above, can be interpreted as being due to one- photon excitations to repulsive electronic valence states (CH_3Br^*) followed by dissociation. This agrees with the observed increase in the corresponding spectral continuum with photon energy (Figure 2.1a) in accordance with an increasing absorption (*i.e.* one-photon) cross section in the excitation region (see Figure 2.8).[3,9] Relatively large signals appearing as rings in the images/sharp KERs peaks, due to the non-resonant contributions were seen for the excitations which show relatively large underlying non-resonant contributions in the REMPI spectra (see Figure 2.1a), *i.e.* in images/KERs no. 8 and 10 for CH_3^+ (Figure 2.3) and in no. 10 for Br^+ (Figure 2.4).

Photodissociation studies in the first continuum absorption band (A band) of CH_3Br have been performed by a number of groups.[13-15,22-25] The reported value for β_2 of 1.9 ±0.1 for CH_3(X; 0100) formation along with Br* for 251.00 nm excitation[23] agrees with our value (1.9) for the corresponding fragment formation for 251.28 nm one-photon excitation (no. 10/79 610 cm^{-1}) and the value for b_2 of 0.2 0.2 for CH_3(X; 0100) along with Br for 251.00 nm excitation[22] is of an intermediate size analogous to our values of -0.15 and -0.24 for the corresponding fragment formation derived for the 259.23 (no. 8/77 165 cm^{-1}) and 251.28 nm (no. 10/79 610 cm^{-1}) excitations, respectively. Furthermore, our upper limit value of β_2 = +0.24, largely due to the formation of Br along with CH_3(X; 0100) (see Appendix B) for 251.28 nm one-photon

excitation can be compared with the values of about zero for excitations in the region of 251–278 nm.[23] Thus, the formation of $CH_3(X)$ in the out-of-plane bending mode along with Br is found to display isotropic to perpendicular fragment angular distributions, whereas its formation along with Br* displays a parallel angular distribution. This is in agreement with previous observations and has been shown to be consistent with a strong non- adiabatic coupling between spin–orbit states of the parent molecule.[23]

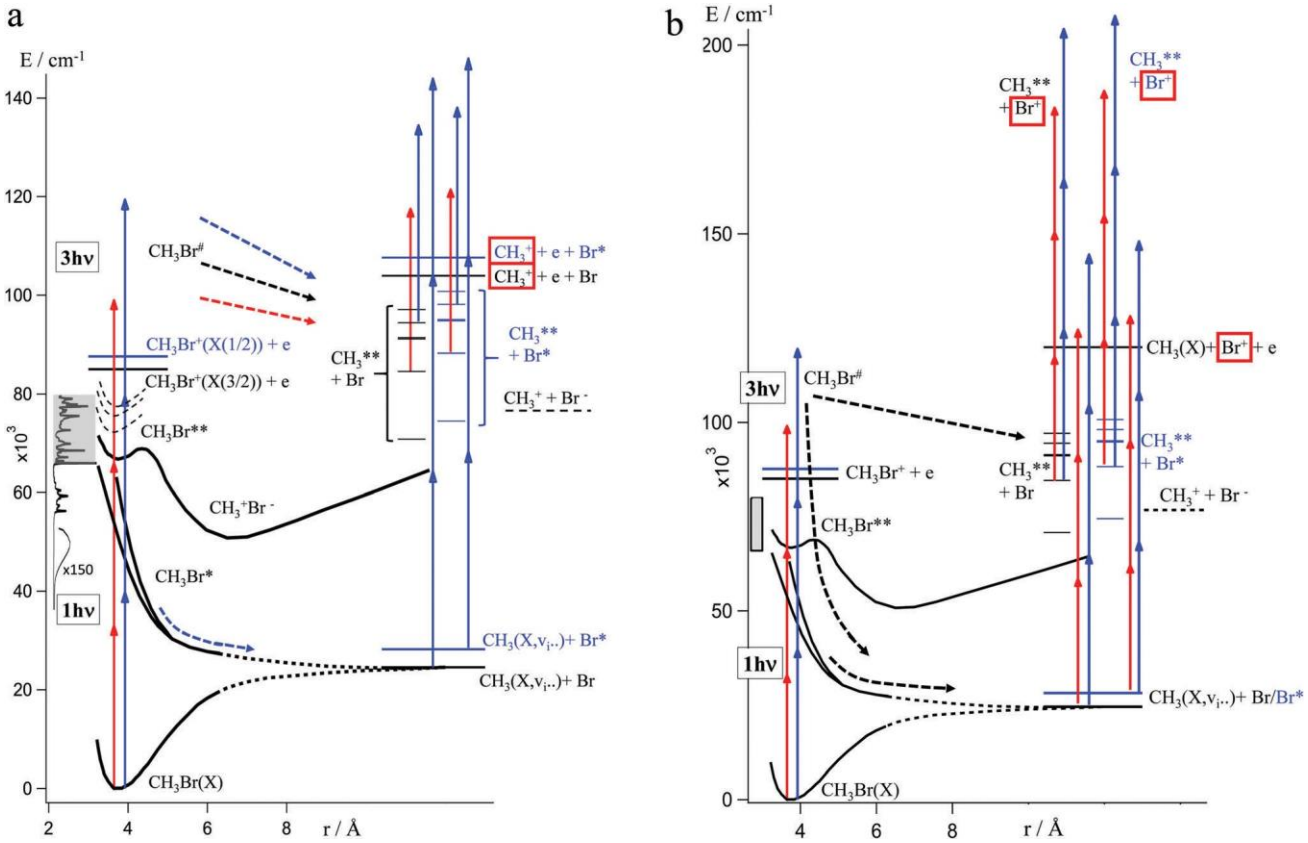

Figure 2.8 Schematic energy diagrams for excitation processes of CH_3Br leading to CH_3^+ (a) and Br^+ (b) formation showing calculated potential energies as a function of the CH_3–Br bond distance[18,27] as well as relevant energy thresholds and transitions. Red vertical arrows correspond to the two-photon resonant transition of 66 019 cm^{-1} (excitation no. 1) and blue vertical arrows correspond to the two-photon resonant transition 79 610 cm^{-1} (excitation no. 10) (see Table 1). Broken arrows indicate paths of photodissociation processes as marked in boxes (see main text). The two-photon resonance scanning region is indicated by grey shaded boxes. The one-photon absorption spectrum[3,9] is tilted to the right (*i.e.* plotted vertically) in figure (a).

CH_3^+ and Br^+ ion slice images as well as photoelectron velocity map images were recorded for multiphoton excitation of CH_3Br at ten wavelengths involving two photon resonant tran-

sitions to np and nd vibrational levels of molecular Rydberg states (CH_3Br^{**}(Ry; $v_1v_2v_3$)) between 66 000 and 80 000 cm^{-1} (Table 2-1). At all wavelengths CH_3^+ is the majority of the ion signal (Figure 2.1). Kinetic energy release spectra (KERs) as well as angular distributions and relevant fit parameters (b_2 and b_4) were derived from the ion slice images. Photoelectron spectra were derived from the photoelectron images.

The majority of the photoelectrons formed are due to one- photon ionization of different Rydberg states of methyl photofragments (CH_3^{**}). These states are formed by two-photon- resonant excitation to an np or nd vibrational levels of parent Rydberg states followed by one-photon excitation to metastable, superexcited molecular states ($CH_3Br^{\#}$) which then dissociate towards CH_3^{**}(Ry; $v_1v_2v_3v_4$) + Br/Br*. This contribution dominates all but two excitation wavelengths used in this work. A correlation is found between the angular momentum quantum numbers (l) of the resonantly excited molecular Rydberg states, CH_3Br^{**} and the CH_3 Rydberg states formed.

For the highest excitation energies, two additional channels are found to be present. The first channel is a dissociation of the metastable, superexcited $CH_3Br^{\#}$ states towards CH_3(X; $v_1v_2v_3v_4$) + Br/Br* which generates fast CH_3^+ and Br^+ ions. The second channel is the formation of CH_3(X; $v_1v_2v_3v_4$) + Br/Br* assigned as a one-photon photolysis *via* the A band with angular distributions of CH_3 and Br/Br* fragments agreeing well with the literature.

The results of this analysis add to information relevant to the energetics and fragmentation processes of the methyl halides. It will hopefully render further theoretical interpretation of the characteristic processes involved in the very interesting dynamics observed here. Furthermore, the content of this paper is of relevance to various intriguing fields. The observed involvement of high energy superexcited molecular states in the formation of halogen atom radicals and fragment ions and electrons is of relevance to further understanding of atmospheric photochemistry as well as plasma chemistry/physics. Selective photoexcitation to form the reactive electronically excited state of the CH_3, as identified, could be of interest for organic photosynthesis purposes.

2.5 References

[1] D. E. Robbins, Photodissociation of Methyl-Chloride and Methyl-Bromide in Atmosphere, *Geophys. Res. Lett.*, 1976, 3(4), 213–216.

[2] D. E. Robbins, Correction, Geophys. Res. Lett.,1976,3(12), 757.

[3] L. T. Molina, M. J. Molina and F. S. Rowland, Ultraviolet- Absorption Cross-Sections of Several Brominated Methanes and Ethanes of Atmospheric Interest, *J. Phys. Chem.*, 1982, 86(14), 2672–2676.

[4] N. J. Warwick, J. A. Pyle and D. E. Shallcross, Global modelling of the atmospheric methyl bromide budget, *J. Atmos. Chem.*, 2006, 54(2), 133–159.

[5] Ozone-Depleting Substances. https://www.epa.gov/ozone- layer-protection/ozone-depleting-substances.

[6] W. C. Price, The Far Ultraviolet Absorption Spectra and Ionization Potentials of the Alkyl Halides. Part I, *J. Chem. Phys.*, 1936, 4(9), 539–547.

[7] G. C. Causley and B. R. Russell, Vacuum Ultraviolet-Absorption Spectra of Bromomethanes, J. Chem. Phys.,1975, 62(3), 848–857.

[8] S. Felps, P. Hochmann, P. Brint and S. P. McGlynn, Molecular Rydberg Transitions; The lowest-Energy Rydberg Transitions of s-Type in CH_3X and CD_3X, X = Cl, Br, and I, *J. Mol.Spectrosc.*, 1976, 59, 355–379.

[9] R. Locht, B. Leyh, H. W. Jochims and H. Baumgartel, The vacuum UV photoabsorption spectrum of methyl bromide (CH_3Br) and its perdeuterated isotopomer CD_3Br: a Rydberg series analysis, *Chem. Phys.*, 2005, 317(1), 73–86.

[10] R. Locht, B. Leyh, D. Dehareng, H. W. Jochims and H. Baumgartel, The vacuum UV photoabsorption spectrum of methyl bromide (CH_3Br) and its perdeuterated isotopomer CD_3Br: a vibrational analysis, *Chem. Phys.*, 2005, 317(1),87–102.

[11] A. Kvaran, H. Wang, K. Matthiasson and A. Bodi, Two-Dimensional (2 + n) REMPI of CH_3Br: Photodissociation Channels via Rydberg States, *J. Phys. Chem. A*, 2010, 114,9991–9998.

[12] G. N. A. Van Veen, T. Baller and A. E. De Vries, Photofragmentation of CH3Br in the A-Band, *Chem. Phys.*, 1985, 92(1),59–65.

[13] W. P. Hess, D. W. Chandler and J. W. Thoman, Photofragment imaging: the 205 nm photodissociation of CH_3Br and CD_3Br, *Chem. Phys.*, 1992, 163(2), 277–

286.

[14]T. Gougousi, P. C. Samartzis and T. N. Kitsopoulos, Photodissociation study of CH_3Br in the first continuum, *J. Chem.Phys.*, 1998, 108(14), 5742–5746.

[15] V. Blanchet, P. C. Samartzis and A. M. Wodtke, UV photodissociation of methyl bromide and methyl bromide cation studied by velocity map imaging, *J. Chem. Phys., 2009,130, 3.*

[16] D. A. Shaw, D. M. P. Holland and I. C. Walker, Ion-pair formation mechanisms in chloromethane, bromomethane and dichlorodifluoromethane, *J. Phys. B: At., Mol. Opt. Phys.*, 2006, 39(17), 3549–3560.

[17] D. D. Xu, J. H. Huang, R. J. Price and W. M. Jackson, Velocity Imaging Studies on Ion-Pair Dissociation of $CH_3Br + hv(_{VUV}) \rightarrow CH_3^+ + Br^-$ as a Function of Wavelength, *J. Phys.Chem. A*, 2004, 108(45), 9916–9923.

[18] C. Escure, T. Leininger and B. Lepetit, Ab initio study of methyl-bromide photodissociation in the A band, *J. Chem.Phys.*, 2009, 130(24), 244305.

[19] F. Y. Wang, M. L. Lipciuc, X. M. Yang and T. N. Kitsopoulos,Multiphoton dissociation dynamics of CH_3Br, *Phys. Chem.Chem. Phys.*, 2009, 11(13), 2234–2240.

[20] T. Ridley, J. T. Hennessy, R. J. Donovan, K. P. Lawley,S. Wang, P. Brint and E. Lane, Evidence for Rydberg doorway states in photoion pair formation in bromomethane, *J. Phys. Chem. A*, 2008, 112(31), 7170–7176.

[21] Mulliken, R. Intensities In Molecular Electronic Spectra X. Calculations On Mixed-Halogen, Hydrogen Halide, Alkyl Halide, And Hydroxyl Spectra. *The Journal of Chemical Physics* 1940, *8*, 382-395.

[22] G. N. A. Vanveen, T. Baller and A. E. De Vries, Photofragmentation of CH_3Br in the A-Band, *Chem. Phys.*, 1985, 92(1),59–65.

[23] J. G. Underwood and I. Powis, Photofragmentation of CH_3Br in red wing of the first continuum absorption band, *Phys.Chem. Chem. Phys.*, 2000, 1, 747–756.

[24] F. Y. Wang, M. L. Lipciuc, A. Kartakoullis, P. Glodic,P. C. Samartzis, X. M. Yang and T. N. Kitsopoulos, Slice imaging of methyl bromide photofragmentation at 193 nm, *Phys. Chem. Chem. Phys.*, 2014, 16(2), 599–606.

[25] M. L. Lipciuc and M. H. M. Janssen, High-resolution slice imaging of quantum state-to-state photodissociation of methyl bromide, J. *Chem. Phys.*, 2007, 127, 224310.

[26] Y. Song, X. M. Qian, K. C. Lau, C. Y. Ng, J. B. Liu and W. W. Chen, High-resolution energy-selected study of the reaction $CH_3X^+ \rightarrow CH_3^+ + X$: Accurate thermochemistry for the CH_3X/CH_3X+ (X = Br, I) system, *J. Chem. Phys.*, 2001,115(9), 4095–4104.

[27] X. Tang, X. Zhou, Z. Sun, S. Liu, F. Liu, L. Sheng and B. Yan,Dissociation of internal energy-selected methyl bromide ion revealed from threshold photoelectron-photoion coincidence velocity imaging, *J. Chem. Phys.*, 2014, 140, 044312.

[28] C. Escure, T. Leininger and B. Lepetit, Ab initio study of valence and Rydberg states of CH_3Br, *J. Chem. Phys.*, 2009,130(24), 244306.

[29] H. R. Hrodmarsson, A. Kartakoullis, D. Zaouris, P. Glodic,H. Wang, P. C. Samartzis and A. Kvaran, Excitation Dynamics Involving Homogeneous Multistate Interactions:One and Two Color VMI and REMPI of HBr, *Phys. Chem.Chem. Phys*., 2017, 19(18), 11354–11365.

[30] H. R. Hrodmarsson and A. Kvaran, Revealing photofragmentation dynamics through interactions between Rydberg states: REMPI of HI as a case study, *Phys. Chem. Chem.* Phys.,2015, 17, 32517.

[31] H. R. Hrodmarsson, H. Wang and A. Kvaran, State interactions and illumination of hidden states through perturbations and observations of new states: High energy resonance enhanced multiphoton ionization of HI, *J. Chem. Phys.*,2015, 142(24), 244312.

[32] J. Long, H. Wang and A. Kvaran, Phtofragmentation, state interactions, and energetics of Rydberg and ion-pairstates:Resonance enhanced multiphoton ionization via E and V(B)states of HCl and HBr, *J. Chem. Phys*., 2013, 138(4), 044308.

[33] P. Glodic, D. Zaouris, P. C. Samartzis, A. Haflijason and A. Kvaran, Effect of a triplet to singlet interaction on photofragmentation dynamics: Highly excited states of HBr probed by VMI and REMPI as a case study, Phys. *Chem.Chem. Phys*., 2016, 18(37), 26291–26299.

[34] D. Zaouris, A. Kartakoullis, P. Glodic, P. C. Samartzis,H. R. Hrodmarsson and A. Kvaran, Rydberg and valence state excitation dynamics: a velocity map imaging study

involving the E-V state interaction in HBr, Phys. Chem.Chem. Phys., 2015, 17(16), 10468–10477.

[35] C. R. Gebhardt, T. P. Rakitzis, P. C. Samartzis,V. Ladopoulos and T. N. Kitsopoulos, Slice Imaging: A New Approach to Ion Imaging and Velocity Mapping, *Rev.Sci. Instrum.*, 2001, 72(10), 3848.

[36] V. Papadakis and T. N. Kitsopoulos, Slice Imaging and Velocity Mapping Using a Single Field, *Rev. Sci. Instrum.*,2006, 77(8), 5.

[37] B. Zhang, J. Zhang and K. Liu, Imaging the ‘‘missing’’ bands in the resonance-enhanced multiphoton ionization detection of methyl radical, *J. Chem. Phys.*, 2005, 122, 104310.

[38] NIST Chemistry WebBook - (National Institute of Standardsand Technology) https://webbook.nist.gov/chemistry/nameser/,accessed Jan 2018.

3 Production of highly excited Rydberg Iodine atoms from photolysis of CH_3I: a Rydberg series dynamical analysis

3.1 Introduction

Methyl iodide (CH_3I) is a very interesting molecule to study, due to its rich dynamics and because of its role in atmospheric chemistry. It is present in the atmosphere and the oceans[1] and the products of its photodissociation, influence numerous atmospheric processes. High energy CH_3 or I radicals along with other types of highly reactive iodocarbons[2] engage in redox reactions perturbing the natural cycles of chemical species from marine-atmosphere interfaces[3,4] up to the troposphere[5,6,7]and the stratosphere7[,8], increasing the overall reactivity of the atmosphere. Moreover, recently, iodine chemistry was shown to play an important role in ozone depletion.[9,10] At even higher layers of the atmosphere, towards the ionosphere, chemical species interact with solar VUV radiation and formation of highly reactive species and ions takes place.[11]

Methyl iodide is a benchmark system in dynamics and has been explored experimentally[12,13] and theoretically[14,15], especially as a model system for non-adiabatic curve-crossing.[16].Methyl iodide studies were focused mostly on two regions of its absorption spectrum, known as the A and the B bands. The A band (220-350 nm) displays no structure, therefore is characterized by transitions between repulsive states. It was studied in great depth by several groups in nanosecond and femtosecond timescales, therefore a comprehensive image of its dynamics is established.[12,]**Error! Bookmark not defined.**[,]**Error! Bookmark not defined.**[,17]The B band (190-205 nm) displays vibrational structure, thus has more bound character and it is also well studied.[18,19,16,]**Error! Bookmark not defined.**[,]**Error! Bookmark not defined.**[,]**Error! Bookmark not defined.** Overall, photolysis in the A or B band leads to formation of CH_3 radical in its ground electronic and vibrational states or vibrationally excited in the umbrella v_2 or stretch v_1 modes with 1-4 vibrational quanta (X, v_1=1-4 or v_2=1-4) along with I in its ground state or spin-orbit excited $I(^2P_{3/2})/I(^2P_{1/2})$.

Here, we report on the dynamics of higher excited states of CH_3I. We probe the photoproducts following the two-photon resonant excitation of CH_3I to selected states from the Rydberg series in the energy range of 55000-70000 cm^{-1}(See Table 3-1) as shown at the high resolution absorption spectra recorded by S. Eden *et al.*[20] Photoelectron Velocity Map Images and ion Slice images revealed that the excess photon energy is channeled into the I photofragment resulting in the production of highly excited Rydberg Iodine atoms in various quantum states.

3.2 Experimental

In Table 3-1, the excitation wavelength of the specific states under study along with their Rydberg term and the converging CH_3I^+ state is displayed. Each excitation is assigned a number to facilitate subsequent reference in the text and several excitations are classified in groups (A, B or C) according to the iodine state range produced after the dissociation process (see further in the text).

Table 3-1 : CH_3I Molecular Rydberg states selected for excitation including the number assignments used further in the text along with the Rydberg terms and the 1hv excitation wavelengths and 2hv excitation wavenumbers.

No.	Laser wavelength λ/nm	2hv excitation energy /cm^{-1}	Rydberg Term	Converging CH_3I^+ state	Group
1	359.062	55700.63	6s(3/2)+v_3	$^2E_{1/2}$	
2	339.404	58926.84	6p(0…)#	$^2E_{3/2}$	A
3	336.913	59362.38	6p(3/2)+ v_3	$^2E_{3/2}$	
4a	336.357	59461		$^2E_{3/2}$	
4b	335.735	59531.76		$^2E_{3/2}$	
4c	333.902	59898		$^2E_{3/2}$	
6	324.481	61636.86	6p(3/2)+nv_1	$^2E_{3/2}$	B
7	317.095	63072.53	5d(0,…)#	$^2E_{3/2}$	
8	310.116	64492.07	6p(0,…)#	$^2E_{1/2}$	
9	309.111	64701.77		$^2E_{3/2}$	
10	298.793	66935.92	7s(3/2)+nv_2	$^2E_{3/2}$	C
11	294.185	67984.44	7p(0,…)#	$^2E_{3/2}$	
12	286.602	69783.06	7s(0,…)#	$^2E_{1/2}$	

The VMI/Slice Imaging setup described in Chapter 1, was used for this work. Methyl iodide molecules are prepared in their electronic ground state via a supersonic molecular beam comprised of CH_3I vapor seeded in He. The beam is created via adiabatic expansion through a home-made piezoelectrically-actuated nozzle valve (ø1mm orifice) and collimated by a skimmer (ø1.5 mm, Beam Dynamics) prior to entering the interaction region. A stagnation pressure of P_0 ~ 1 bar is used. The photolysis / ionization laser beam is focused (f = 30 cm) on the geometric focal point of a two electrode repeller-extractor arrangement where it intersects the molecular beam at right angles. The laser beam (typically 1 mJ/pulse) is generated by an excimer-pumped (Lambda Physik LPX, operating with XeCl) pulsed-dye laser (LPD3000) and the appropriate dyes were used to cover the whole excitation range.

For the slicing experiments, the repeller is pulsed ON at optimized time delays (~300 ns) following the photolysis/ionization allowing the ion sphere to expand. The charged photofragments traverse a field-free time-of-flight region (45 cm) and the center slice of the ion sphere is selectively detected by a position-sensitive detector (dual, imaging-quality MCP array coupled to a phosphor screen) coupled to a CCD camera. The image frame is recorded asynchronously every second (~10 laser shots) by the camera and several thousand frames are averaged to form images such as those shown in the Results section. Each final image is integrated over angle to extract the speed and over radius to extract the angular distributions of the corresponding fragments**.** For the photoelectron images recording, the repeller is negatively charged and both the repeller electrode and the detector are not gated (i.e. they are always ON).

3.3 Results

3.3.1 Photoelectron Velocity Map Images

Velocity map photoelectron images were recorded, mapping the quantum states of ionized photoproducts following two-photon resonant excitation to selected Rydberg states of CH_3I (See Table 3-1) and subsequent processes. Representative raw photoelectron images are displayed in Figure3.1 and all images are available in Appendix C. A colour map ranging from red to yellow is chosen to indicate regions of different relative intensity, where bright yellow stands for high intensity. Labels of I states (see below) are indicated in the images to draw attention to the fact that different states

exhibit stronger signals in different excitations. A list of the energies and terms of the relevant atomic iodine states is reproduced[21] in Table 3-2. The photoelectron images proved critical for the identification of the channels involved.

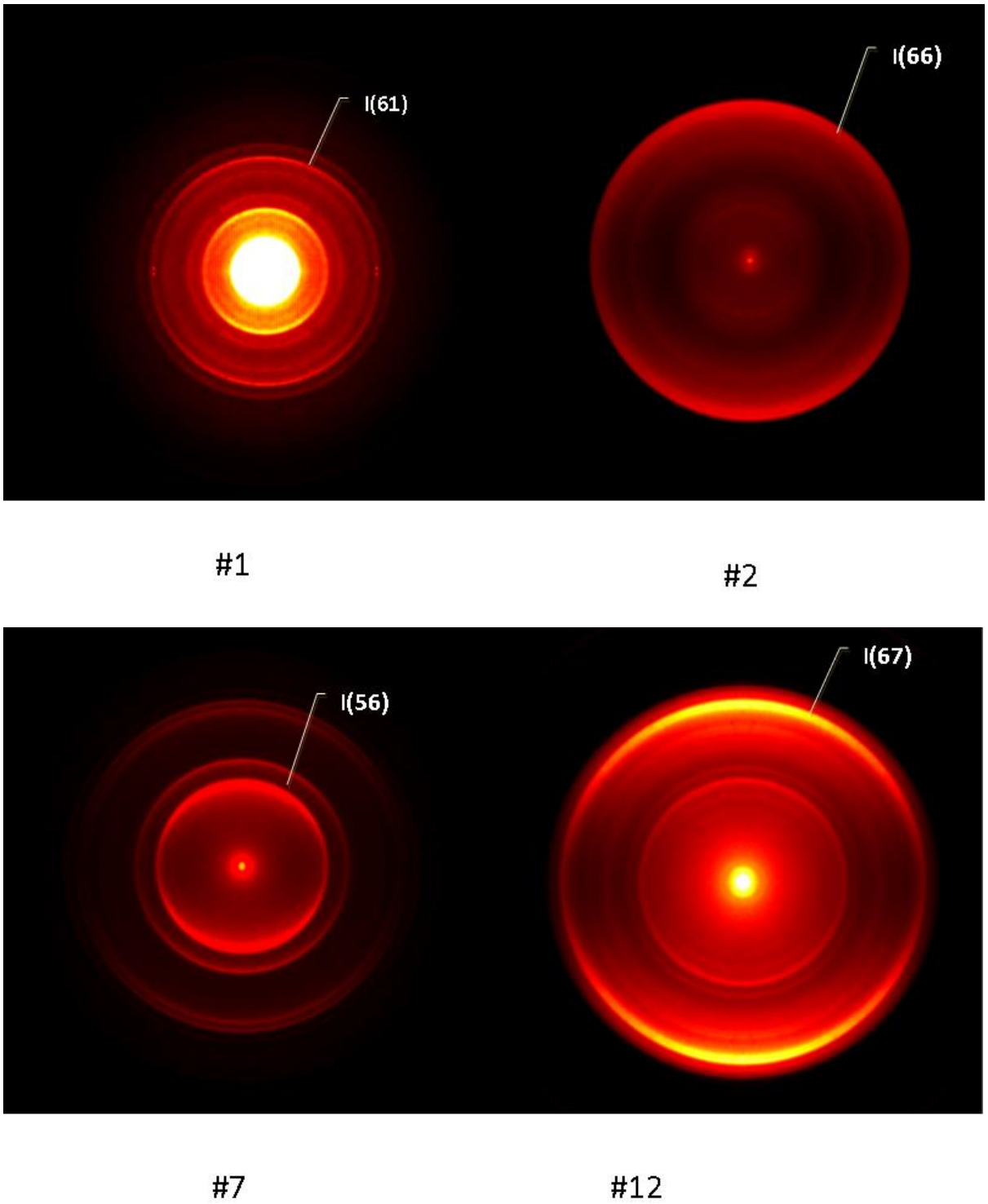

Figure3.1 : Photoelectron raw images from selected excitations no. 1, 2, 7 and 12. Colours have been adjusted for all the features to be distinguishable. The main state of excited I produced in each excitation is depicted in relation to the corresponding ring.

Table 3-2 Relevant iodine atomic energy states (Reproduced from Ref 21.) along with the Rydberg excitation schemes (see Table 3-1)where they were observed.

Configuration	Term	J	Level /cm^{-1}	Notation used	No. of Rydberg excitation
$5s^25p^5$	$^2P^o$	3/2	0.000	I	9
		1/2	7602.970	I*	9
$5s^25p^4(^3P_2)6s$	^2D	5/2	54633.460	I (54)	2,3,4b,6,7,8,9,10,11,12
		3/2	56092.881	I (56)	2,3,4b,6,7,8,9,10,11,12
$5s^25p^4(^3P_0)6s$	^2S	1/2	60896.243	I (60)	3,4a,6,7,8,9
$5s^25p^4(^3P_1)6s$	^2P	3/2	61819.779	I (61)	4a,4b,4c,7,8,9,10,11,12
		1/2	63186.758	I (63)	4b,8,9,10,11,12
$5s^25p^4(^3P_2)6p$	$^2D^o$	5/2	64906.290	I (64)	2,3,4c,10,11,12
		3/2	64989.994		
$5s^25p^4(^3P_2)6p$	$^2F^o$	5/2	65644.476	I (65)	4a,4b,10,11,12
		7/2	65669.988		
$5s^25p^4(^3P_2)6p$	$^2P^o$	1/2	65856.960		
		3/2	67062.130	I (67)	4a,10,11,12
$5s^25p^4(^3P_2)5d$	^2F	7/2	66015.023	I (66)	2,3,4a,10,11,12
		5/2	66020.469		
$5s^25p^4(^3P_2)5d$	^2P	3/2	66355.093		
		1/2	67298.328	I (67)	4a,4b,10,12
$5s^25p^4(^3P_2)5d$	^2G	9/2	67726.415		
		7/2	68559.540	I (68)	12
$5s^25p^4(^1D_2)6s$	^2D	3/2	68549.743		
		5/2	68587.859		
$5s^25p^4(^3P_2)5d$	^2S	1/2	68615.734		

Kinetic Energy Release spectra (KERs) were derived from the images and shown in Figure **3.2** and Figure 3.3. Photoelectron spectra suggest the existence of highly excited iodine in a range of states dependent on the initial excitation.

Photoelectrons from the ionization of the neutral photoproducts (CH_3 and I in several excited quantum states) are produced via a one photon process.

$I^{**} + 1hv \rightarrow I^{+} + e^{-}$ (1)

$CH_3^{**} + 1hv \rightarrow CH_3^{+} + e^{-}$ (2)

The species $CH_3I(X)$, I ($^2P_{3/2}$) and I*($^2P_{1/2}$) require three photons to get ionized:

$$I/I^{*} + 3hv \rightarrow I^{+} + e^{-}\ (3) CH_3I + 3hv \rightarrow CH_3I^{+}\ (^2E_{3/2,1/2})\ (4)$$

We have separated the Rydberg states under study into three groups denoted as A, B, C (see Table 3-2) based on the resulting quantum states of iodine produced. An energy shift relative to the photodissociation of CH_3I taking place at 69783 cm^{-1} (the highest energy excitation) is introduced to the rest of the KERs to account for the change in photolysis wavelength. In this way, common channels appear in the same position in the x-axis (ΔKER/eV) and comparison between the different excitations is more straightforward. Since the ionization processes of interest involved require one or three photons, comparison using a 1hv and a 3hv relative energy shift is presented. The maximum kinetic energy ionization thresholds for several I and CH_3 states, in each case, are indicated by vertical lines in the figure.

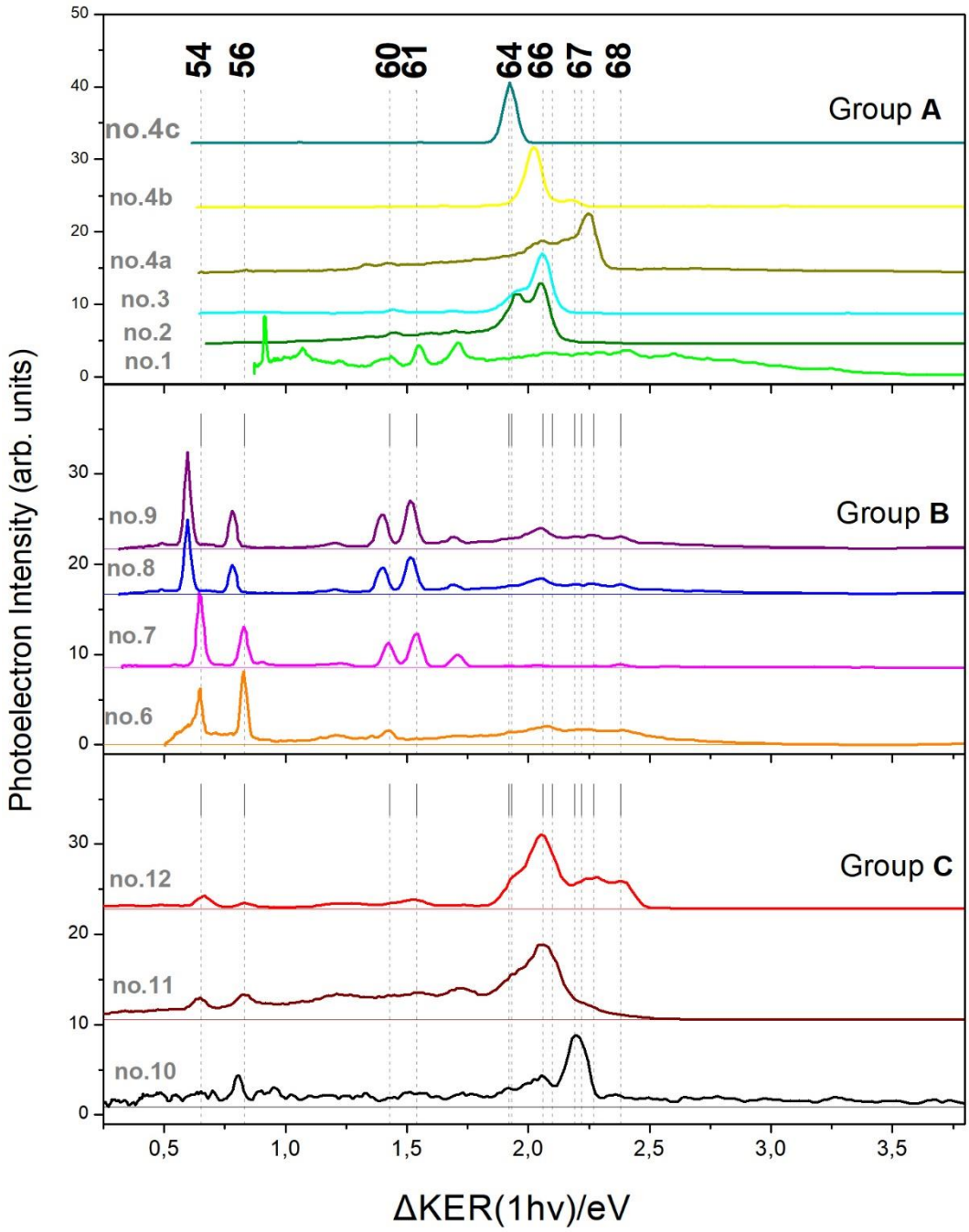

Figure 3.2 : Photoelectron KER distributions for the Rydberg states belonging to Groups A, B and C on a relative energy scale for 1hv ionization processes. The maximum kinetic energy thresholds for the creation of relevant I and CH_3 ions are indicated by vertical lines.

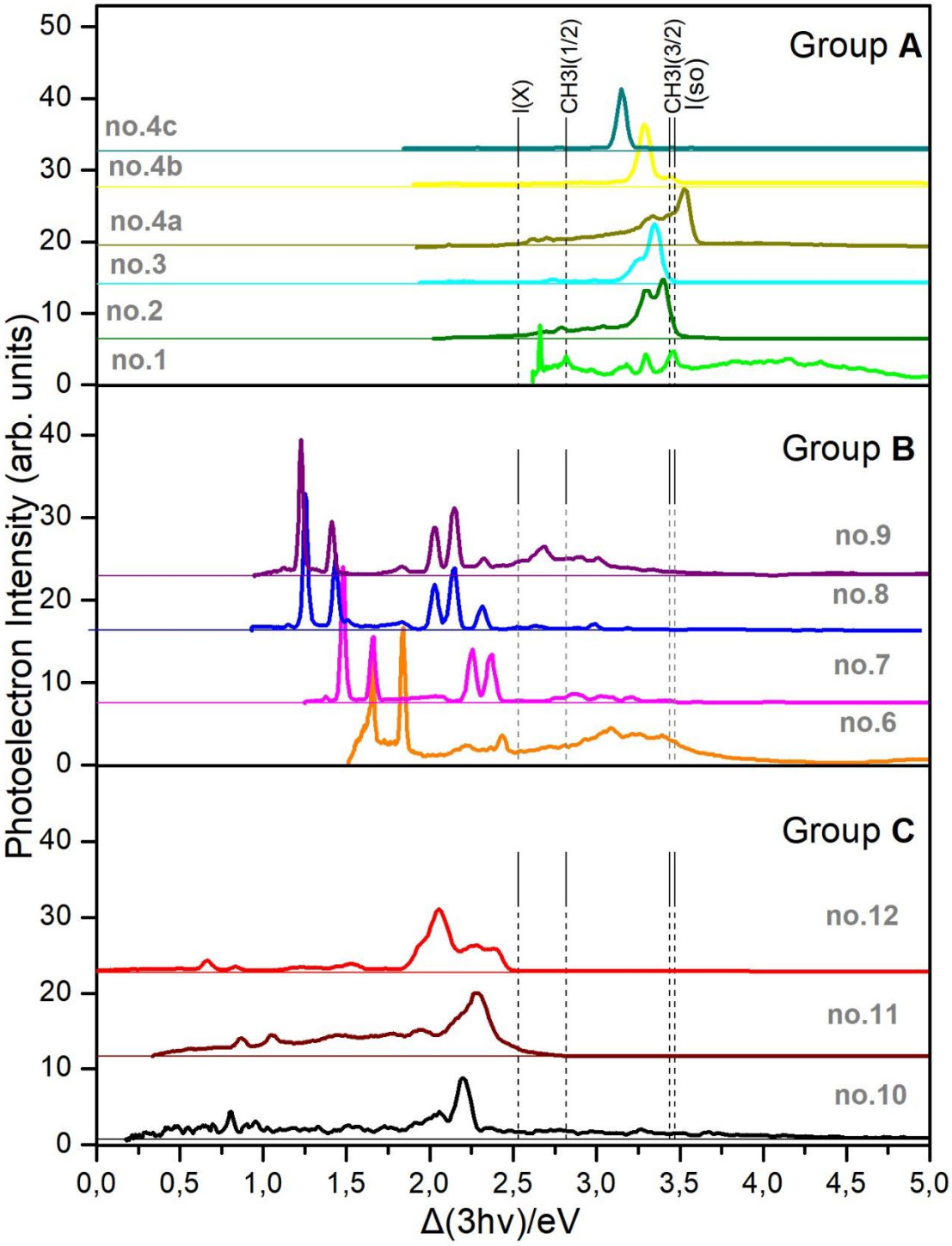

Figure 3.3 : Photoelectron KER distributions for the Rydberg states belonging to Groups A, B and C on a relative energy scale for 3hv ionization processes. The maximum kinetic energy thresholds for the creation of relevant I and CH_3I ions are indicated by vertical lines.

Group A includes the states from #2 to #4a-c which lie on the lower energy part of the region under study between 58927 and 59898 cm^{-1}. We have separated excitation no.4 into three subexcitations labelled as 4a, 4b and 4c, respectively. According to Eden *et al.*, only 4b is considered to be a molecular Rydberg state of CH_3I but since we observed resonant signals, states 4a and 4c are included for a more complete picture of the dynamics in the region.

Photodissociation followed upon excitation to Group A states results in excited I** in quantum states spanning the energy region between 56000 to 67000 cm^{-1}, according to the PE spectra ((See **Figure 3.2**). The strongest photoelectron signals are observed in states around 66000 cm^{-1}, denoted as I (66). As one can see from the PE spectra, I or I* are absent or negligible compared to the amount of the other I channels produced. Similarly, no peaks corresponding to CH_3 ground state or excited states are discernible from the PE distributions, although photoelectrons from their ionization are well within the energy range detected. Therefore straightforward information about the CH_3 states involved cannot be extracted from the PE spectra. However, it is clear that there is a propensity for available energy to be channeled into iodine atoms instead of the CH_3 radicals after the bond rupture.

Within the group, going from no.2 towards no.4 we observe more excited iodine being produced as the energy increases. The trend does not continue towards 4a-c. Signals of I** in the higher energy regions become harder to resolve since the iodine atomic levels get denser (see *Table 3-2*). An alternative assignment for features of excitations no. 2 to 4 is that of CH_3I^+ vibrational levels (see Figure 3.3). Indeed, broader features in excitations no.2 and no.3 can be assigned either to I(64) and I(66) (**Figure 3.2**) or to stretching vibrations ((~ 2000 cm^{-1}) of the ion CH_3I^+ ($^2E_{3/2}$) (Figure 3.3). In a similar manner, in excitation no. 4a small peaks around 1.5 eV ((1hv scale) or 2.8 eV (3hv scale) could be I(54) to I(61) or vibrations (~ 800 cm^{-1}) of the ion CH_3I^+ ($^2E_{1/2}$) as in no.4c where there is competing assignment between I(56) and I(61) and CH_3I^+ ($^2E_{1/2}$). In light of what we observe at higher excitation energies, where CH_3I^+ photoelectrons generate broader distributions rather that sharp peaks, we believe that the excited I assignment is more likely, but the reader should keep in mind this CH_3I^+ possibility.

In group B's (excitations no.6 to no.9) photoelectron KERs (See Figure 3.3), it is clear that low KER photoelectron peaks match well the ionization of I (54) and I (56) excited states. Even though, the energy given to the system compared to Group A is higher, it seems that less energetic iodine is produced, covering every atomic state from 54000 to 63000 cm^{-1}. Stronger signals are displayed for I (54) and I(56) with I(60) and I(61) states following .Within the group, the same iodine states are produced with little variation in the relative intensities.

Faster photoelectrons are also observed at ΔKER(1hv)>1.8 eV as a broad distribution of lower intensity rather than distinct sharp peaks. We assign these to ground state and vibrationally excited v_2 (umbrella mode) CH_3I^+ ($^2E_{3/2}$) rather than more excited I** that also could fit energetically, as seen in Figure 3.3. The argument is further confirmed by the lack of these photoelectrons in peak #8 which converges to CH_3I^+ ($^2E_{1/2}$) instead of CH_3I^+ ($^2E_{3/2}$).

It is interesting that the excitation no.1 (of group A) displays features more similar to those of Group B than Group A. The I** states of I (60), I(61) and I(63) seem to be present along with a broad high KER feature that could be assigned to vibrationally excited CH_3I^+ vibrationally excited in a mode with vibrational frequency equal to 1613 ± 806 cm^{-1}, possibly the v_2 umbrella mode.

Group C consists of the higher energetic Rydberg states of the range under study, excitations no.10 to no. 12. As seen in Figure 3.3 the peaks are not very consistent with CH_3I^+ generation unless this is combined with substantial rovibrational excitation. Photoelectron peaks here resemble those of group A in KER which suggests that increase in excitation energy, does not lead to more energetic iodine (>68000cm^{-1}). The peaks are wider, which can be attributed to populating more atomic I states in the 64000 to 68000 cm^{-1} region. In fact, we observe highly excited I all over the range from 64000 to 68000 cm^{-1} in different ratios and small production of I(54) and I(56) (See **Figure 3.2 : Photoelectron KER distributions for the Rydberg states belonging to Groups A, B and C on a relative energy scale for 1hv ionization processes. The maximum kinetic energy thresholds for the creation of relevant I and CH3 ions are indicated by vertical lines.**Figure 3.2).

To summarize, PE distributions suggest the production of highly excited iodine in various quantum states after excitation to any chosen state of the CH_3I Rydberg series.

Given the fact that a variety of Rydberg states, converging to either $CH_3I^+(^2E_{3/2})$ or $CH_3I^+(^2E_{1/2})$, were selected as intermediate steps, the preferential I excitation does not seem to be a Rydberg-feature-dependent effect, but it characterizes the dynamics in the whole 55000 to 70000 cm^{-1} excitation region. This highlights a preference of the CH_3I system to partition energy in the iodine atom as the C-I bond breaks. The lowest excitations (Group A) produce I** mostly in states close to 66000cm^{-1}, while the highest excitations (Group C), exhibit a wider I** state distribution spanning from 54000 to 68000 cm^{-1}. In between, Group B excitations display intense peaks for I (54) and I(56) along with vibrationally excited CH_3I^+(3/2).

3.3.2 Ion Kinetic Energy Release Distributions

CH_3^+ slice images were recorded following the excitation to selected molecular Rydberg states converging to both ground ionic state $X(^2E_{3/2})$ and spin-orbit excited state $X(^2E_{1/2})$ in the two-photon excitation region between 54600 to 69783 cm^{-1} (see Table 3-1). Images of iodine and methyl ions for all excitations studied are shown in Appendix C.

The corresponding kinetic energy release distributions were extracted from the images. Similar to PE analysis, an energy shift relative to the photodissociation of CH_3I taking place at 69783 cm^{-1} (excitation no. 12) is introduced to account for the change in photolysis wavelength in each KER. Given that the excitation step is a two-photon process, we tested for processes of one, two or more photons in order to interpret the energy distributions. Processes with a total of 3 or 4 total number of photons agreed with the primary observations in the KERs, consequently the energy shift shown is for a total of 3hv or 4hv processes. The corresponding maximum kinetic energy thresholds for several channels are indicated by vertical lines at each figure.

All CH_3^+ KERS of Group A (See Figure 3.4**Error! Reference source not found.**) display a broad kinetic energy distribution spreading in a range from 0-2 eV of translational energy. For excitations no.2 and no.3, in agreement with the PE spectra, one could propose the following photodissociation steps:

$CH_3I + 2hv \rightarrow CH_3I^{**}(Ryd)$ (5a)

$CH_3I^{**}(Ryd) + 1hv \rightarrow CH_3I^{\#}$ (5b)

$CH_3I^{\#} \rightarrow CH_3(X) + I^{**}$ (5c)

CH_3I molecules are resonantly excited with 2 photons to the selected Rydberg state CH_3I^{**}(Ryd). Then the CH_3I in the Rydberg state absorbs one additional photon producing superexcited CH_3I (henceforth denoted $CH_3I^{\#}$). $CH_3I^{\#}$ subsequently dissociates to CH_3(X) + I**.

CH_3^+ KERs for Rydberg transitions no.2 and no.3 display two broad shoulder-like peaks (see Figure 3.4) that correspond to dissociation channels leading to CH_3(X) along with I(64) and I(66), respectively. Kinetic energy distribution of CH_3^+ for transition 4a suggests that it follows the same dynamics as transitions no.2 and no. 3. However, spectra from excitations 4b and 4c display features resembling a vibrational progression. These could be assigned to channels producing vibrationally excited $CH_3(X,v_1=0\text{-}5)$ potentiantly in the stretch mode and a more limited range of I** states.

Overall, group A excitation leads to the production of I** in several excited quantum states with I (64), I (65), I (66) being more pronounced:

$$CH_3I + 2hv \rightarrow CH_3I^{**}(Ryd)\ (6a)$$
$$CH_3I^{**} + 1hv \rightarrow CH_3I^{\#}\ (6b)$$
$$CH_3I^{\#} \rightarrow CH_3(X,v) + I(64), I(65), I(66)\ \ (6c)$$

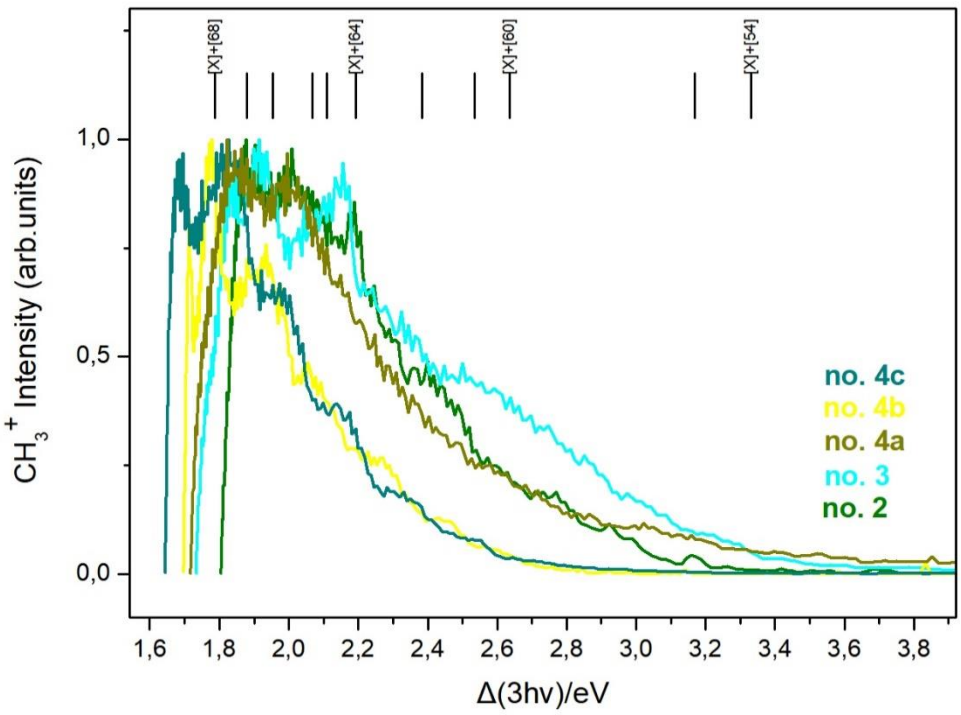

Figure 3.4: CH_3^+ KER distributions for the Rydberg states belonging to Group A ((2, 3,4a-c) on a relative energy scale for the total of 3hv excitation processes. The maximum kinetic energy thresholds for the creation of $CH_3(X)$ + I are indicated by vertical lines. Notation: [X]→ $CH_3(X)$, [54] → I(64).**

I^+ ion slice images/KERs for excitation transitions no.2 and no.3 confirm the channel assignments for CH_3^+ and do not display any additional features. However, I^+ KERs for 4a and 4c display an intense peak that could be assigned to the non-resonant channels (Fig.5 bottom):

$$CH_3I + 2hv \rightarrow CH_3(X) + I/I^* \ (7)$$

Analysis of the same peak in the 3-hv scale (Figure 3.5, top) does not energetically match any channel very well, unless one assumes that the third photon energy is channeled into internal degrees of freedom of the photofragments.

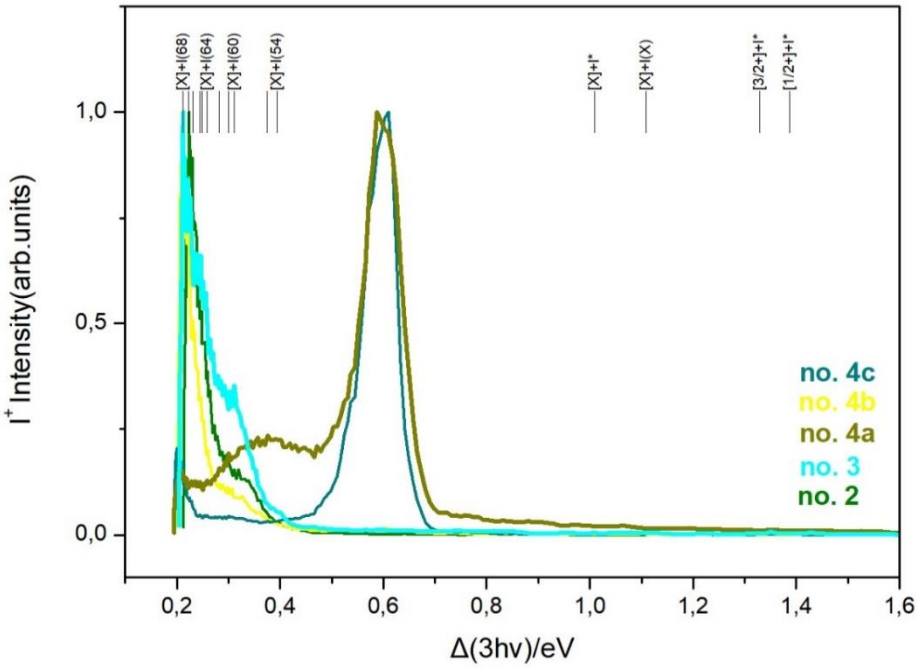

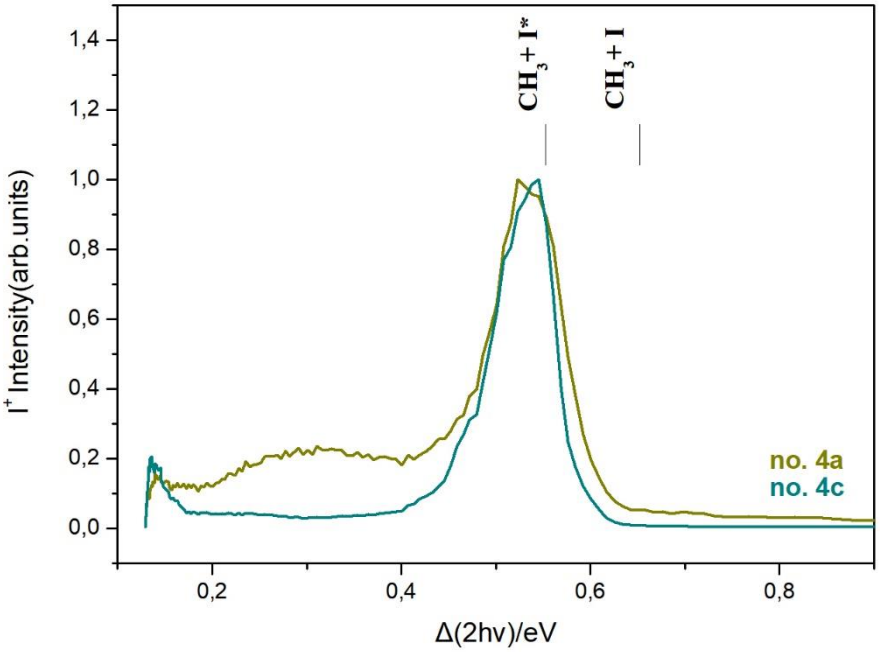

Figure 3.5 : I^+ KER distributions for the Rydberg states belonging to Group A ((2, 3,4a-c) on a relative energy scale for the total of 3hv (up) and 2hv (down) excitation processes. The maximum kinetic energy thresholds for the creation of $CH_3(X)$ + I is indicated by vertical lines. [X]→ $CH_3(X)$, [54] →I(64),[3/2+]→CH_3 from $CH_3I^+(^2E_{3/2})$.**

Group B CH_3^+ KERs (Figure 3.6), extracted from slice images of the product CH_3 ions, exhibit the broadest kinetic energy distributions of our analysis covering a range

of approximately 3 eV of kinetic energy. As in group A, CH_3I molecules are resonantly excited with 2 photons to the selected Rydberg state and then after absorbing one additional photon superexcited $CH_3I^{\#}$ is produced. However, $CH_3I^{\#}$ dissociates to CH_3(X,v) + I**(54,56) and CH_3(X,v) + I**(60,61,63), producing a different set of I** states than Group A along with ground state or vibrationally excited CH_3. These two different groups of channels can be assigned to the two shoulder-like maxima of the KER. In the higher excitations (no.8 and no.9) another type of channel is becoming accessible in which CH_3 appears in its first excited state ((3s $^2A_1$') along with I(54) and I(56) at a Δ(4hv)<2eV. Thus, group B excitation namely leads to the production of I** in many quantum states with a preference towards I (54) and I(56).

$Group\ B\ (6-9)$:

$CH_3I + 2hv \rightarrow CH_3I(Ryd)\ (8a)$

$CH_3I\ (Ryd) + 1hv \rightarrow CH_3I^{\#}$ *(8b)*

$CH_3I^{\#} \rightarrow CH_3(X,v) + I(54), I(56)\ \ (8c)\ and$

$CH_3I^{\#} \rightarrow CH_3(X,v) + I(60), I(61), I(63)$ *(8d)*

$Group\ B\ (8,9)$:

$CH_3I + 2hv \rightarrow CH_3I(Ryd)\ (9a)$

$CH_3I(Ryd) + 2hv \rightarrow \rightarrow CH_3(3s\ 1A_1, v) +\ I(54), I(56)\ \ (9b)$

Vibrational spacing of CH_3(X) and the spacing between the iodine atomic levels being at the same order of magnitude ((around 1500 cm^{-1}) provides additional complexity to the assignments. This is why the PE spectra proved to be very critical suggesting that I** states are produced rather than vibrationally excited CH_3.

The sharp peak around 2.5 eV only appearing at KER no.9 can be assigned to 1hv photodissociation through the A-band.

$$CH_3I + 1hv\ \rightarrow CH_3(X) +\ I(X)/I^*\ \ (10)$$

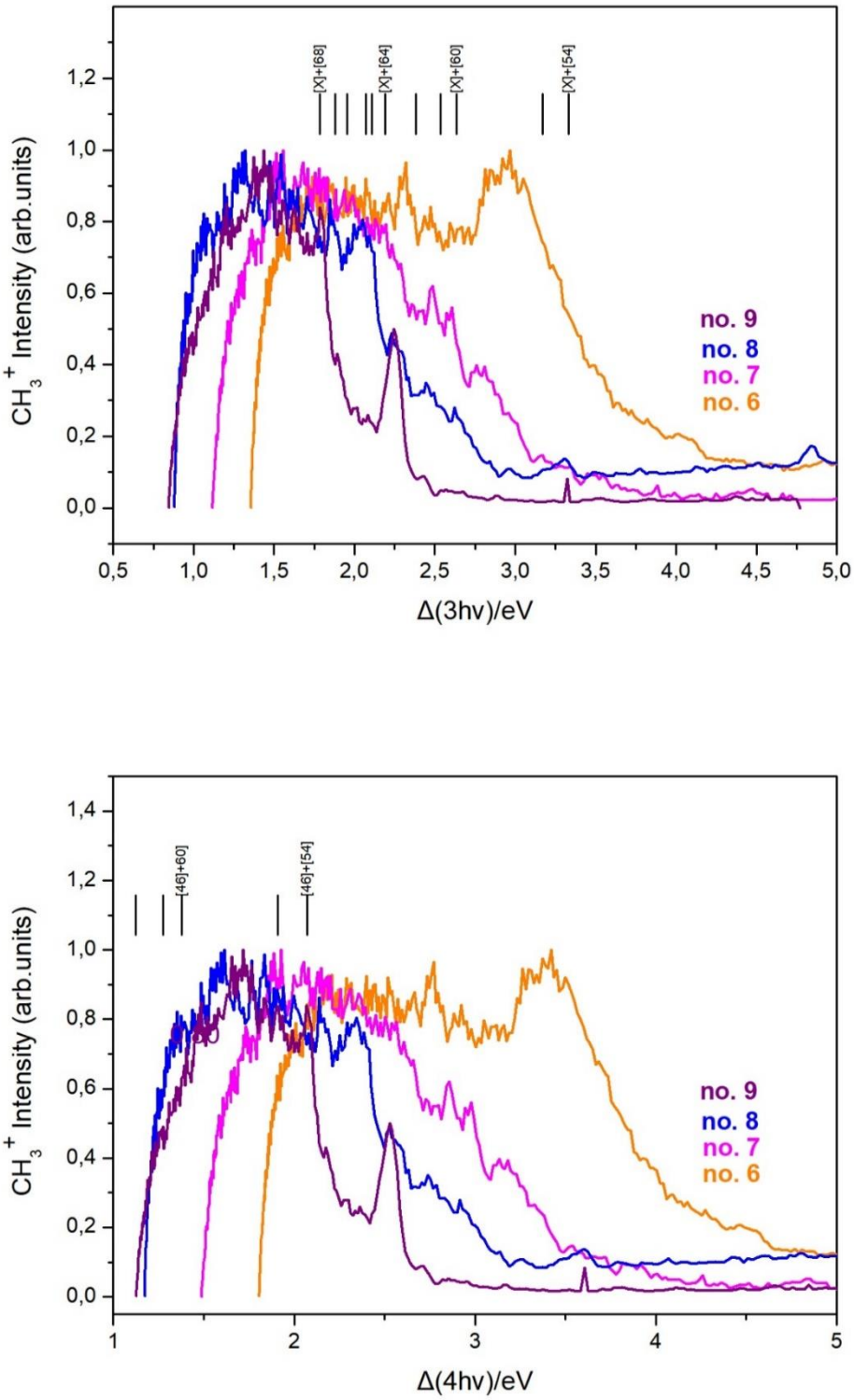

Figure 3.6: CH_3+ KER distributions for the Rydberg states belonging to Group B ((6,7,8,9) on a relative energy scale for the total of 3hv (up) and 4hv (down) excitation processes. The maximum kinetic energy thresholds for the creation of CH_3(X) + I are indicated by vertical lines.**

Group B I^+ ion KERs (Figure 3.7) are consistent with the observations of CH_3^+ and PE distributions. Low KER I^+ is assigned to highly excited I** states, while higher KER

I^+ is consistent with CH_3I^+ dissociation (see PE spectra). $CH_3I^+(^2E_{3/2})$ is formed by a total of 3hv process resulting to :

$$CH_3I + 4hv \rightarrow CH_3\,(X) + I/I^* \quad (11)$$

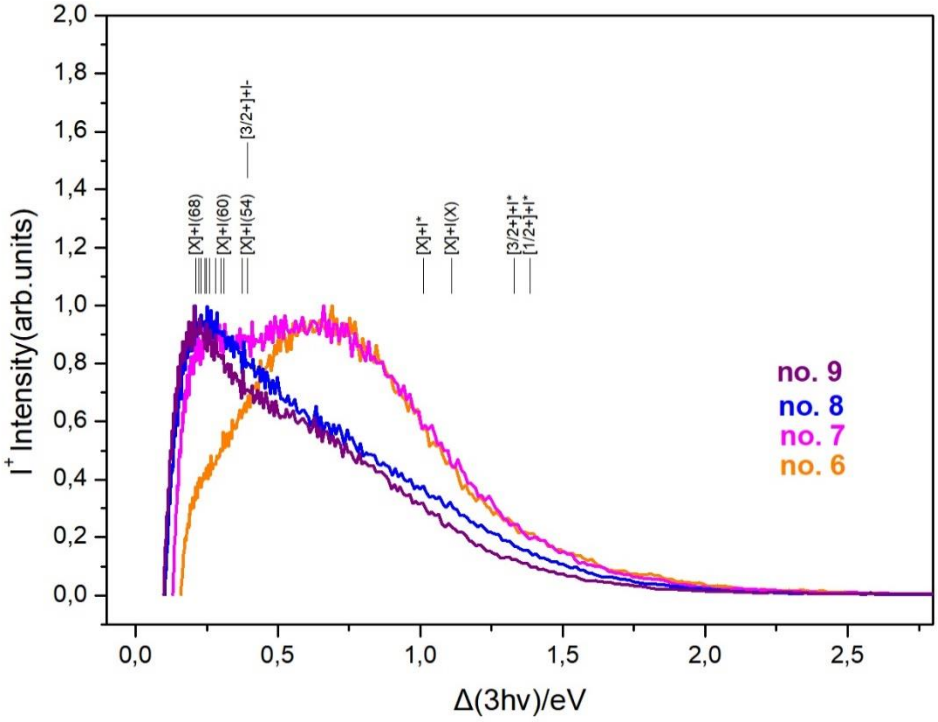

Figure 3.7:I^+ KER for group B (transitions 6-9), showm shifted at 3hv energy

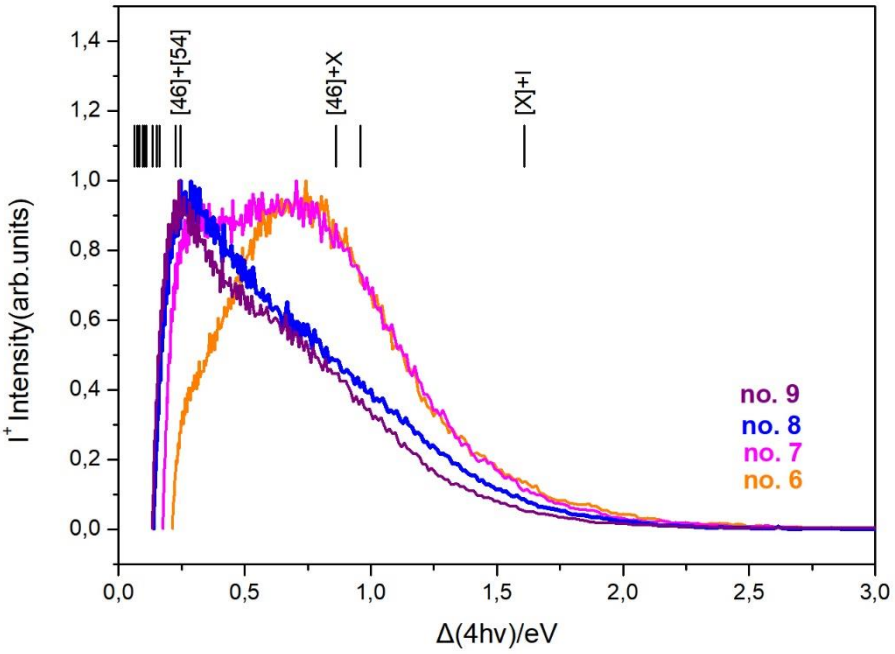

Group C I^+ KERs (excitations no.10 and no. 11), obtained from slice images of I^+, consist of a broad structureless distributions which can be attributed to the same channels as the previous groups (Figure 3.8).

$Group\ C$ (10,11):

$CH_3I + 2hv \rightarrow CH_3I(Ryd)$ (12a)

$CH_3I(Ryd) + 1hv \rightarrow CH_3I^{\#}$ (12b)

$CH_3I^{\#} \rightarrow CH_3(X,v) + I(54),..,I(67)$ $(12c)$

Peak no.10 displays an additional intense band which can be attributed to dissociation of the parent ion via 1 photon.

$CH_3I + 1hv \rightarrow CH_3\ (X) + I$ (13)

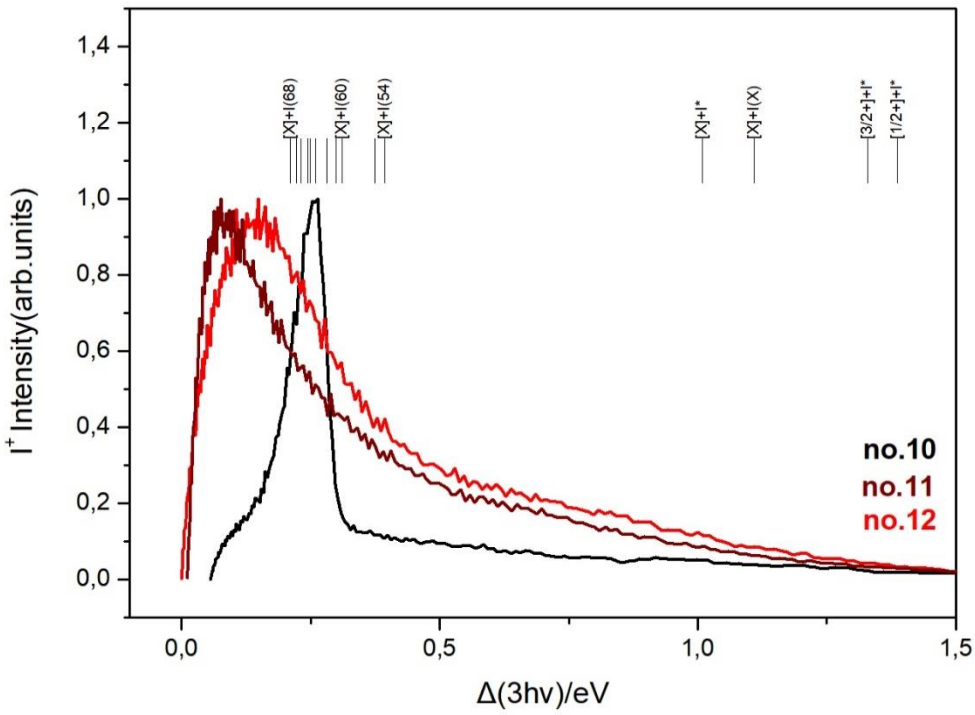

Figure 3.8: I^+ KER distributions for the Rydberg states belonging to Group C ((10,11,12) on a relative energy scale for the total of 3hv excitation processes. The maximum kinetic energy thresholds for the creation of $CH_3(X)$ + I are indicated by vertical lines.**

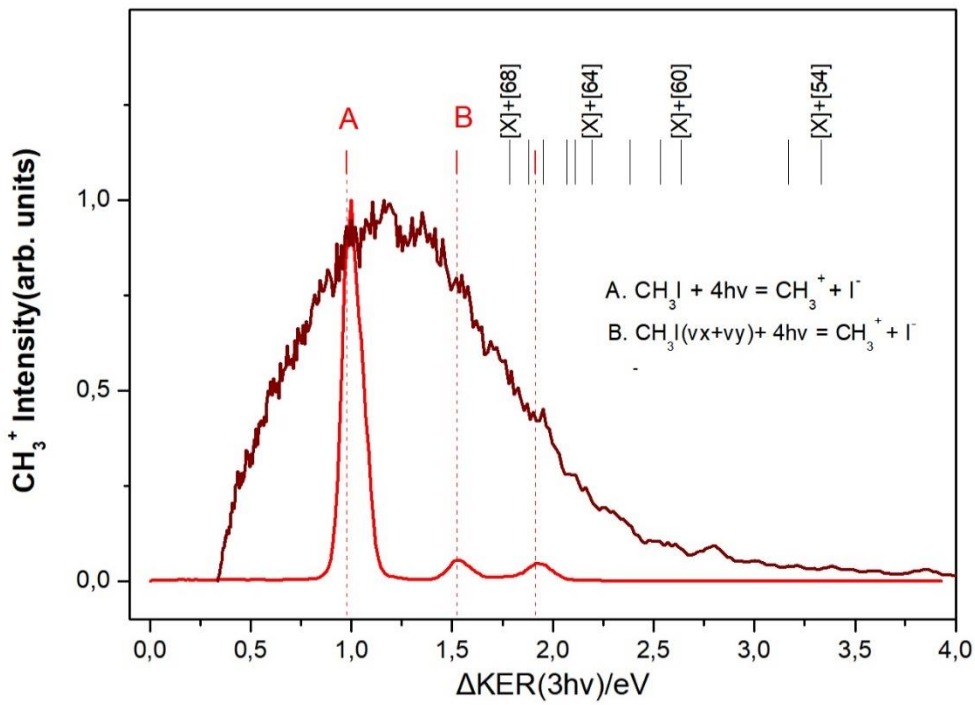

Figure 3.9: CH_3^+ KER distributions for the Rydberg states belonging to excitations no.11 and no.12. The maximum kinetic energy thresholds for the potential channels are indicated by vertical lines.

The methyl signal for excitation no.10 was negligible. The CH_3^+ distribution for no.11 matches the I assignments (Figure 3.9).

Even though, group C states seem to follow similar dynamics judging solely from the iodine and photoelectron images, the CH_3 image/KER of peak no.12 displays, in contrast with KER from no.11, three distinct sharp rings/peaks. Given the similarity of the rest of the KERs, one could assign these peaks to CH_3^+ and I^- produced from CH_3I forming an ion-pair. Negative iodine ions were not observed, so we suggest that I^- rapidly converts to I(54). The electron ejected has similar KER with the electron ejected from I(54) ionization(0.61 vs 0.65 eV). Specifically, the slower peak (A in Figure) can be assigned to CH_3 ion produced from the following process:

$$CH_3I + 4hv \rightarrow CH_3^+I^- \ (14a)$$

$$CH_3^+I^- \rightarrow CH_3^+ + I^- \ (14b)$$

$$I^- \rightarrow I(54) + e^- \ (14c)$$

The two faster peaks can be assigned to CH_3^+ produced from 'hot' vibrationally excited CH_3I in a combination vibrational mode denoted as $v_x + v_y$ at 3500 cm^{-1}. Two possible combinations could be $v_1 + v_2$ ((CH-stretch and umbrella mode) or $v_1 + v_3$ ((CH-stretch and C-I stretch modes).[22]

$$CH_3I\left(v_x + v_y = 3500cm^{-1}\right) + 4hv \rightarrow CH_3^+ + I^- \ (15)$$

$$I^- \rightarrow I(54) + e^- \ (12)$$

3.3.3 Angular Distributions

Anisotropy parameters were extracted from angular distribution analysis of the ion raw images. Even though the photodissociation mechanisms proposed here involve multiple steps, the distributions of the polarized photofragments were fitted with the simplified expression for a single step photodissociation process thus resulting in beta parameters that are an average of the processes involved. The expression consists of the even expansion of Legendre polynomials, [23]as discussed in Chapter 1:

$$I(\theta) = A[\,1 + \beta_2 P_2 \cos\theta] \quad (16)$$

where P_2 is the 2nd order Legendre polynomial and β_2 the spatial anisotropy parameter.

In this way, underlying trends in the nature of the transitions (parallel or perpendicular) involved can be identified. The calculated β_2 values for the methyl and iodine ions are presented in Figure 3.6 as a function of the total translational energy in a relative 3hv shift to account for the change in the excitation wavelength, as in the previous sections. Overall, we observe mostly positive β_2 values ranging from 0 to 2, with the majority of them lying between 0 and 1 for both ions. Positive values, close to the +2 (value for a pure parallel transition), suggest that the processes dominating the dynamics are mostly parallel but some mixing of transitions with perpendicular character occurs. The values vary for different excitations, therefore there is some dependence on the first step of the photodissociation process.

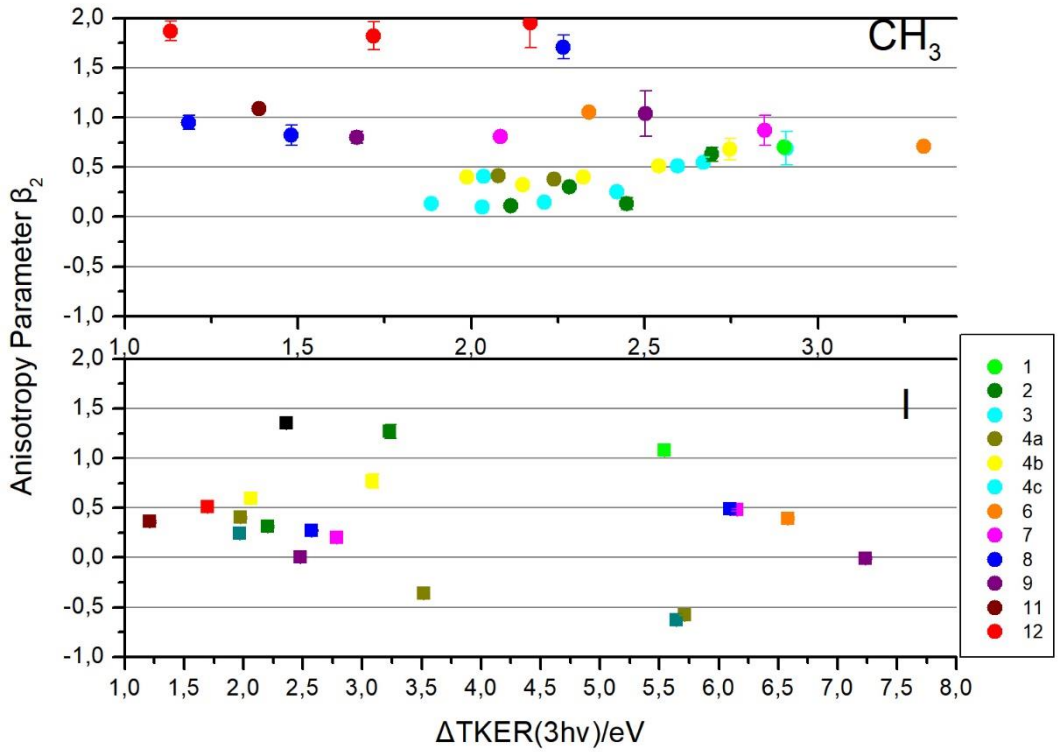

Figure 3.10: Spatial anisotropy parameter β_2 values for CH_3 (up-circles) and I((down-squares) for the different excitations (1-12) as a function of the total translational energy with a 3hv shift.

The β_2 values of the CH_3 ion raw images of Group A(2,3,4a-c) vary between 0 and 0.75 displaying isotropic surface patterns. There is a slight increase of the values, suggesting more parallel character, towards the channels producing faster CH_3 (less excited I) (Figure 3.10 up or Figure 3.11).

However, transitions with perpendicular character dominate the fast iodine sharp peaks observed for states 4a and 4c (dark yellow and dark cyan points in Figure 10) where we have β_2 parameters with negative values around 0.6 with ΔTKER around 5.65 eV. This suggests the involvement of a perpendicular channel in I^+ generation that is compensated by parallel channels in the course of its CH_3^+ counter fragment production.

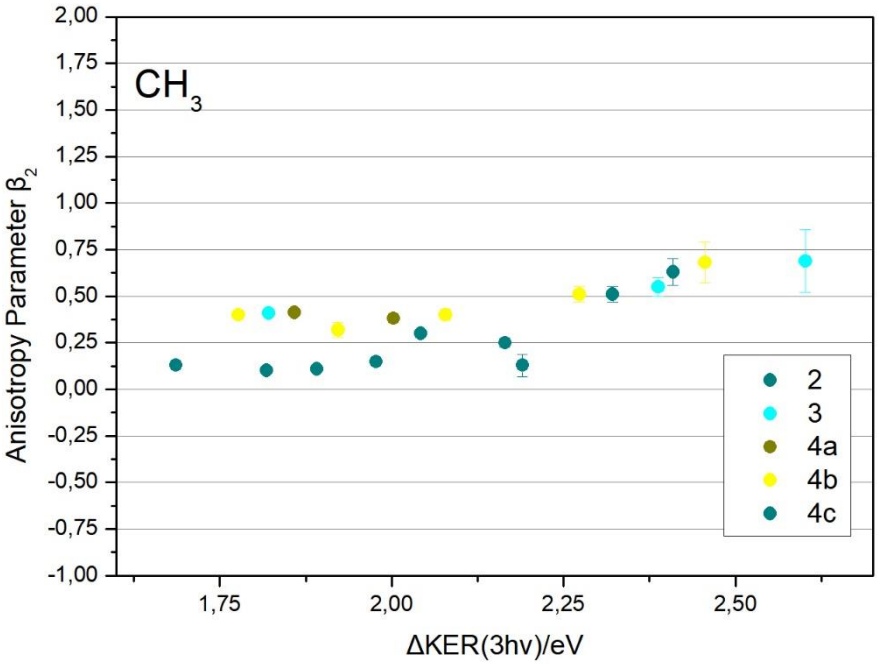

Figure 3.11 Spatial anisotropy parameter β_2 values for CH_3 for the excitations 3 and 4a, b, c as a function of the Kinetic Energy Release with a 3hv shift.

The β_2 values of the iodine ion raw images of Group B extracted for the transitions involved in excitations no.6 to no.9 are very close to isotropic (0.3) for the whole energy range. Values from the CH_3 corresponding to the slow iodine regions is similar for all the excitations around 0.75 to 1.75. The sharp peak only present in #9 CH_3 dis-

tribution has the total isotropic value of zero ((See Figure 3.9**Error! Reference source not found.**) .

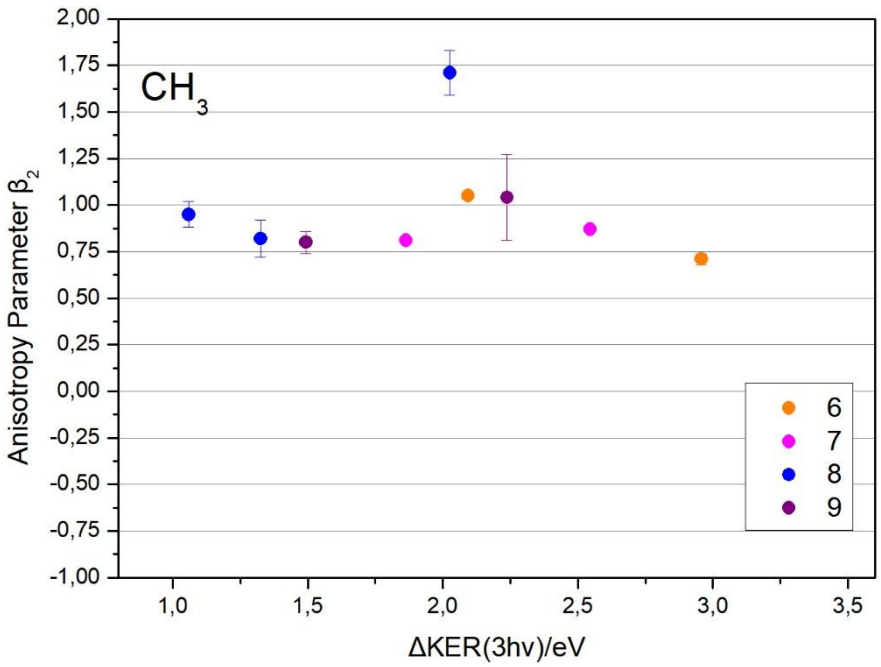

Figure 3.12 Spatial anisotropy parameter β_2 values for CH_3 for the excitations 6 to 9 as a function of the Kinetic Energy Release with a 3hv shift.

For excitations 10-12, Group C, for total kinetic energy release < 1.7 eV the β_2 values for I are similar to the other groups (around 0.4). For higher energies, there is an increase and the values reaching values around +1.5 for each excitation and for both of the ions . Finally, the three sharp distinct peaks for #12 describe pure parallel transitions with β_2 values very close to +2(Figure 3.9**Error! Reference source not found.**).

3.4 Discussion

As described in the previous section, we observe the production of highly excited iodine in various quantum states from the photodissociation of CH_3I. This discovery implies that there is a completely different dynamical picture in higher energies than the one extensively explored for photolysis upon excitations in the A, B and low lying 3s Rydberg state region. In lower excitation energies (see Introduction), the photon excess energy is not partitioned to the iodine atom but preferentially to vibrational

degrees of freedom of the CH_3 fragment, limiting the iodine produced solely to ground and spin-orbit excited quantum states.

Production of highly excited iodine (or any halogen) as the one observed here is not a common outcome in methyl halide photolysis. In fact, a preliminary literature search showed that no other methyl or hydrogen halides exhibit such behavior. Energetically, one would expect photodissociation (exit) channels involving electronically excited halogen or electronically excited methyl photofragments or both to manifest themselves at sufficiently high excitation energies. The photon energies employed here allow such channels, but only those with iodine excitation are observed. This suggests that electron excitation in CH_3I is mainly concentrated on the I atom or that there are significant barriers in channels involving electronically excited CH_3 production. However, as excitation energy increases moving from Group A to Group B states, we observe the production of less excited I with iodine excitation region shifted from 60000 cm^{-1} to 54000 cm^{-1}(See Figure 3.2). This observation could imply that at the energy window spanning Group B's excitations energy is also focused to the CH_3 fragments . Theoretical calculations could shed light into this problem.

Comparing CH_3I results with CH_3Br results[24] (see Chapter 2), where CH_3 photofragment is the one that is electronically (and rovibrationally) excited, while Br remains in its ground electronic or spin-orbit excited state, is an interesting deviation from the rule that elements in a group of the periodic table exhibit similar behavior. Here it seems that going from Br to I in CH_3-X switches CH_3 excitation off and X excitation on. One explanation could be that the larger and more polarizable iodine atom is more likely than CH_3 to "store" the high excess energy in CH_3I photolysis, while the smaller and less polarizable Br atom does not provide much more stabilization than CH_3, therefore the excess energy there ends up in the methyl fragment. If this idea is correct, we expect that in CH_3Cl and CH_3F photolysis at high energies the dynamics will resemble that of CH_3Br. One could suggest that electronically excited CH_3 was not observed here due to fragmentation into CH_2^+, CH^+ and C^+. Indeed, in a similar study[24] for CH_3Br (see Chapter 2), we observed various CH_3 fragments like CH_2, CH, C.. etc. in comparable signals with CH_3. However, such signals were not observed in the TOF spectrum in the current study.

Generation of multiple excited states of I originating from a single Rydberg state of CH_3I provides some insight into the dynamics involved. If further excitation of the Rydberg state to a single "superexcited" $CH_3I^{\#}$ state involved only one exit channel, then a single quantum state of I** would be produced. However, what we observe is production of several I** states at one excitation energy and the production of the same I** state (for example I (54) or I (56)) at different excitation energies, i.e. through different Rydberg state origins. In lack of theoretical data in the region, we can conclude that following excitation to the designated Rydberg state, CH_3I absorbs a photon and ends up in one or more $CH_3I^{\#}$ state(s) coupling (directly or through curve crossing to repulsive states) to the exit channels observed. The different beta parameters measured for Br^+ and CH_3^+ suggest that these crossings are closer to the excitation region rather than the exit region of the PES and are the cause of the nearly isotropic angular distributions observed in most excitation energies.

In the Rydberg region, after two-photon-resonant excitation to specific states we observe no fragmentation that would be an indication of a predissociation mechanism. Instead, in most cases, CH_3I absorbs at least one more photon forming highly excited metastable $CH_3I^{\#}$ before it dissociates. This implies that the Rydberg states do not cross with any repulsive states. That said, it is worth to note that for transitions no.4a and no.4c we do observe 2hv photolysis of CH_3I (see figure) but these transitions are not part of the Rydberg series, as far as we know. In few excitations, mostly in higher energies (Group B and Group C), the parent ion is formed instead of the superexcited species.

From a practical point of view, CH_3I photolysis with the scheme used in this work could be used as a source for photolytic production of electronically excited iodine. A rough control over which iodine states will be produced can be implemented by choosing different excitation transitions. This can be easily seen from the PES spectra of the different excitation groups denoted as A, B, C where a different range of states is preferentially produced in each group and excitation energy. A second practical conclusion of this work seems to be that iodine could be used as a "lightning rod" in molecular excitation "absorbing" the excess energy and protecting sensitive chemical moieties. Of course much work is needed in other systems to confirm that this could be the case.

3.5 References

[1] Moore, R. and Groszko, W. (1999). Methyl iodide distribution in the ocean and fluxes to the atmosphere. *Journal of Geophysical Research: Oceans*, 104(C5), pp.11163-11171.

[2] . Saiz-Lopez, A., Plane, J., Baker, A., Carpenter, L., von Glasow, R., Gómez Martín, J., McFiggans, G. and Saunders, R. (2011). Atmospheric Chemistry of Iodine. *Chemical Reviews*, 112(3), pp.1773-1804.

[3] McFiggans, G., Plane, J., Allan, B., Carpenter, L., Coe, H. and O'Dowd, C. (2000). A modeling study of iodine chemistry in the marine boundary layer. *Journal of Geophysical Research: Atmospheres*, 105(D11), pp.14371-14385.

[4] O'Dowd, C., Jimenez, J., Bahreini, R., Flagan, R., Seinfeld, J., Hämeri, K., Pirjola, L., Kulmala, M., Jennings, S. and Hoffmann, T. (2002). Erratum: Marine aerosol formation from biogenic iodine emissions. *Nature*, 417(6889), pp.632-636.

[5] Chameides W, Davis D. Iodine: Its possible role in tropospheric photochemistry. *Journal of Geophysical Research* : Oceans. 1980.

[6] Davis, D., Crawford, J., Liu, S., McKeen, S., Bandy, A., Thornton, D., Rowland, F. and Blake, D. (1996). Potential impact of iodine on tropospheric levels of ozone and other critical oxidants. *Journal of Geophysical Research: Atmospheres*, 101(D1), pp.2135-2147.

[7] Aschmann, J., Sinnhuber, B., Atlas, E. and Schauffler, S. (2009). Modeling the transport of very short-lived substances into the tropical upper troposphere and lower stratosphere. *Atmospheric Chemistry and Physics*, 9(23), pp.9237-9247.

[8] Tegtmeier, S., Krüger, K., Quack, B., Atlas, E., Blake, D., Boenisch, H., Engel, A., Hepach, H., Hossaini, R., Navarro, M., Raimund, S., Sala, S., Shi, Q. and Ziska, F. (2013). The contribution of oceanic methyl iodide to stratospheric iodine. *Atmospheric Chemistry and Physics*, 13(23), pp.11869-11886.

[9] Montzka, S. A. and Reimann, S.: Ozone-depleting substances and related chemicals, in Scientific Assessment of Ozone Depletion: 2010, *Global Ozone Research and Monitoring Project – Report No. 52*, Geneva, Switzerland, 2011

[10] Tuite, K., Brockway, N., Colosimo, S., Grossmann, K., Tsai, C., Flynn, J., Alvarez, S., Erickson, M., Yarwood, G., Nopmongcol, U. and Stutz, J. (2018). Iodine catalyzed ozone destruction at the Texas coast and Gulf of Mexico. *Geophysical Research Letters*.

[11] R. E. Huffman, The Formation of Ions in Upper Atmosphere, GRD Research Notes No.66 AFCRL 851, AD 273999, 1961.

[12] Eppink, A.; Parker, D. Energy Partitioning Following Photodissociation Of Methyl Iodide In The A Band: A Velocity Mapping Study. *The Journal of Chemical Physics* 1999, 110, 832-844.

[13] Xu, H.; Pratt, S. A New Look At The Photodissociation Of Methyl Iodide At 193 Nm. *The Journal of Chemical Physics* 2013, 139, 214310.

[14] Alekseyev, A.; Liebermann, H.; Buenker, R.; Yurchenko, S. An Ab Initio Study Of The CH3I Photodissociation. I. Potential Energy Surfaces. *The Journal of Chemical Physics* 2007, 126, 234102.

15 Alekseyev, A.; Liebermann, H.; Buenker, R. An Ab Initio Study Of The CH3I Photodissociation. II. Transition Moments And Vibrational State Control Of The I* Quantum Yields. *The Journal of Chemical Physics* 2007, 126, 234103.

16 Gsitzinger, G., Corrales, M., Loriot, V., de Nalda, R. and Bañares, L. (2012). A femtosecond velocity map imaging study on B-band predissociation in CH3I. II. The 201 and 301 vibronic levels. *The Journal of Chemical Physics*, 136(7), p.074303.

[17] Gardiner, S.; Lipciuc, M.; Karsili, T.; Ashfold, M.; Vallance, C. Dynamics Of The A-Band Ultraviolet Photodissociation Of Methyl Iodide And Ethyl Iodide Via Velocity-Map Imaging With 'Universal' Detection. *Physical Chemistry Chemical Physics* 2015, 17, pp.4096-4106.

18 Baronavski, A. and Owrutsky, J. Vibronic dependence of the B state lifetimes of CH_3I and CD_3I using femtosecond photoionization spectroscopy. *The Journal of Chemical Physics* 1998, 108(9), pp.3445-3452.

19 Dobber, M., Buma, W. and de Lange, C. Resonance enhanced multiphoton ionization photoelectron spectroscopy on nanosecond and picosecond time scales of Rydberg states of methyl iodide. *The Journal of Chemical Physics* 1999, 99(2), pp.836-853.

[20] Eden, S., Limão-Vieira, P., Hoffmann, S. and Mason, N.VUV spectroscopy of CH_3Cl and CH_3I. *Chemical Physics* 2007, 331(2-3), pp.232-244.

[21] Kramida, A., Ralchenko, Yu.,Reader, J. and NIST ASD Team (2018). *NIST Atomic Spectra Database* (version 5.5.6). Available: https://physics.nist.gov/asd [Fri Jul 27 2018]. National Institute of Standards and Technology, Gaithersburg, MD.

[22] Dobber, M.; Buma, W.; de Lange, C. Resonance Enhanced Multiphoton Ionization Photoelectron Spectroscopy On Nanosecond And Picosecond Time Scales Of Rydberg States Of Methyl Iodide. *The Journal of Chemical Physics* 1993, *99*, 836-853.
[23] Rakitzis, T.; Zare, R. Photofragment Angular Momentum Distributions In The Molecular Frame: Determination And Interpretation. *The Journal of Chemical Physics* 1999, *110*, 3341-3350.
[24] Hafliðason, A.; Glodic, P.; Koumarianou, G.; Samartzis, P.; Kvaran, Á. Multiphoton Rydberg And Valence Dynamics Of CH_3Br Probed By Mass Spectrometry And Slice Imaging. *Physical Chemistry Chemical Physics* 2018, *20*, 17423-17433.

4 Highly nuclear-spin-polarized deuterium atoms from the UV photodissociation of deuterium iodide.

4.1 Introduction

It has been shown that photodissociation of hydrogen halides with laser sources can produce highly polarized H atoms[1,2,3,4,5]. First, the photodissociation process polarizes the electron spin, up to 100% (for photofragment velocities parallel to the propagation direction of the circularly-polarized dissociation laser light).[6] Subsequently, due to the hyperfine interaction, the polarization oscillates back and forth between the electronic and the nuclear spin on the 1 ns timescale. By terminating this polarization exchange appropriately, for example by ionizing the atom, one can isolate the polarization in the electronic or nuclear spin.

This pulsed production of hyperpolarized H, is here extended to the production of hyperpolarized D atoms that can be used to study polarized D fusion reactions at high density, with much larger signals than conventional beam methods. The D atoms can be used to produce pulsed ion beams, allowing the possibility of measuring polarized fusion reaction cross sections over a large energy range. The pulsed production can also be combined with Inertial Confinement Fusion (ICF), where fusion is induced by an intense short laser pulse.[7] The photolysis and fusion pulses can be timed so that the D nuclei are maximally polarized when fusion occurs; such a combination can offer a straightforward method for measuring the effect of polarization in the D reactions, at densities close to 10^{18} cm^{-3}, and at collision energies of ~ 10 keV.

Theoretical calculations of the photofragment polarizations, over a range of UV photodissociation energies, have been performed for nearly all the hydrogen halides: HF/DF [8], HCl/DCl[9], HBr[10], and HI/DI[11]. At least two competing dissociation mechanisms occur: excitation to a dissociative state followed by adiabatic dissociation producing hydrogen atoms with spin-down electrons, or excitation to another dissociative state followed by adiabatic dissociation producing hydrogen atoms with spin-up electrons (also non adiabatic transitions between dissociative states can change the H at-

om polarization). Therefore, depending on the contribution from each mechanism, the hydrogen electronic spin polarization P_e can range from fully spin up (P_e=1) to fully spin-down ($P_e = -1$), and anything in between, including unpolarized (P_e=0). Calculations predict that P_e can take on values over this complete range, and depends strongly on the photolysis energy, on the halide cofragment (F, Cl, Br, or I), and the hydrogen isotope. For example, near maximal H polarizations (P_e = 1) are calculated at some energies for photodissociation of the hydrogen halides HCl, HBr, and HI (of which HCl and HBr have been measured at 193 nm[1,3]), and the deuterium halides DF and DI (which have not been measured previously). Here we determine the polarization of the D and I photofragments from the photodissociation of DI molecules at 270 nm, demonstrating a source of highly-polarized-high-density D atoms.

Nuclear-spin-polarized D atoms are important for the study of numerous nuclear reactions[12]. For example, controlling the nuclear spin polarization in fusion reactions offers important advantages, such as larger reaction cross sections, control over the emission direction of products, and in some cases suppressing unwanted neutron emission.[13,14] For the reactions D + T → n + ^{4}He and D + ^{3}He →p + ^{4}He, it is well known that the cross sections increase by ~50% when the nuclei have oriented nuclear spins.14,[15] However, the experimental inability to produce Spin-Polarized Deuterium (SPD) in sufficient quantity has not allowed the realization of polarized fusion in a plasma. This lack of SPD has left the three most important questions of polarized fusion unanswered:[14]

(1) Does the nuclear polarization survive the plasma long enough to benefit fusion? Theoretical calculations[16,17] indicate that it likely does, however, experimental demonstration is lacking (although proposals for such demonstration have been made recently[18,19]).

(2) What is the polarization dependence of the D-D fusion reaction? Over the last 30 years, several theoretical predictions, from 10 to 100 keV, range from enhancement, suppression, or no effect on reactivity[20,21,22,23,24,25], leaving a longstanding need for experimental resolution.

(3) Assuming (1) is positive, can sufficient SPD be produced for a nuclear reactor, ~10^{21} s^{-1} ?[3] For current methods, either the SPD production rate or polarization is too low. For example large-scale magnetic (Stern-Gerlach) separators are limited to pro-

duction rates of $\sim 10^{17}$ atoms s^{-1},3 and polarized solid deuterium targets are produced where densities reach ~3 x 10^{19}spins/ cm^3, but at a low polarization[26] of ~10% .

In this Chapter, we demonstrate the production of SPD from the photodissociation of deuterium iodide, which can offer sufficient SPD densities and production rates to help answer open questions (1-3). Magnetic separation methods require low beam densities to avoid collisions on the ms timescale of the separation process, which limits densities to 10^{12} cm^{-1} .3 In contrast, the DI photodissociation method requires only 1.6 ns (the D-atom hyperfine-beating time) to polarize the D nuclear spin, which is 10^6 times faster than magnetic separation, allowing densities larger by a similar factor, of order 10^{18} cm^{-3}. In addition, one photodissociating photon produces one SPD nucleus; industrial scale kW UV lasers can therefore achieve SPD production rates of at least 10^{21} s^{-1}. Below we discuss how SPD pulsed densities of 10^{18} cm^{-3} can be combined with pulsed laser fusion to study D-T, D-^{3}He, and D-D polarized reactions.

4.2 Experimental

The experiments are performed using a molecular beam set-up, to facilitate polarization sensitive detection. We measure the spin polarization of the iodine atoms via a Resonance-Enhanced Multiphoton Ionization (REMPI) scheme and infer the deuterium polarization by angular momentum conservation; past experiments of direct measurements of hydrogen spin polarization give excellent agreement with indirect detection.[19,5,27,28]

The experimental set-up has been explained in detail in Chapter 1 and elsewhere.[29,30] Briefly, deuterium iodide is mixed with He in a 50% ratio and expanded into the chamber via a pulsed nozzle. The molecular beam is intersected at right angles 50 mm downstream by the focused photolysis and probe laser beams. The resulting ion sphere is focused by a single ion lens on a gated position sensitive detector, thus performing velocity map imaging.[31]

4.3 Results

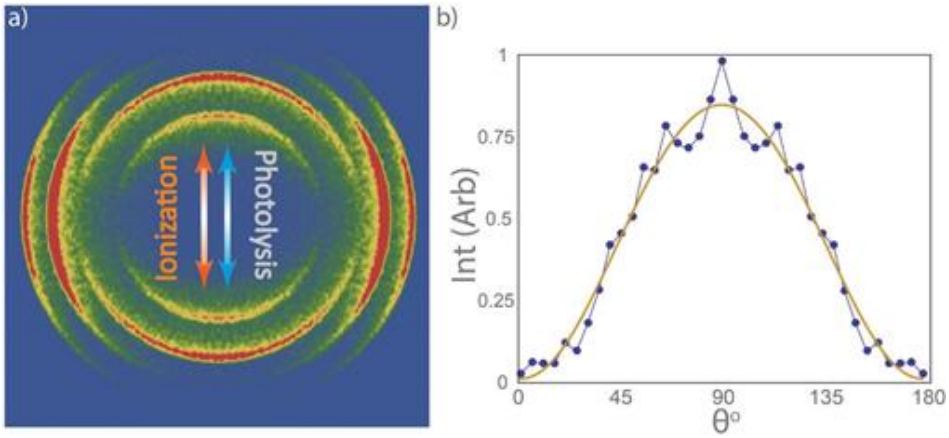

Figure 4.1 shows an image of the D ions produced by dissociation of DI at 270 nm and 243 nm in coincidence with I($^2P_{3/2}$) and I($^2P_{1/2}$) (henceforth denoted as I and I*, respectively). The D photofragments are ionized via 2+1 REMPI at 243 nm. From inner to outer, the four rings correspond to dissociation channels:

(1) DI + 270 nm → D + I* (v_D = 7242 m/s),

(2) DI + 243 nm → D + I* (v_D = 10184 m/s),

(3) DI+270 nm → D+I (v_D =12032 m/s), and

(4) DI + 243 nm → D+I (v_D = 13880 m/s),

where v_D is the velocity of the D atoms. Without the probe field at 243 nm, only channels (1) and (3) are present. 3

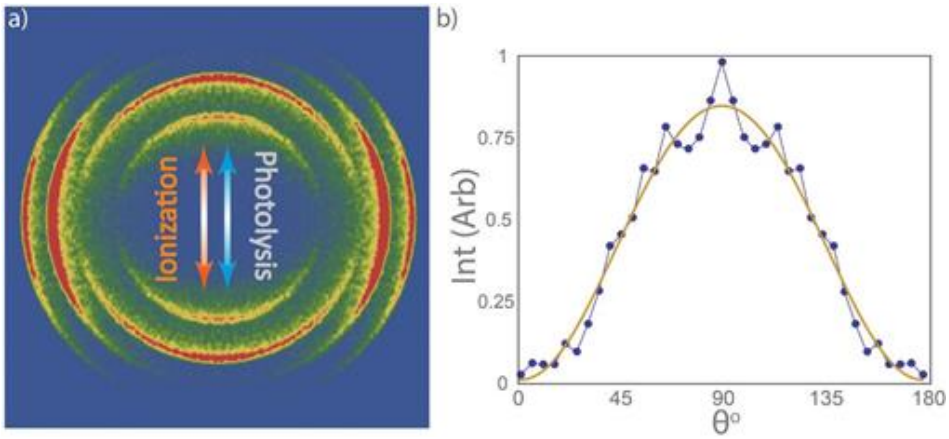

Figure 4.1: a) Sliced ion image of the deuterium ions produced by the DI photodissociation. The photolysis and ionization lasers counterpropagate along the 90 - 270° direction, while the direction of their linear polarization is marked by the arrows. b) Angular distribution of the ions corresponding to DI+270nm → D+I($^2P_{3/2}$)(points) and fit with Eq. 3 (orange solid line).

,

Channel (1) is accessed by a parallel transition to the $\alpha^3\,\Pi_{0+}$ state, and does not yield SPD:

$$DI\ (\Omega_\alpha = 0) \rightarrow D(m_S = \pm 1/2) + I^*\left(m_J = \pm 1/2\right) \quad (1)$$

Channel (3) is accessed by a perpendicular transition to the $A^1\Pi_1$ state, and yields SPD:

$$DI\ (\Omega_\alpha = \pm 1) \rightarrow D(m_S = \pm 1/2) + I\left(m_J = \pm 3/2\right) \quad (2)$$

Circularly polarized photolysis light σ^+ excites the Ω_A =+1 state (or σ^- excites the Ω_A= -1), *only* for photofragment recoil direction $\hat{u}$ parallel to the propagation direction $\hat{k}$ (θ_{vk} = 0; see Figure 4.2). Otherwise, a coherent superposition of the two $\Omega_A = \pm 1$ states is excited and SPD polarization falls as $\hat{v} \cdot \hat{k} = \cos\theta_{vk}$. This loss in polarization can be minimized by aligning the DI bonds using a strong nonresonant laser pulse[32,33], along $\hat{k}$ just before photodissociation, which also eliminates the unwanted unpolarized D+I* channel (1).

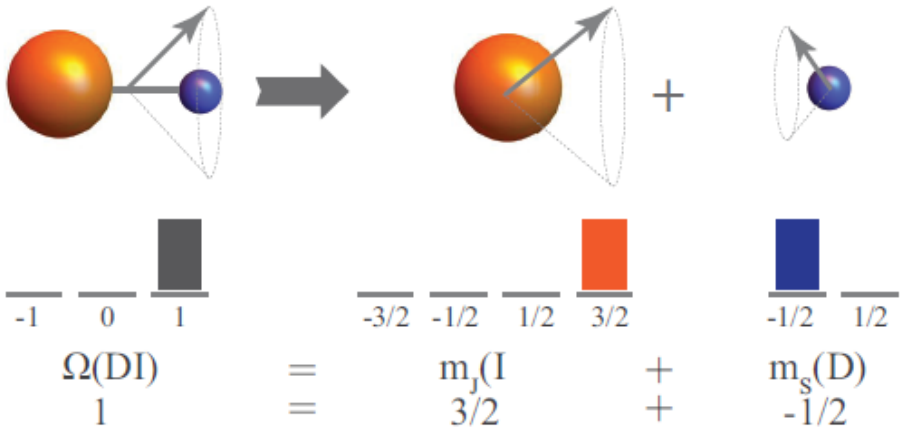

Figure 4.2: The angular momentum projection Ω_A=+1 is prepared from the DI = 0 ground state, using ± circularly polarized photolysis light, and is distributed to the angular momentum projections of the photofragments after photodissociation.

The angular distribution of the polarized photofragments along the quantization axis can be expressed as an even expansion of Legendre polynomials[32,34] up to the fourth order:

$I(\theta)/I_0 = 1 + \beta_2 P_2(cos\theta) + \beta_4 P_4(cos\theta)$ (3)

where $P_n(x)$ is the nth-order Legendre polynomial. Fig. 4.1b depicts the angular distribution of the deuterium ions correlated with the production of I atoms at 270 nm, as well as a fit using Eq. 3, for which $\beta_2 = \beta$ and $\beta_4 = 0$. The value of the spatial-anisotropy β parameter extracted by this fit is β = -0.98±0.03, corresponding to an almost purely perpendicular transition, in agreement with theoretical predictions[11] .

Figure 4.3a-e show sliced ion images of I atoms produced by DI+270 nm → D + I and detected via the $^2P_{3/2} \rightarrow\rightarrow {}^4P_{1/2}$ REMPI transition at 303.6 nm. The intensities of the 6 ns dissociation and ionization laser pulses were ~1 and ~ 0.5 mJ, respectively, and both were focused with f = 30 cm lenses. In Fig. 4.3a, both the photolysis and the ionization laser pulses are right-circularly polarized (RCP); the angular distribution is strongly anisotropic, with most of the photofragments recoiling preferentially along the propagation direction of the laser beams. For Figure 4.3b, the photolysis laser has opposite helicity: left-circularly polarized (LCP), and we see a very big change in the angular distribution, as it is nearly isotropic. The ratio of the total intensities of the images in Figure 4.3(a and b) is $I_0(RR)/I_0(LR) = 1.8 \pm 0.2$. Together, these measurements show that the I atoms are strongly polarized. Figures 4.3c-e show images using linearly polarized photolysis and ionization lasers, aligned in the geometries (XX), (XZ), and (ZX), respectively.

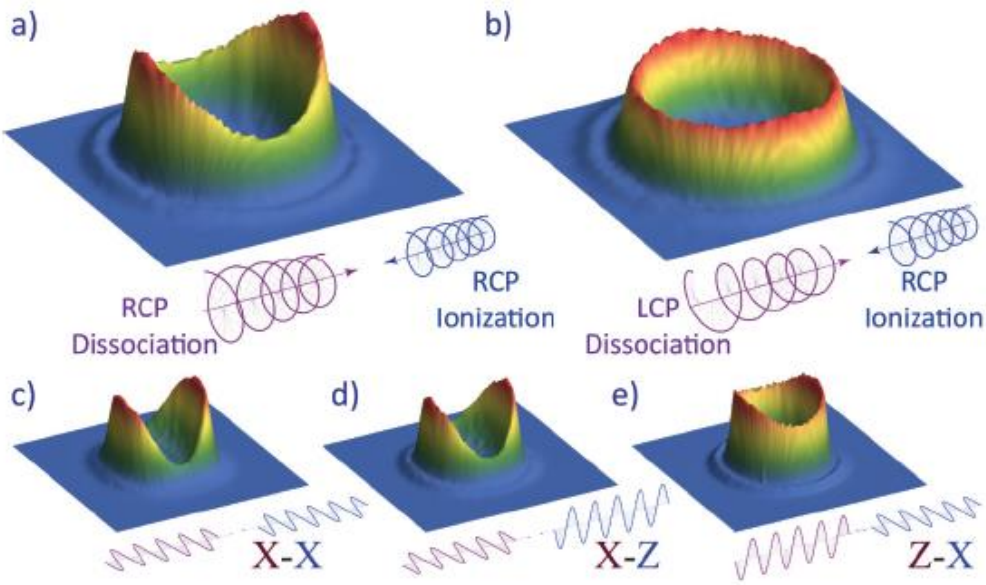

Figure 4.3: Sliced ion image of I ions produced with the polarizations of the photolysis laser (λ=270 nm) and the ionization laser (λ=303.6 nm) being a) both right circularly polarized (RCP), b)left circularly polarized (LCP) and RCP c) both linearly polarized parallel to the image plane X d) linearly polarized along X, and linearly polarized perpendicular to the image plane Z e) linearly polarized along Z, and linearly polarized along X.

The measured β are consistent with those of the dissociation mechanism predicted at a significantly higher energy, 47.000 cm^{-1}.[11] However, at lower energies, the dissociation is predicted to switch to excitation and adiabatic dissociation via the $a^3\Pi_1$ state, producing m_J (I) = +1/2 and m_S(D) =+1/2 [11]; the energy of this mechanism switch, predicted between 37.000-44.000 cm^{-1}, is strongly model dependent.[35] Our results at 37.000 cm^{-1} do not show this mechanism switch, indicating that the dissociation models may need to be modified.

Highly polarized D, and likely T, can be produced by deuterium and tritium halide photodissociation, respectively, using ps photodissociation and ionization lasers (DI photodissociation is saturated by 5 mJ/pulse 270 nm, focused to 100 μm). Highly polarized ^{3}He can be produced by spin-exchange optical pumping.[36,37] Subsequently, using the conditions described above, laser fusion of D-T or D-^{3}He will give neutron or proton reaction products with angular distributions of the form $\alpha + \sin^2\theta$ about the spin quantization axis5 (where a = 0 for fully polarized spins; for D polarization p_z=0.55 and p_{zz}=0 [38], α ~1 for reaction with T polarization of p_z= 0.95, and a ~2 for ^{3}He with pz=0.76[39]). Such large spatial anisotropy contrasts can determine whether spin polarization survives laser plasma (question 1). In addition, the neutron products will be spin polarized5 and can be measured with neutron polarimeters.[40] Finally, polarized D-D reaction cross sections can be measured by comparing (in a single laser shot) the ratios of the total signal and angular distributions of the D-D and D-T (or D-^{3}He) reaction products, for the cases of polarized, and unpolarized, reactants (question 2).

4.4 References

[1]Rakitzis, T. Spin-Polarized Hydrogen Atoms from Molecular Photodissociation. *Science* 2003, *300*, 1936-1938.

[2]Rakitzis*, T. Pulsed-Laser Production and Detection Of Spin-Polarized Hydrogen Atoms. *ChemPhysChem* 2004, *5*, 1489-1494.

[3] Rakitzis, T.; Samartzis, P.; Toomes, R.; Kitsopoulos, T. Measurement of Br Photofragment Orientation and Alignment From HBr Photodissociation: Production Of Highly Spin-Polarized Hydrogen Atoms. *The Journal of Chemical Physics* 2004, *121*, 7222-7227.

[4] Sofikitis, D.; Rubio-Lago, L.; Bougas, L.; Alexander, A.; Rakitzis, T. Laser Detection of Spin-Polarized Hydrogen from HCl And HBr Photodissociation: Comparison Of H- And Halogen-Atom Polarizations. *The Journal of Chemical Physics* 2008, *129*, 144302.

[5] Sofikitis, D.; Rubio-Lago, L.; Alexander, A.; Peter Rakitzis, T. Nanosecond Control and High-Density Production of Spin-Polarized Hydrogen Atoms. *EPL (Europhysics Letters)*2008, *81*, 68002.

[6] Van Brunt, R.; Zare, R. Polarization of Atomic Fluorescence Excited by Molecular Dissociation. *The Journal of Chemical Physics* 1968, *48*, 4304-4308.

[7] Betti, R.; Hurricane, O. Inertial-Confinement Fusion with Lasers. *Nature Physics*2016, 435-448.

[8] Balint-Kurti, G.; Orr-Ewing, A.; Beswick, J.; Brown, A.; Vasyutinskii, O. Vector Correlations and Alignment Parameters in The Photodissociation Of HF And DF. *The Journal of Chemical Physics* 2002, *116*, 10760-10771.

[9] Brown, A.; Balint-Kurti, G.; Vasyutinskii, O. Photodissociation Of HCl And DCl: Polarization of Atomic Photofragments. *The Journal of Physical Chemistry A* 2004, *108*, 7790-7800.

[10] Smolin, A.; Vasyutinskii, O.; Balint-Kurti, G.; Brown, A. Photodissociation Of Hbr. 1. Electronic Structure, Photodissociation Dynamics, And Vector Correlation Coefficients†. *The Journal of Physical Chemistry A* 2006, *110*, 5371-5378.

[11] Broderick, B.; Lee, Y.; Doyle, M.; Chernyak, V.; Vasyutinskii, O.; Suits, A. Spin-Polarized Hydrogen Rydberg Time-Of-Flight: Experimental Measurement Of The Velocity-Dependent H Atom Spin-Polarization. *Review of Scientific Instruments* 2014, *85*, 053103.

[12] Steffens, E.; Haeberli, W. Polarized Gas Targets. *Reports on Progress in Physics*2003, *66*, 1887-1935.

[13] Ciullo, G.; Engels, R.; Büscher, M.; Vasilyev, A. *Nuclear Fusion With Polarized Fuel*,pp.1-13.

[14] Engels, R.; Grigoryev, K.; Kochenda, L.; Kravtsov, P.; Mikirtytchiants, M.; Rathmann, F.; Paetz gen. Schieck, H.; Ströher, H.; Trofimov, V.; Vasilyev, A. et al. Polarized Fusion. *Physics of Particles and Nuclei* 2014, *45*, 341-343.

[15] C. Leemann, H. Burgisser, P. Huber, U. Rohrer,H. Paetz gen. Schieck, and F. Seiler. Investigation of the $^{3}He(d,p)^{4}He$ with polarized beam and Target at 430keV. *Annals of Physics* 1971, 45,810.

[16] Kulsrud, R.; Furth, H.; Valeo, E.; Goldhaber, M. Fusion Reactor Plasmas with Polarized Nuclei. *Physical Review Letters* 1982, *49*, 1248-1251.

[17] More, R. Nuclear Spin-Polarized Fuel in Inertial Fusion. *Physical Review Letters*1983, *51*, 396-399.

[18] Didelez, J.; Deutsch, C. DD Fusion From A Polarized HD Target. *Laser and Particle Beams* 2015, *33*, 211-214.

[19] Pace, D.; Lanctot, M.; Jackson, G.; Sandorfi, A.; Smith, S.; Wei, X. Controlling Fusion Yield In Tokamaks With Spin Polarized Fuel, And Feasibility Studies On The DIII-D Tokamak. *Journal of Fusion Energy* 2015, *35*, 54-62.

[20] Fletcher, K.; Ayer, Z.; Black, T.; Das, R.; Karwowski, H.; Ludwig, E.; Hale, G. Tensor Analyzing Powers For $H_2(d,p)^{3}H$ And $H_2(d,n)3He$ At Deuteron Energies Of 25, 40, 60, And 80 Kev. Physical Review C 1994, 49,2305-2310.

[21] G. Hale and G. Doolen, Cross sections and Maxwellian reaction rates for polarized d + d reactions,LA-9971-MS, Los Alamos (1984).

[22] Hofmann, H.; Fick, *D.* Fusion of Polarized Deuterons. *Physical Review Letters*1984, 52, 2038-2040.

[23] Lemaître, S.; Paetzgen. Schieck, H. Complete Determination Of The Transition Amplitudes From A Comprehensive Data Analysis Of The Fusion Reactions $D(d,p)^{3}H$ And $D(d,p)^{4}He$ For E_D<500 KeV. *Annalen der Physik* 1993, 505, 503-521.

[24] Zhang, J.; Liu, K.; Shuy, G. Fusion Reactions of Polarized Deuterons. *Physical Review Letters* 1986, *57*, 1410-1413.

[25] Zhang, J.; Liu, K.; Shuy, G. Neutron Suppression in Polarized dd fusion Reaction. *Physical Review C* 1999, *60*.

[26] Iio, M.; Daito, I.; Doshita, N.; Hasegawa, T.; Horikawa, N.; Inagaki, T.; Ishii, S.; Iwata, T.; Kobayashi, T.; Kondo, K. et al. Development Of A Polarized Target For Nuclear Fusion Experiments. *Nuclear Instruments and Methods in Physics Research*

Section A: Accelerators, Spectrometers, Detectors and Associated Equipment 2004, *526*, 190-193.

[27] Eppink, A.; Parker, D. Velocity Map Imaging of Ions and Electrons Using Electrostatic Lenses: Application In Photoelectron And Photofragment Ion Imaging Of Molecular Oxygen. *Review of Scientific Instruments* 1997, *68*, 3477-3484.

[28]Bougas, L.; Sofikitis, D.; Everest, M.; Alexander, A.; Rakitzis, T. (2+1) Laser-Induced Fluorescence of Spin-Polarized Hydrogen Atoms. *The Journal of Chemical Physics* 2010, *133*, 174308.

[29] C. R. Gebhardt, T. P. Rakitzis, P. C. Samartzis,V. Ladopoulos and T. N. Kitsopoulos, Slice Imaging: A New Approach to Ion Imaging and Velocity Mapping, *Rev. Sci. Instrum*., 2001, 72(10), 3848.

[30] V. Papadakis and T. N. Kitsopoulos, Slice Imaging and Velocity Mapping Using a Single Field, *Rev. Sci. Instrum*., 2006, 77(8), 5.

[31] Eppink, A.; Parker, D. Velocity Map Imaging of Ions and Electrons Using Electrostatic Lenses: Application In Photoelectron And Photofragment Ion Imaging Of Molecular Oxygen. *Review of Scientific Instruments* 1997, 68, 3477-3484.

[32] Siebbeles, L.; Glass-Maujean, M.; Vasyutinskii, O.; Beswick, J.; Roncero, O. Vector Properties In Photodissociation: Quantum Treatment Of The Correlation Between The Spatial Anisotropy And The Angular Momentum Polarization Of The Fragments. *The Journal of Chemical Physics* 1994, *100*, 3610-3623.

[33] Vrakking, M.; Stolte, S. Coherent Control of Molecular Orientation. *Chemical Physics Letters* 1997, *271*, 209-215.

[34] Zare, R.; Herschbach, D. Doppler Line Shape of Atomic Fluorescence Excited by Molecular Photodissociation. *Proceedings of the IEEE* 1963, *51*, 173-182.

[35] Jodoin, D.; Brown, A. Photodissociation Of HI and DI: Testing Models For Electronic Structure Via Polarization Of Atomic Photofragments. *The Journal of Chemical Physics*2005, *123*, 054301.

[36] Lee, K.; Hansen, J.; van den Brand, J.; Milner, R. A Laser Optically Pumped Polarized 3He Target for Storage Rings. *Nuclear Instruments and Methods in Physics Research Section A: Accelerators, Spectrometers, Detectors and Associated Equipment* 1993, *333*, 294-303.

[37] Walker, T.; Happer, W. Spin-Exchange Optical Pumping of Noble-Gas Nuclei. *Reviews of Modern Physics* 1997, *69*, 629-642.
[38] Paetz gen. Schieck, H. The Status Of "Polarized Fusion". *The European Physical Journal A* 2010, *44*, 321-354.
[39] Karpuk, S.; Allmendinger, F.; Burghoff, M.; Gemmel, C.; Güldner, M.; Heil, W.; Kilian, W.; Knappe-Grüneberg, S.; Mrozik, C.; Müller, W. et al. Spin Polarized 3He: From Basic Research to Medical Applications. *Physics of Particles and Nuclei* 2013, *44*, 904-908.
[40] Simmons, J.; Perkins, R. Liquid Helium Scintillation Counter As A Neutron Polarimeter. *Review of Scientific Instruments* 1961, *32*, 1173-1178.

5 Appendix A: Publications

6 Appendix B: Ion Images of CH_3Br

Methyl Ion Images

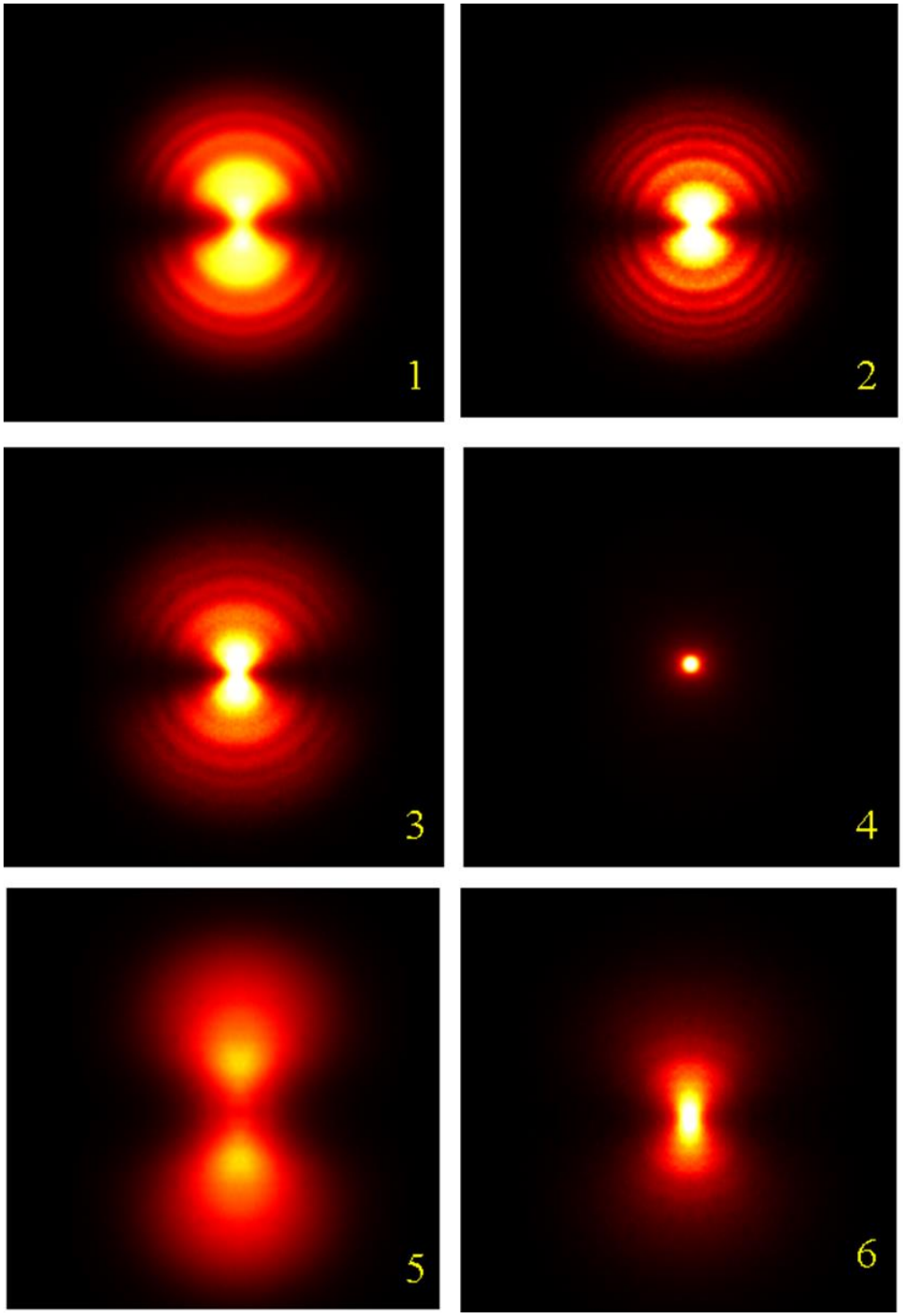

Figure: $CH3^+$ ion images for excitations 1-6.

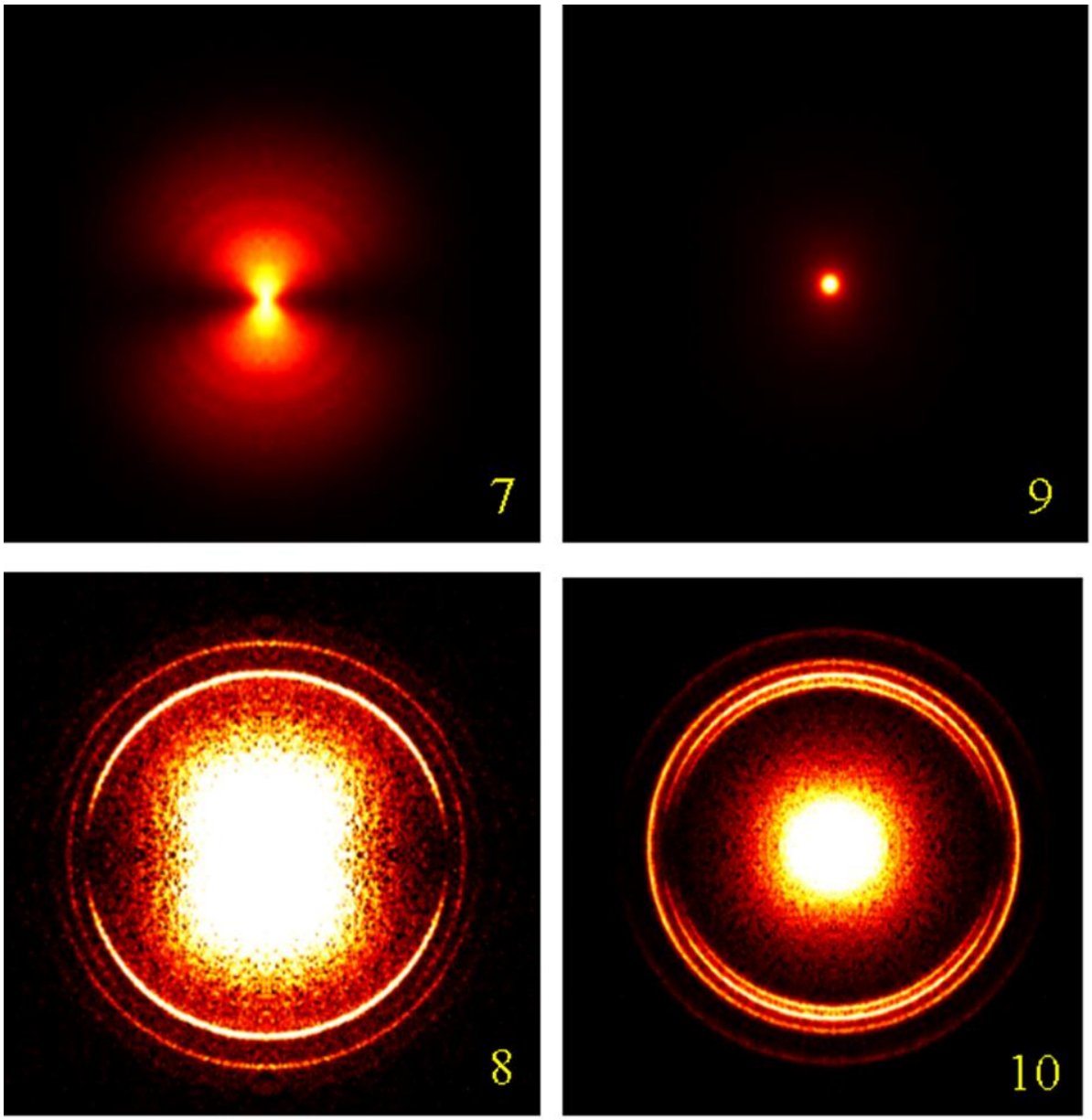

Figure: $CH3^+$ ion images for excitations 7-10.

Bromine Ion Images

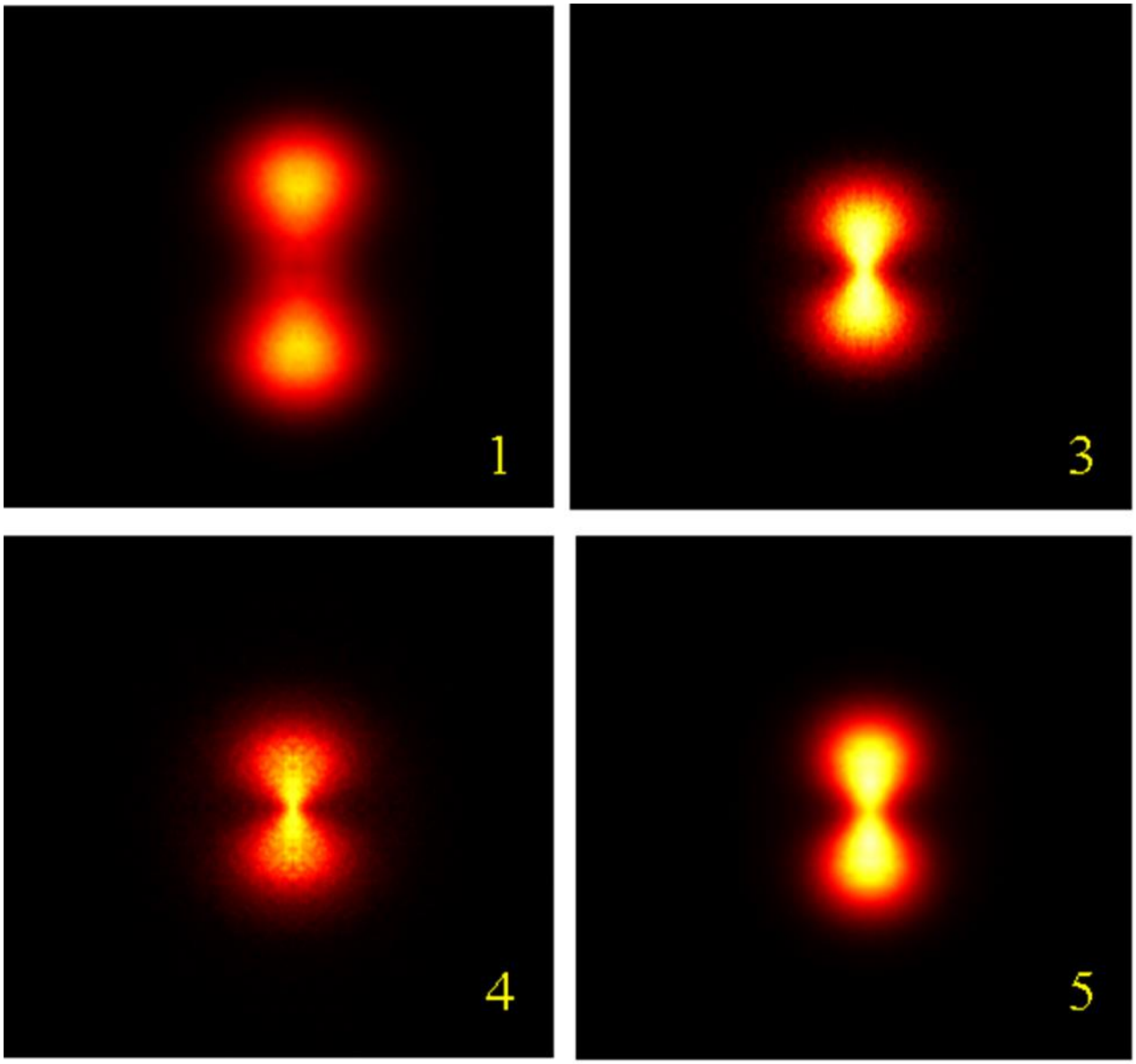

Figure: Br^+ ions for excitations no.1,3,4,5.

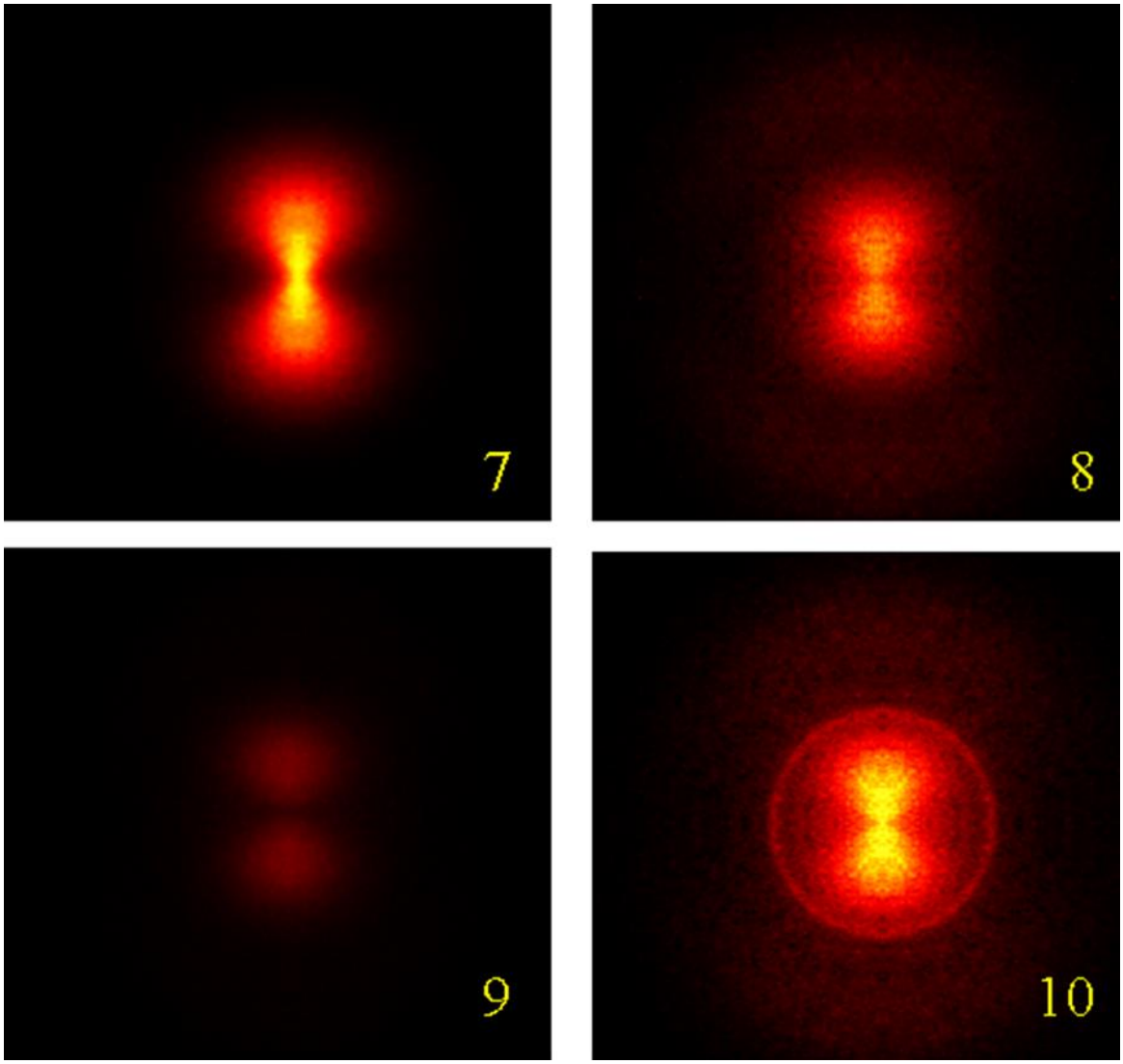

Figure: Br^+ ions for excitations no.7,8,9,10.

7 Appendix C

CH_3I Ion Slice Images and Photoelectron Images

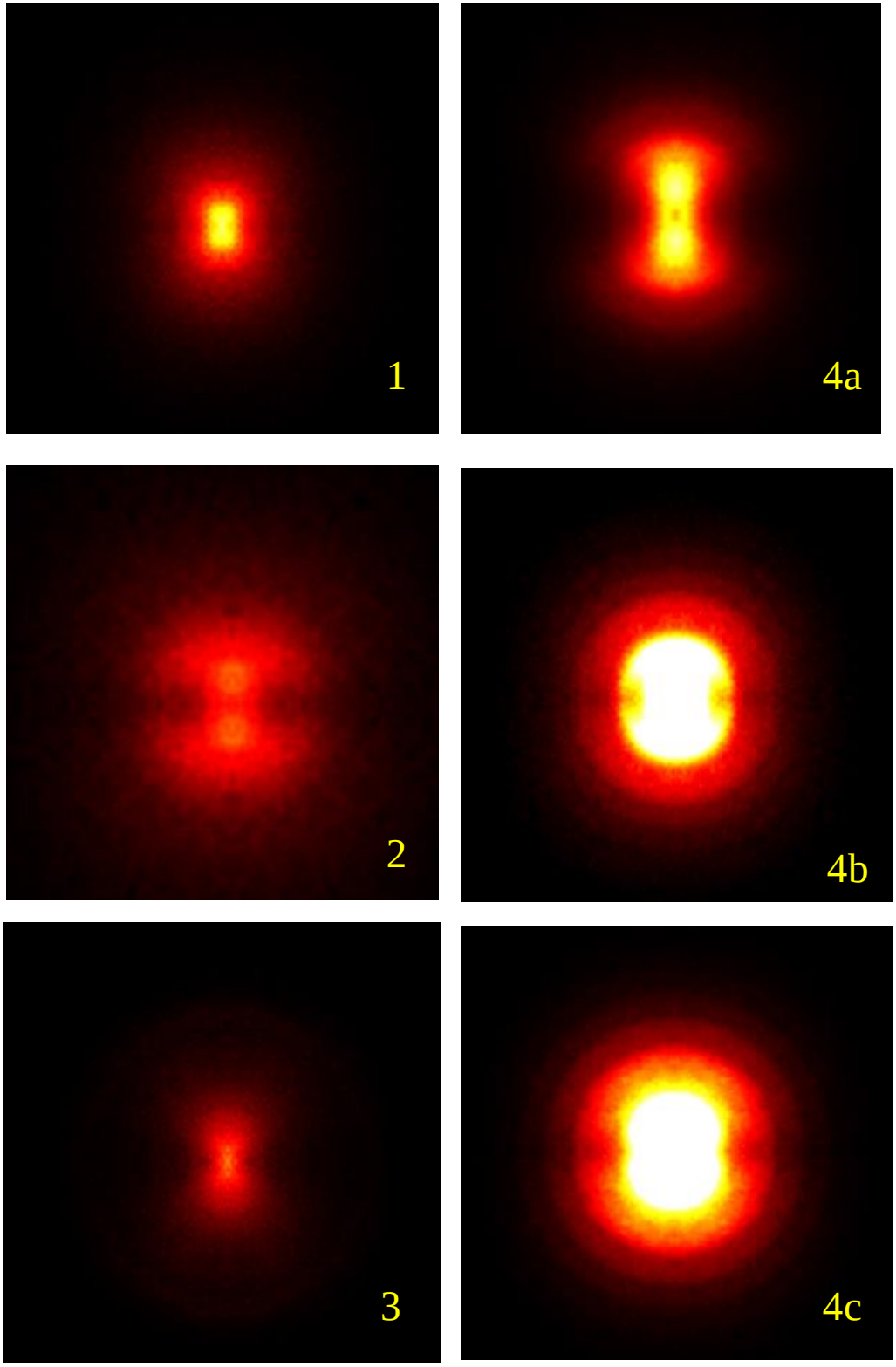

Figure 7.1 Methyl Ion Images for Excitations no.1,2,3,4a-c

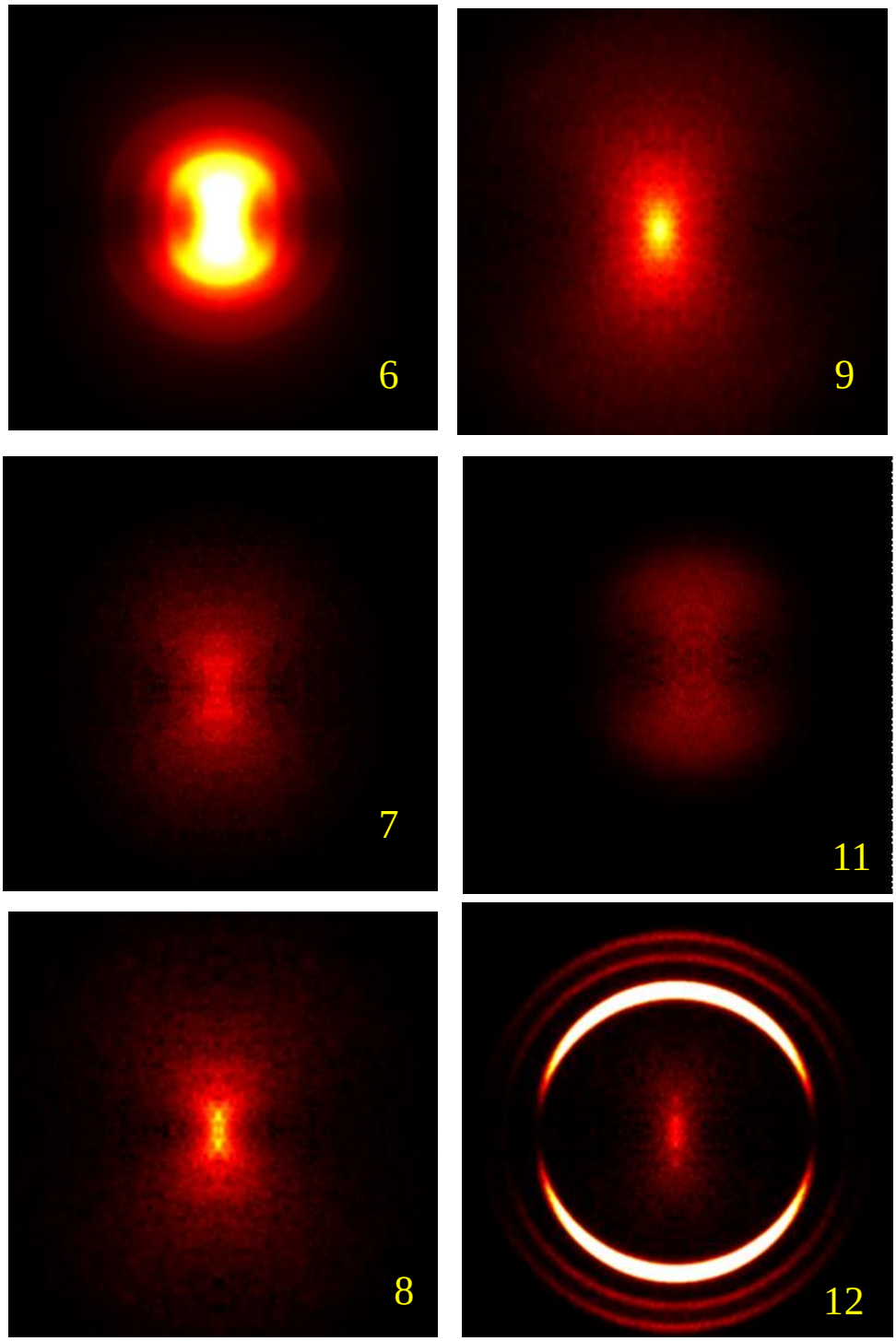

Figure 7.2 Methyl Ion Images for Excitations no.6,7,8,9,11,12

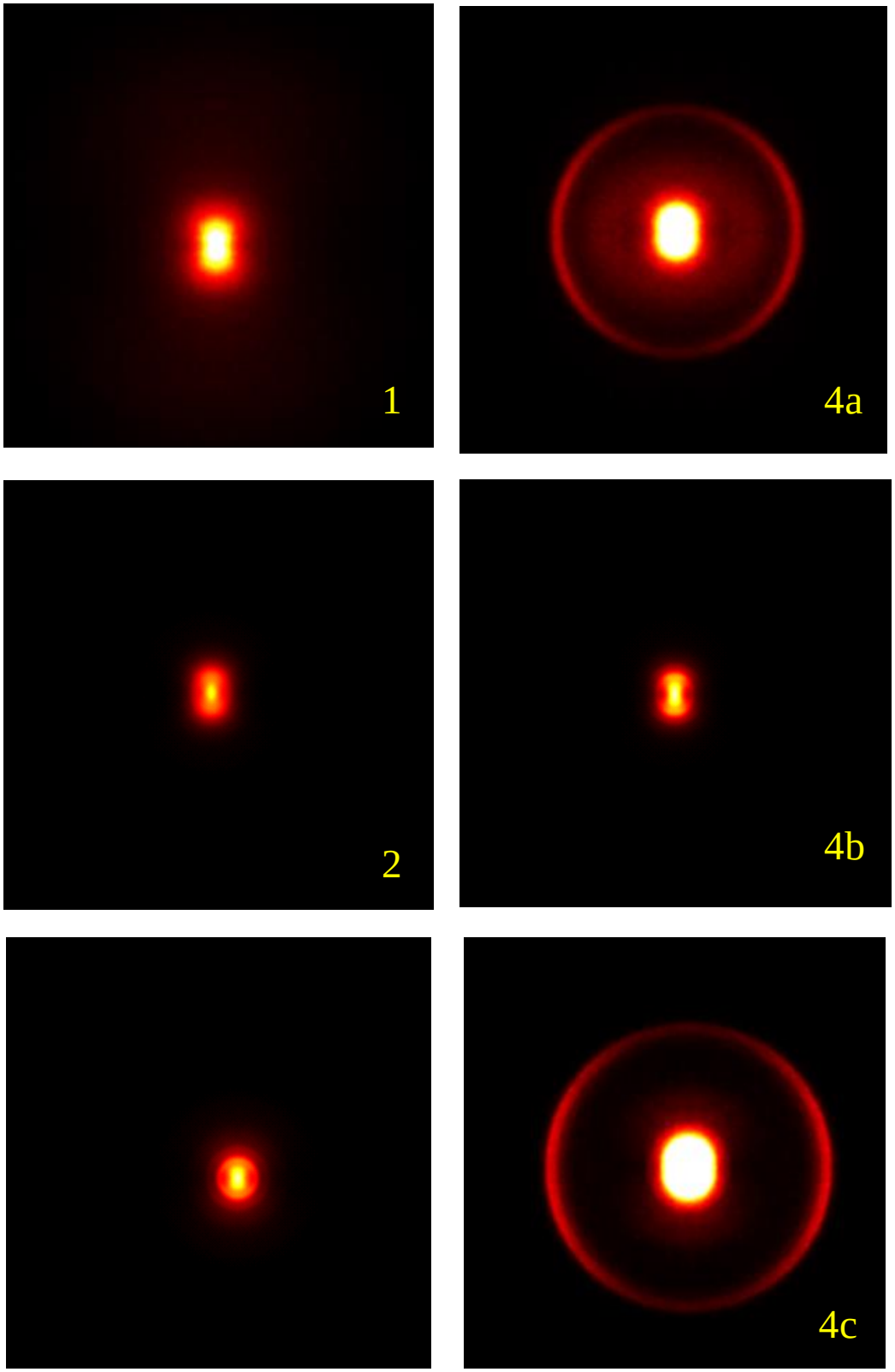

Figure 7.3 Iodine Ion Images for Excitations no.1,2,3,4a-c

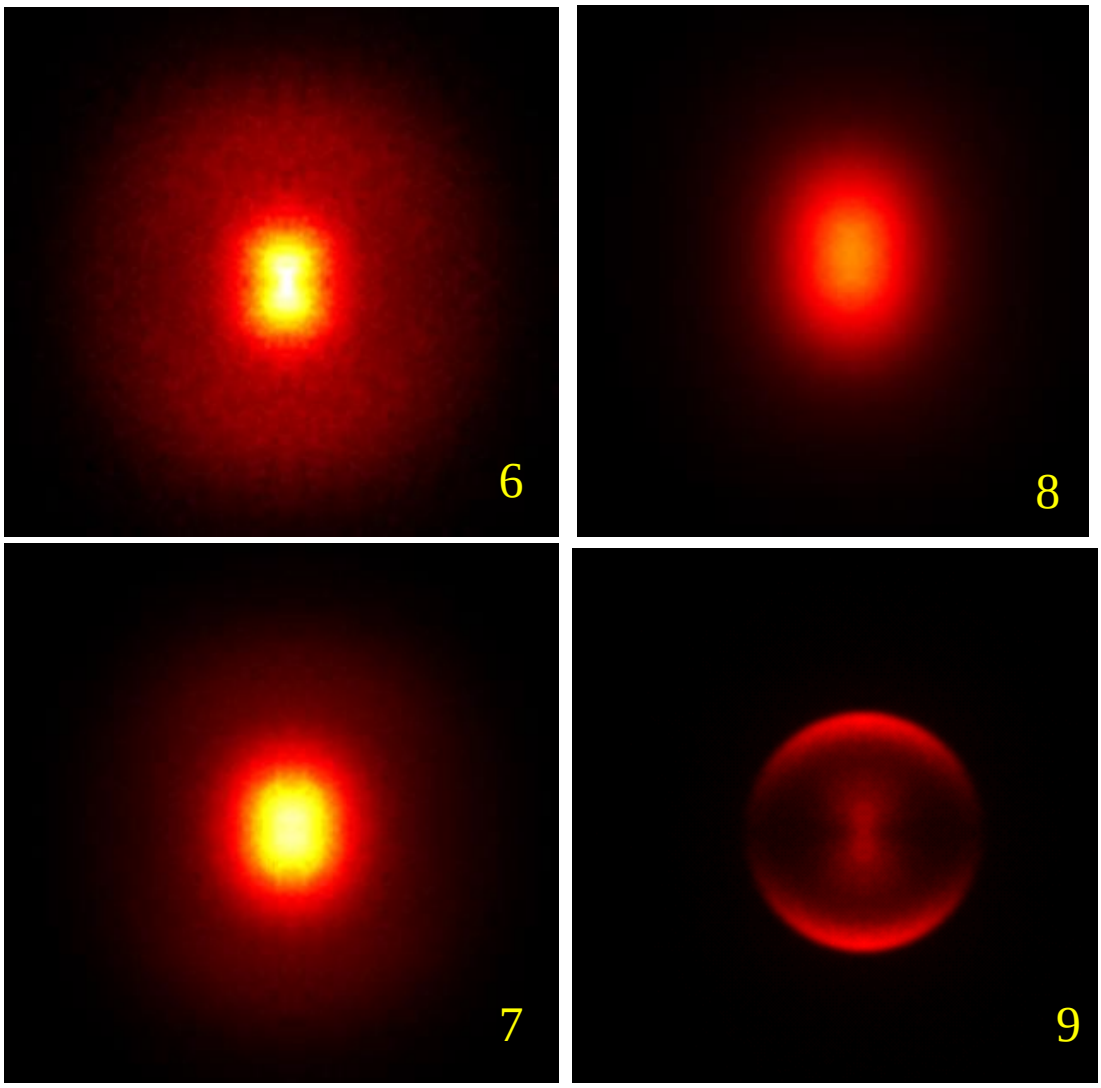

Figure 7.4 Iodine Ion Images for Excitations no.6,7,8,9

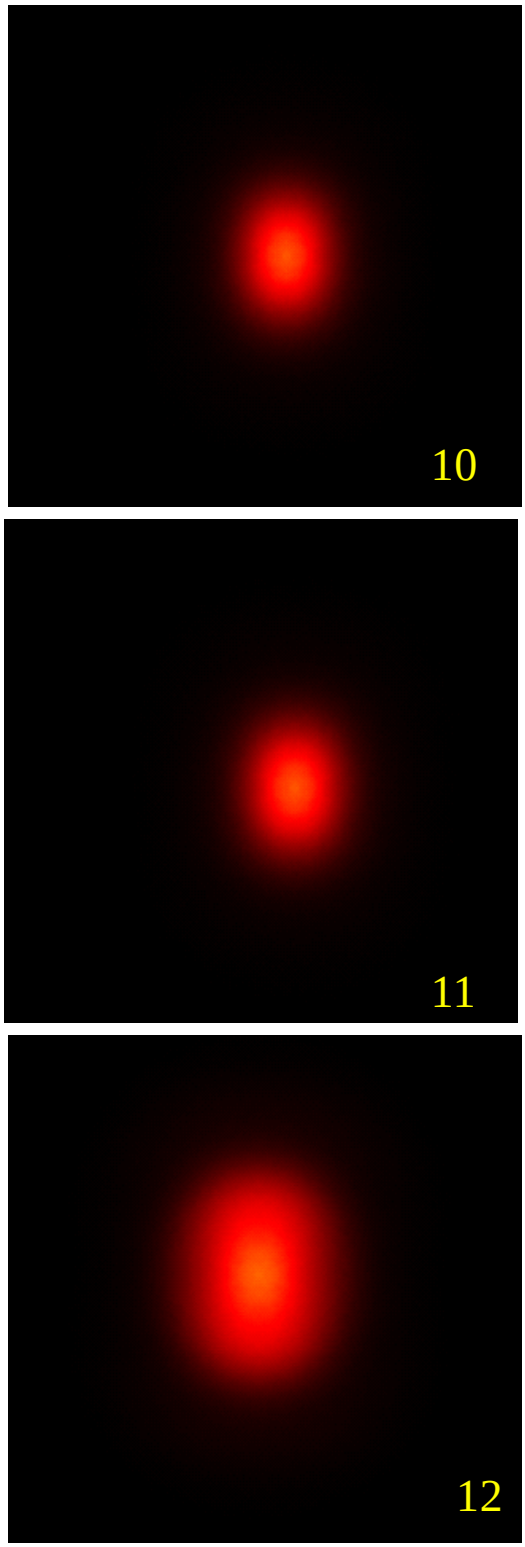

Figure 7.5 Iodine Ion Images for Excitations no.10,11,12

Photoelectron Images

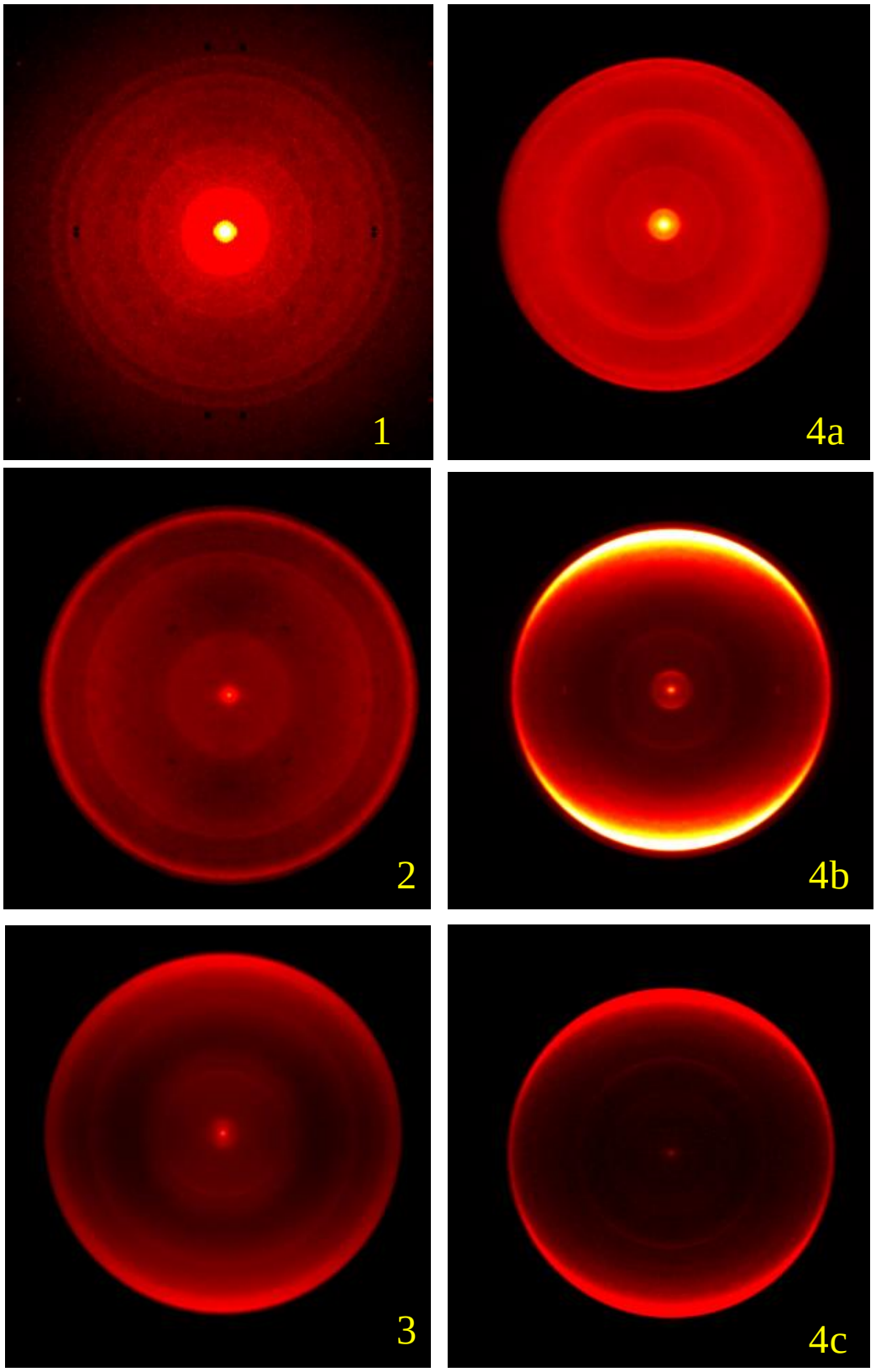

Figure 7.6 Photoelectron Images for excitations no.1,2,3,4a-c

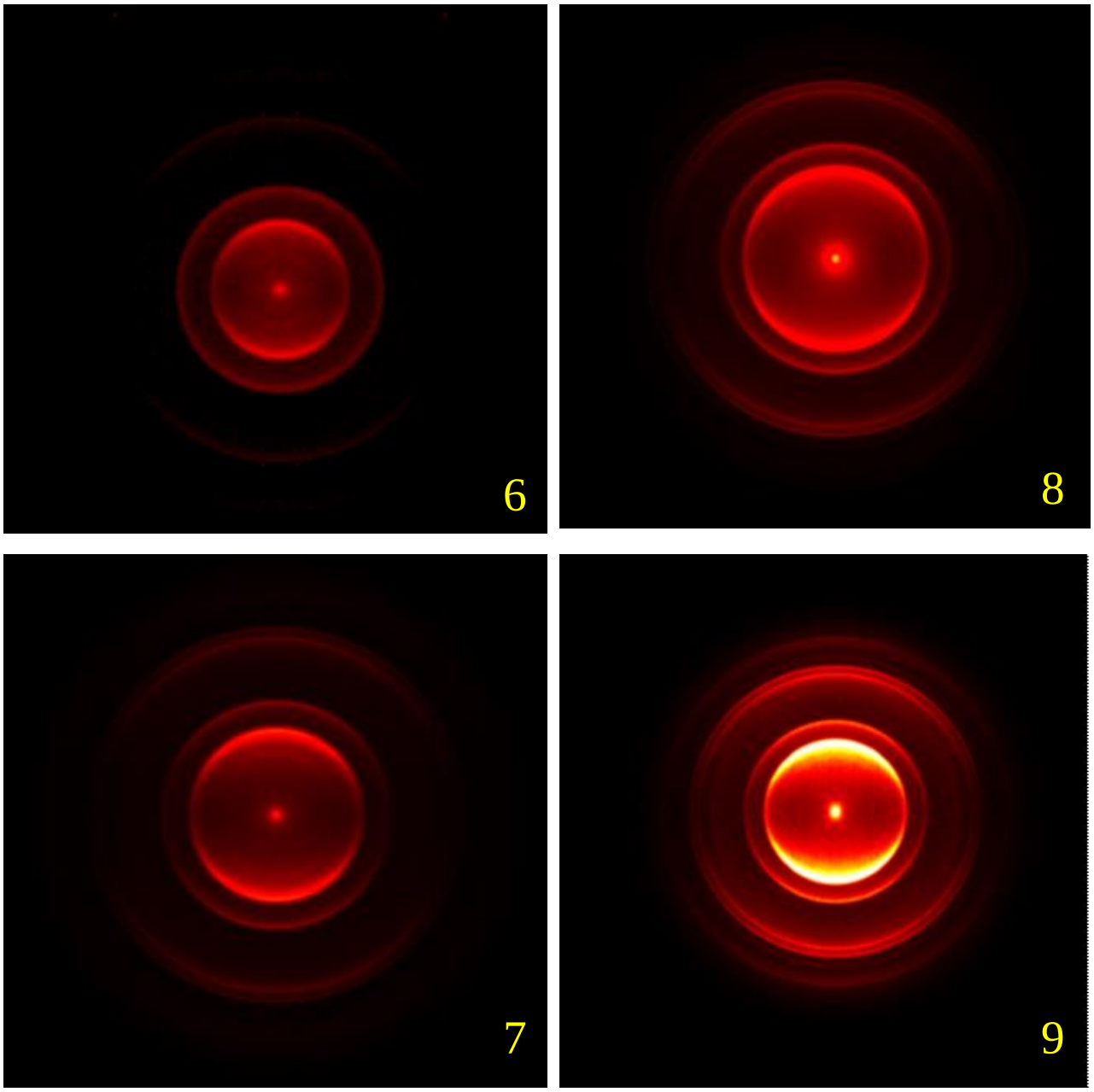

Figure 7.7 Photoelectron Images for Excitations no.6,7,8,9

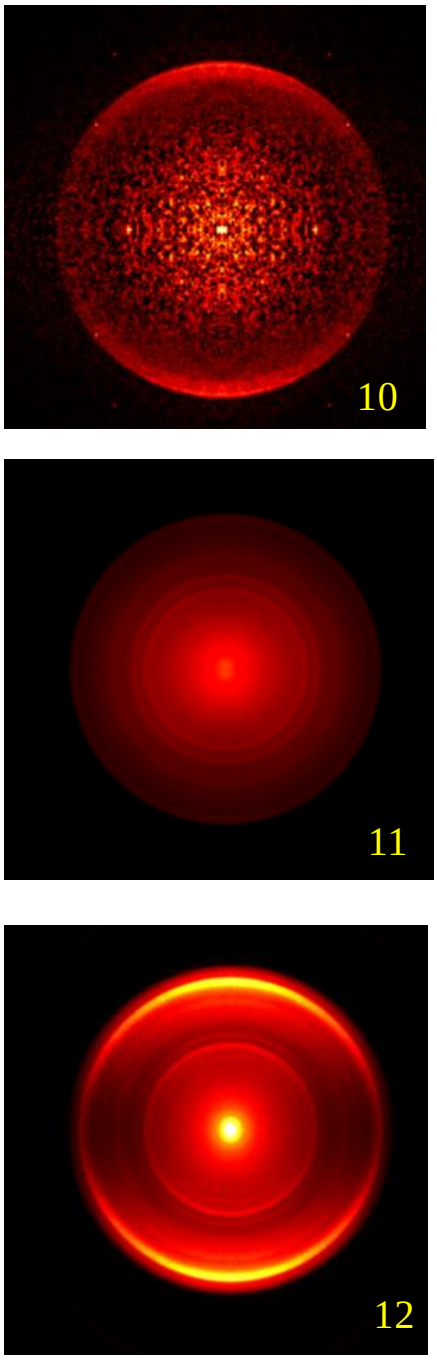

[s]Figure 7.8 **Photoelectron Images for Excitations no.10,11,12**

Highly spin-polarized deuterium atoms from the UV dissociation of Deuterium Iodide.

Dimitris Sofikitis,[1,2] Pavle Glodic,[1] Greta Koumarianou,[1,3] Hongyan Jiang,[4] Lykourgos Bougas,[1,2,*] Peter C. Samartzis,[1,3] Alexander Andreev,[5,6] and T. Peter Rakitzis[*1,2]

[1]*Institute of Electronic Structure and Laser, Foundation for Research and Technology-Hellas, 71110 Heraklion-Crete, Greece.*
[2]*Department of Physics, University of Crete, 71003, Heraklion-Crete, Greece.*
[3]*Department of Chemistry, University of Crete, 71110, Heraklion-Crete, Greece.*
[4]*Max Planck Institute for Biophysical Chemistry Fassberg 11, D-37077 Göttingen, Germany.*
[5]*IELI-ALPS, 6720 Szeged, Hungary*
[6]*Max Born Institute, 12489 Berlin, Germany.*

(Dated: September 11, 2018)

We report the production of highly spin-polarized Deuterium atoms via photodissociation of deuterium iodide at 270 nm. The velocity distribution of both the deuterium and iodine photodissociation products is performed via velocity mapping slice-imaging. Additionally, the angular momentum polarization of the iodine products is studied using polarization-sensitive ionization schemes. The results are consistent with excitation of the $A^1\Pi_1$ state followed by adiabatic dissociation. The process produces ∼100% electronically polarized deuterium atoms at the time of dissociation, which is then converted to ∼ 60% nuclear D polarization after ∼ 1.6 ns. These production times for hyperpolarized deuterium allow collision-limited densities of ∼ 10^{18} cm^{-3}, which is ∼ 10^6 times higher than conventional (Stern-Gerlach separation) methods. We discuss how such high-density hyperpolarized deuterium atoms can be combined with laser fusion to measure polarized D-D fusion cross sections.

PACS numbers: 33.80.Gj, 32.10.Fn

Controlling the nuclear spin polarization in fusion reactions offers important advantages, such as larger reaction cross sections, control over the emission direction of products, and in some cases eliminating hazardous neutron emission [1, 2]. In the case of the five-nucleon reactions D + T → n + ^{4}He and D + ^{3}He → p + ^{4}He, it is well known that the reaction cross section increases by ∼50% when the fused nuclei have oriented nuclear spins [3, 4].

For the 4-nucleon D+D reaction, over the important energy range of 10-100 keV, the situation is unclear, since several predictions range from enhancement of the reaction, suppression of the reaction, or almost no effect at all [5–10]. The technical challenges of measuring fusion polarization dynamics limits the number of experiments which pursue this direction to two facility-scale experiments [11]. These experiments achieve nuclear spin polarization by magnetically separating the nuclear spin states via the Stern-Gerlach effect in molecular beams, a process however which limits the achievable production rates to ∼ 10^{16} atoms s^{-1} [2], and the projected D-D fusion reaction rate to as low as ∼0.01 neutrons s^{-1} [12]. Polarized solid deuterium targets can be produced where the densities can reach as high as 2.5×10^{19} spins/cm^3, albeit in much lower polarization close to 10% [13]. Another approach for the production of polarized sold fuel involves accumulating the hyperpolarized deuterium in specially coated storage cells [11].

Laser photodissociation of hydrogen halides has been shown to produce highly polarized H atoms [14–17]. The photodissociation process initially polarizes the electron spin up to 100% (for photofragment velocities parallel to the propagation direction of the circularly-polarized dissociation laser) [18]; due to the hyperfine interaction, the polarization oscillates back and forth between the electronic and the nuclear spin on the ∼1-ns timescale. By terminating this polarization exchange appropriately, for example by ionizing the atom, one can isolate the polarization on the electronic or nuclear spin. This ultrafast production mechanism allows the production of spin-polarized H atoms at densities many orders of magnitude higher than the traditional Stern-Gerlach spin-separation method. This pulsed production of hyperpolarized H, if also extended to the production of hyperpolarized D atoms, can be used to study polarized D fusion reactions at high density, with much larger signals than conventional beam methods. The D atoms can be used to produce pulsed ion beams, allowing the possibility of measuring polarized fusion reaction cross sections over a large energy range. The pulsed production can also be combined with Inertial Confinement Fusion (ICF), where fusion is induced by an intense short laser pulse. The photolysis and fusion pulses can be timed so that the D nuclei is maximally polarized when fusion occurs; such a combination can offer a straightforward method for measuring the effect of polarization in the D reactions, in densities close to 10^{18} cm^{-3}, at collision energies of $\sim 10-50$ keV.

Theoretical calculations of the photofragment polarizations (over a range of UV photodissociation energies) have been performed for nearly all the hydrogen halides: HF/DF [19], HCl/DCl [20], HBr [21], and HI/DI [22]. At least two competing dissociation mechanisms occur: excitation to a dissociative state followed by adiabatic dissociation producing hydrogen atoms with

spin-down electrons, excitation to another dissociative state followed by adiabatic dissociation producing hydrogen atoms with spin-up electrons (also nonadiabatic transitions between dissociative states can change the H-atom polarization). Therefore, depending on the contribution from each mechanism, the hydrogen electronic spin polarization P_e can range from fully spin up (P_e=1) to fully spin-down (P_e=-1), and anything in between, including unpolarized (P_e=0). Calculations predict that P_e can take values over this complete range, and depends strongly on the photolysis energy, on the halide cofragment (X=F,Cl,Br, or I), and the hydrogen isotope (H or D). For example, near maximal H polarizations ($|P_e| = 1$) are calculated at some energies for photodissociation of the hydrogen halides HCl, HBr, and HI (of which HCl and HBr have been measured at 193 nm [14, 15]), and the deuterium halides DF and DI (which have not been measured previously). Here we measure the polarization of the D and I photofragments from the photodissociation of DI molecules at 270 nm, with the goal of demonstrating a source of highly polarized high-density D atoms.

The experiments are performed using a molecular beam set-up, to facilitate polarization sensitive detection. We measure the spin polarization of the iodine atoms via a Resonance-Enhanced Multiphoton Ionisation (REMPI) scheme and infer the deuterium polarization by angular momentum conservation; past experiments of direct measurements of hydrogen spin polarization [16, 17] give excellent agreement with indirect detection. Measuring directly the spin polarization in hydrogen (or deuterium) atoms, usually requires the use of Vacuum-Ultra-Violet (VUV) sources [16, 17, 23]. Non VUV detection of spin polarized hydrogen has been reported, but using laser-induced fluorescence (LIF) detection and not REMPI [24].

The experimental set-up has been explained in detail elsewhere [25, 26]. Briefly, deuterium iodide is mixed with He in a 50% ratio and expanded into the chamber via a pulsed nozzle, giving a molecule flux is $\sim 10^{17}$ molecules/s. The molecular beam is intersected at right angles roughly 50 cm downstream by the focused photolysis and probe laser beams. The resulting ion sphere is focused by a single ion lens on a gated position sensitive detector , thus performing velocity map imaging. [27].

In Fig. 1 we see a characteristic image of the D ions produced by dissociation of DI and subsequent ionisation of the D photofragments via 2+1 REMPI at 243.16 nm. From inner to outer, the rings are assigned as: (1) DI + 270 nm $\rightarrow$ D + I*($^2P_{1/2}$) ($v_D = 7242$ m/s), (2) DI + 243 nm $\rightarrow$ D + I*($^2P_{1/2}$) ($v_D = 10184$ m/s), (3) DI+270 nm $\rightarrow$ D+I($^2P_{3/2}$) ($v_D = 12032$ m/s), and (4) DI + 243 nm $\rightarrow$ D+I($^2P_{3/2}$) ($v_D = 13880$ m/s), where v_D is the measured velocity of the D atoms. Notice that the deuterium atoms correlated to the production of I* atoms (two inner rings) have completely different angular distributions to those correlated to the production of I atoms (two outer rings), which in combination with the high velocity of the photoproducts leads to their spatial separation in a few ns assuming a laser focus of several tens of μm. Note that the ions produced by 243 nm dissociation are not produced when laser detection is not used.

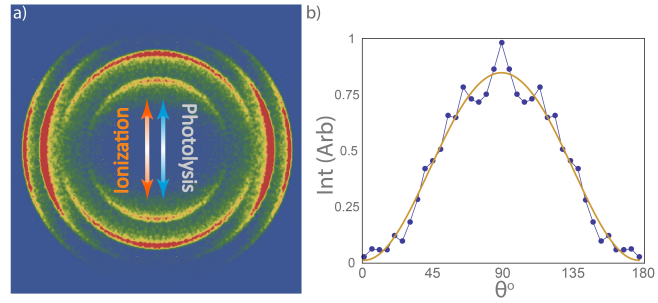

FIG. 1: a) Sliced ion image of the deuterium ions produced by the DI photodissociation. The direction of propagation of the photolysis laser is along the $90 - 270^o$ direction and opposite for the ionisation laser, while the direction of their linear polarization is marked by the arrows. b) Angular distribution of the ions corresponding to $DI + 270nm \rightarrow D + I(2P3/2)$ (points) and fit with Eq. 3 (orange line).

The angular distribution of the polarized photofragments can be expressed as an even expansion of Legendre polynomials [28–30] up to the fourth order:

$$I(\theta)/I_0 = 1 + \beta_2 P_2(cos\theta) + \beta_4 P_4(cos\theta) \quad (1)$$

where $P_n(x)$ is the nth-order Legendre polynomial. In Fig.1.b we see the angular distribution of the deuterium ions corresponding to the production of $I(^2P_{3/2})$ atoms at 270 nm, as well as a fit using Eq.1. In this case, as there is no detection sensitivity to the D-atom spin, $\beta_2 = \beta$ and $\beta_4 = 0$. The value of the spatial-anisotropy β parameter extracted by this fit is $\beta = -0.98 \pm 0.03$, corresponding to an almost purely perpendicular transition, in agreement with theoretical predictions [22].

The total intensity I_0 of the iodine photofragments, and the β_2 coefficient, describing the angular distribution, are expressed in terms of the spatial anisotropy β and a linear combination of the $a_q^{(1)}(p)$ parameters [31]:

$$I_0 = 1 + \frac{s_1}{3}\left[\left(1 - \frac{\beta}{2}\right)a_0^{(1)}(\perp) + \sqrt{2}Re[a_1^{(1)}])\right] \quad (2)$$

$$\beta_2 = \frac{1}{I_0}\left\{\frac{2s_1}{3}\left[\left(1-\frac{\beta}{2}\right)a_0^{(1)}(\perp) - \frac{\sqrt{2}}{2}Re[a_1^{(1)}])\right] - \frac{\beta}{2}\right\} \quad (3)$$

where s_1 is the sensitivity factor of the REMPI transition to the $a_q^{(1)}(p)$ parameters, given by $s_1 = -\sqrt{3}\langle G^{(1)}\rangle$ for RCP and $s_1 = +\sqrt{3}\langle G^{(1)}\rangle$ for LCP probe light, and $\langle G^{(1)}\rangle \approx 0.400$ is the time-averaged k=1 hyperfine depolarization coefficient due to the iodine nuclear spin (I = 5/2). Thus, the only way that the intensity I_0 and the β_2 can differ upon reversal of the probe (or photodissociation) laser polarization helicity, is for the iodine atoms

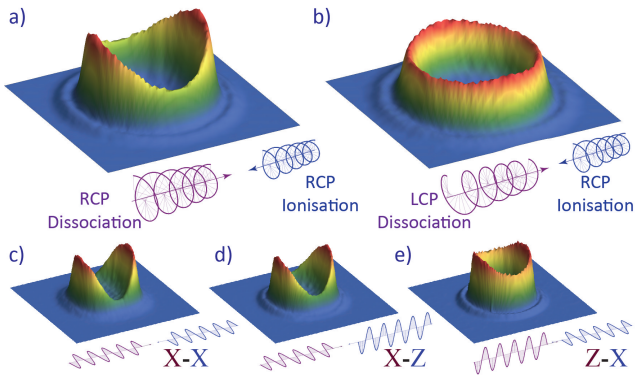

FIG. 2: a) Sliced ion image of I ions produced with both the photolysis and ionisation lasers right circularly polarized (RCP) b) Sliced ion image of I ions produced the ionisation laser RCP and the photolysis laser left circularly polarized (LCP) c) Sliced ion image with the photolysis and the ionisation lasers linearly polarized parallel to the image plane (X) d) Sliced ion image with the photolysis laser linearly polarized along X, and the ionisation laser linearly polarized perpendicular to the image plane (Z) e) Sliced ion image with the photolysis laser linearly polarized along Z, and the ionisation laser linearly polarized along X.

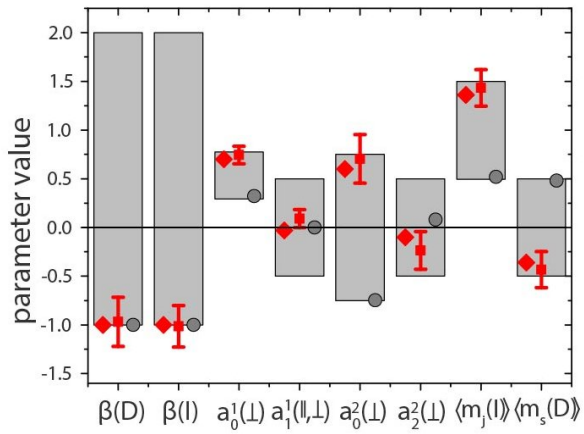

FIG. 3: Results for the parameter for the D and I($^2P_{3/2}$) atoms from the photodissociation of DI at 270 nm, and the I($^2P_{3/2}$) polarization parameters $a_q^{(k)}(p)$, which give $\langle m_j(I)\rangle \approx 1.5$ and $\langle m_s(D)\rangle \approx -0.5$. Error bars are 2σ confidence intervals, and the grey bars give the allowed range of the parameters. Theoretical predictions [23] are given for energies of 47,000 cm^{-1} (red diamonds) and 37,000 cm^{-1} (grey circles).

to be polarized (i.e. the $a_q^{(1)}(p)$ parameters are not zero). The $a_0^{(1)}(\perp)$ parameter is proportional to the j projection $\langle m_j(I)\rangle = \sqrt{j(j+1)}a_0^{(1)}(\perp)$, with j=3/2, while the $Re[a_1^{(1)}]$ parameter is related to interference from multiple dissociating states accessed by parallel and perpendicular transitions.

In Figs 2a and 2b we see two sliced ion images of iodine atoms produced by the DI+270 nm $\rightarrow D + I(^2P_{3/2})$ and detected via the $^2P_{3/2} \rightarrow\rightarrow^4 P_{1/2}$ REMPI transition at 303.6 nm. In Fig.2a, both the photolysis and the ionisation lasers are right-circularly polarized (RCP); the angular distribution is strongly anisotropic, with most of the photofragments recoiling preferentially along the propagation direction of the laser beams. For Fig.2b, the photolysis laser has opposite helicity: left-circularly polarized (LCP), and we see a very big change in the angular distribution, as it is nearly isotropic. The ratio of the total intensities of the images in Figs.3a and 3b is $I_0(RR)/I_0(LR) = 1.8 \pm 0.2$.

Figures 2c-e show images using linearly polarized photolysis and ionization laser light, aligned in the geometries (XX), (XZ), and (ZX), respectively (see Fig.2 for details). The β_2 anisotropy parameter of the corresponding geometries (determined from fitting the angular distributions using Eq. 1) can be related to the β, $a_0^{(2)}$ and $a_2^{(2)}$ parameters as:

$$\beta_2^{XX} = \frac{\beta + \frac{s_2}{7}\left(5a_0^{(2)}(\perp) - 4\sqrt{6}a_2^{(2)}(\perp)\right)}{1 - \frac{s_2}{5}\left(a_0^{(2)}(\perp) + 2\sqrt{6}a_2^{(2)}(\perp)\right)} \tag{4}$$

$$\beta_2^{XZ} = \frac{\beta + \frac{s_2}{2}\left(a_0^{(2)}(\perp) + \sqrt{6}a_2^{(2)}(\perp)\right)}{1 - \frac{s_2}{2}\left(a_0^{(2)}(\perp) + \sqrt{6}a_2^{(2)}(\perp)\right)} \tag{5}$$

$$\beta_2^{ZX} = \frac{\frac{s_2}{3}\left(3a_0^{(2)}(\perp) + \sqrt{6}a_2^{(2)}(\perp)\right)}{1 - \frac{s_2}{3}\sqrt{6}a_2^{(2)}(\perp)} \tag{6}$$

where $s_2 = (-5/4)\langle G^{(2)}\rangle$, and $\langle G^{(2)}\rangle \approx 0.233$ is the average k=2 hyperfine depolarization coefficient. Fitting images in the geometries shown in Fig.2c-e with equations 4-6 yields the $a_0^{(2)}(\perp)$ and $a_2^{(2)}(\perp)$ polarization parameters; the $a_0^{(2)}(\perp)$ gives an independent measure of $\langle m_j(I)\rangle$, as $a_0^{(2)}(\perp) = \langle\frac{3m_j(I)^2}{j(j+1)} - 1\rangle$, and $a_2^{(2)}(\perp)$ gives the interference between perpendicular transitions excited with opposite helicity.

In Fig.3 we present graphically the fitted values of the β parameter, for the D and I($^2P_{3/2}$) photofragments from the photodissociation of DI at 270 nm, as well as the $a_q^{(k)}(p)$ parameters for $I(^2P_{3/2})$, along with the corresponding values of $\langle m_j(I)\rangle$ and the inferred D-atom electron spin-projection $\langle m_s(D)\rangle = 1 - \langle m_j(I)\rangle$. The gray histograms represent the physical ranges of these parameters. The value of each of the $a_0^{(1)}(\perp)$ and $a_0^{(2)}(\perp)$ parameters is maximal, meaning that $\langle m_j(I)\rangle = 1.5$ is also maximal, constraining the D photofragment electron spin polarization to be maximally polarized in the opposite direction, $\langle m_s(D)\rangle = -0.5$ [22], as shown in Fig. 4. These m-state values are explained by excitation of the $A^1\Pi_1$

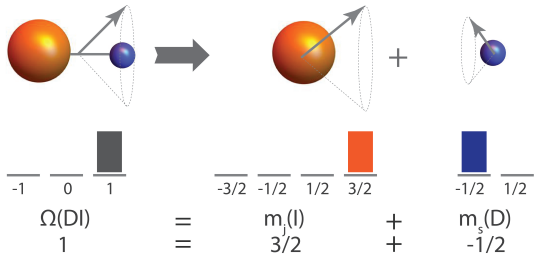

FIG. 4: Angular momentum projection of Ω=+1 is prepared for the DI molecules from the circularly polarized photolysis beam, and is distributed to the angular momentum projections of the photofragments after

state at 270 nm, followed by adiabatic dissociation:

$$DI(\Omega_A = \pm 1) \rightarrow D(m_s = \mp 1/2) + I(m_j = \pm 3/2) \quad (7)$$

The measured β and polarization parameters are consistent with those of the dissociation mechanism predicted at a significantly higher energy, $\sim 47,000\, cm^{-1}$ [22]. However, at lower energies, the dissociation is predicted to switch to excitation and adiabatic dissociation via the $a^3\Pi_1$ state, producing $m_j(I) = +1/2$ and $m_s(D) = +1/2$ [22]; the energy of this mechanism switch is strongly model dependent. Our measurements here at $\sim 37,000\, cm^{-1}$ do not observe this mechanism switch, indicating that the dissociation models may need to be modified.

We note that Eq. 7 applies exactly only for photofragment recoil direction $\hat{v}$ parallel to the photolysis polarization direction $\hat{k}$; the photofragment polarization falls as $\hat{v} \cdot \hat{k} = \cos\theta_{vk}$. This loss in polarization can be minimized by preferentially aligning the HX bonds along $\hat{k}$ just before photodissociation, using nonresonant molecular alignment with a strong laser pulse [32–34].

The photodissociation process initially polarizes the electron spin S leaving the nuclear spin I initially unpolarized. The D atoms are found in a coherent superposition of the total angular momentum states $|F, M_F\rangle$, defined by the coupling F= S + I, which are the eigenstates of the system. Therefore, the system evolves in time, transferring the polarization of the electron spin to the nuclear spin, and back [35]. Such a polarization transfer has been experimentally demonstrated in several cases [36, 37]. Here, the polarization transfer can be quantified [38] using Eqs. 3-6 in Ref. [39], giving:

$$m_s(D) = \frac{16}{27} sin^2(\frac{\Delta E}{2\hbar} t) \quad (8a)$$

$$m_j(I) = \frac{1}{2} - \frac{16}{27} sin^2(\frac{\Delta E}{2\hbar} t) \quad (8b)$$

where $\Delta E = 327.37 MHz$ is the hyperfine splitting in the deuterium atom [40]. We show the polarization dependence of the D electron and nuclear spin, by plotting Eqs. 8a and 8b in Fig.5. At t=0, the electron spin is fully polarized, and the nuclear spin is unpolarized. The electron spin polarization is transferred to the nuclear spin and back, with a period of ∼3.2 ns. An interesting aspect of these dynamics is that there exist times (for example around 1.6 and 4.8 ns) where the electron spin polarization is opposite to the initial one, albeit with a much smaller value. At the same times, the spin projection of the D nucleus reaches a value of 60%.

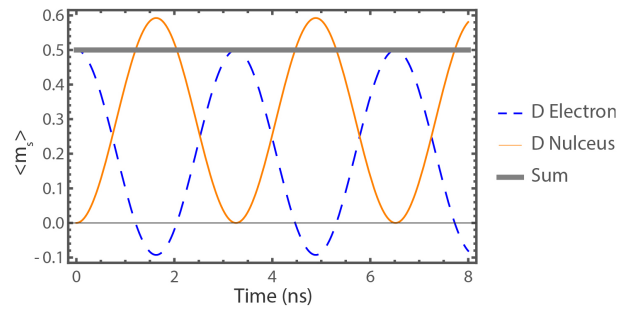

FIG. 5: Evolution of the spin projection expectation values of the electron (dashed line), the nucleus (thin solid line) and sum (thick solid line) due to the hyperfine interaction.

The main depolarizer of the D atoms will be the halogen-atom cofragment, here $I(^2P_{3/2})$. Thermal spin-exchange rates of H/D with halogen atoms are not available, but are of order $10^{-9} cm^3 s^{-1}$ for collisions with alkali atoms [41]. Using this rate, maximal densities of $\sim 10^{18} cm^{-3}$ of spin-polarized D atoms can be produced over the needed time of 1 ns. However, for the photodissociation of DF near 193 nm, it is predicted that both the D and the F($^2P_{3/2}$) cofragment will have the same polarization: $\langle m_s(D)\rangle = \langle m_j(F)\rangle = 0.5$; there is even the possibility of polarizing the F($^2P_{3/2}$) further via infrared excitation of the DF before photodissociation [35–39]. As all colliding species will have similar polarizations, the depolarization rate of D atoms should be significantly reduced, and perhaps densities of greater than $\sim 10^{18}\, cm^{-3}$ spin-polarized D atoms can be produced.

Calculations using modified MEDUSA code [42] have shown that the irradiation of $10^{18}\, cm^{-3}$ spin-polarized D atoms with a 6 kJ (with $\lambda \sim 1\, \mu m$), 1 ps laser pulse [43, 44], focused to $10\, \mu m$, will heat the resulting ions to average collision (thermal) energies of ∼10 keV, producing ∼100 neutrons/pulse from D-D fusion reactions. Past experiments have demonstrated a neutron production in excess of 10^6 per pulse using a 62 J, 1 ps laser pulse, focused to $20\, \mu m$, and D_2 gas densities of up to $\sim 10^{20}\, cm^{-3}$ [45]. These results show that the study of D-D fusion with high signals is possible, using high-density polarized D atoms and laser-initiated fusion.

The experimental work was conducted at the Ultraviolet Laser Facility at FORTH-IESL, supported in part by the EC H2020 project LASERLAB-EUROPE (Grant Agreement No. 654148), and the European Research Council (ERC) Grant TRICEPS (GA No. 207542).

* Current address: Johannes Gutenberg-Universitat Mainz, 55128 Mainz, Germany

[1] G. Ciullo, *Polarized Fusion: An Idea More Than Thirty Years Old! What Are We Waiting For?* (Springer International Publishing, Cham, 2016).
[2] R. Engels, K. Grigoryev, L. Kochenda, P. Kravtsov, M. Mikirtytchiants, F. Rathmann, H. Paetz gen. Schieck, H. Ströher, V. Trofimov, A. Vasilyev, et al., Physics of Particles and Nuclei **45**, 341 (2014).
[3] G. Ciullo, R. Engels, M. Bscher, and A. Vasilyev, *Nuclear Fusion with Polarized Fuel* (Springer, 2016).
[4] C. Leemann, H. Brgisser, P. Huber, U. Rohrer, H. P. gen Schieck, and F. Seiler, Ann. of Phys. **66**, 810 (1971).
[5] K. A. Fletcher, Z. Ayer, T. C. Black, R. K. Das, H. J. Karwowski, E. J. Ludwig, and G. M. Hale, Phys. Rev. C **49**, 2305 (1994).
[6] G. Hale and G. Doolen, LA-9971-MS (1984).
[7] H. M. Hofmann and D. Fick, Phys. Rev. Lett. **52**, 2038 (1984).
[8] S. Lemaitre and H. Paetz gen. Schieck, Annalen der Physik **505**, 503 (1993), ISSN 1521-3889.
[9] J. S. Zhang, K. F. Liu, and G. W. Shuy, Phys. Rev. Lett. **57**, 1410 (1986).
[10] J. S. Zhang, K. F. Liu, and G. W. Shuy, Phys. Rev. C **60**, 054614 (1999).
[11] R. Engels, M. Gaißer, R. Gorski, K. Grigoryev, M. Mikirtychyants, A. Nass, F. Rathmann, H. Seyfarth, H. Ströher, P. Weiss, et al., Phys. Rev. Lett. **115**, 113007 (2015).
[12] H. Paetz gen. Schieck, Eur. Phys. J. A **44**, 321 (2010).
[13] M. Iio, I. Daito, N. Doshita, T. Hasegawa, N. Horikawa, T. Inagaki, S. Ishii, T. Iwata, T. Kobayashi, K. Kondo, et al., Nuc. Instr. Meth. Phys. Res. A **526**, 190 (2004).
[14] T. P. Rakitzis, P. C. Samartzis, R. L. Toomes, T. N. Kitsopoulos, A. Brown, G. G. Balint-Kurti, O. S. Vasyutinskii, and J. A. Beswick, Science **300**, 1936 (2003).
[15] T. P. Rakitzis, P. C. Samartzis, R. L. Toomes, and T. N. Kitsopoulos, J. Chem. Phys. **121** (2004).
[16] D. Sofikitis, L. Rubio-Lago, L. Bougas, A. J. Alexander, and T. P. Rakitzis, J. Chem. Phys. **129**, 144302 (2008).
[17] D. Sofikitis, L. Rubio-Lago, A. J. Alexander, and T. P. Rakitzis, EPL **81**, 68002 (2008).
[18] R. J. Van Brunt and R. N. Zare, J. Chem. Phys. **48** (1968).
[19] G. G. Balint-Kurti, A. J. Orr-Ewing, J. A. Beswick, A. Brown, and O. S. Vasyutinskii, J. Chem. Phys. **116** (2002).
[20] A. Brown, G. G. Balint-Kurti, and O. S. Vasyutinskii, J. Phys. Chem. A **108**, 7790 (2004).
[21] A. G. Smolin, O. S. Vasyutinskii, G. G. Balint-Kurti, and A. Brown, J. Phys. Chem. A **110**, 5371 (2006).
[22] A. Brown, J. Chem. Phys. **122** (2005).
[23] B. M. Broderick, Y. Lee, M. B. Doyle, V. Y. Chernyak, O. S. Vasyutinskii, and A. G. Suits, Rev. Sci. Instrum. **85**, 053103 (2014).
[24] L. Bougas, D. Sofikitis, M. A. Everest, A. J. Alexander, and T. P. Rakitzis, J. Phys. Chem. **133**, 174308 (2010).
[25] C. R. Gebhardt, T. P. Rakitzis, P. C. Samartzis, V. Ladopoulos, and T. N. Kitsopoulos, Rev. Sci. Instrum. **72** (2001).
[26] V. Papadakis and T. N. Kitsopoulos, Rev. Sci. Instrum. **77**, 083101 (2006).
[27] A. T. J. B. Eppink and D. H. Parker, Rev. Sci. Instrum **68** (1997).
[28] S. E. Choi and R. B. Bernstein, J. Chem. Phys. **85** (1986).
[29] R. N. Zare and D. R. Herschbach, Proceedings of the IEEE **51**, 173 (1963), ISSN 0018-9219.
[30] L. D. A. Siebbeles, M. GlassMaujean, O. S. Vasyutinskii, J. A. Beswick, and O. Roncero, J. Chem. Phys. **100** (1994).
[31] J. Zhang, M. Dulligan, and C. Wittig, J. Chem. Phys. **107** (1997).
[32] B. Friedrich and D. Herschbach, Phys. Rev. Lett. **74**, 4623 (1995).
[33] H. Stapelfeldt and T. Seideman, Rev. Mod. Phys. **75**, 543 (2003).
[34] Chemical Physics Letters **271**, 209 (1997), ISSN 0009-2614.
[35] R. Altkorn, R. N. Zare, and C. H. Greene, Mol. Phys. **55** (1985).
[36] D. Sofikitis, L. Rubio-Lago, M. R. Martin, D. J. A. Brown, N. C.-M. Bartlett, R. N. Zare, and T. P. Rakitzis, Phys. Rev. A **76**, 012503 (2007).
[37] N. C.-M. Bartlett, D. J. Miller, R. N. Zare, A. J. Alexander, D. Sofkitis, and T. P. Rakitzis, Phys. Chem. Chem. Phys. **11**, 142 (2009).
[38] L. Rubio-Lago, D. Sofikitis, A. Koubenakis, and T. P. Rakitzis, Phys. Rev. A **74**, 042503 (2006).
[39] T. P. Rakitzis, Phys. Rev. Lett. **94**, 083005 (2005).
[40] J. E. Nafe, E. B. Nelson, and I. I. Rabi, Phys. Rev. **71**, 914 (1947).
[41] L. Anderson and T. Walker, Nuc. Instr. Meth. Phys. Res. A **357**, 220 (1995), ISSN 0168-9002.
[42] J. Christiansen, D. Ashby, and K. Roberts, Comp. Phys. Comm. **7**, 271 (1974), ISSN 0010-4655.
[43] J. Ayers, B. Felker, V. Smalyuk, N. Izumi, K. Piston, J. Holder, G. Power, F. Allen, N. Simanovska, P. Bell, et al. (2012).
[44] C. Haefner, Presentation to ELI-NP Workshop, Bucharest, Romania (2011).
[45] S. Fritzler, Z. Najmudin, V. Malka, K. Krushelnick, C. Marle, B. Walton, M. S. Wei, R. J. Clarke, and A. E. Dangor, Phys. Rev. Lett. **89**, 165004 (2002).

PCCP

PAPER

View Article Online
View Journal | View Issue

Check for updates

Cite this: *Phys. Chem. Chem. Phys.*, 2018, **20**, 17423

Multiphoton Rydberg and valence dynamics of CH_3Br probed by mass spectrometry and slice imaging†

Arnar Hafliðason,[a] Pavle Glodic,[b] Greta Koumarianou,[b] Peter C. Samartzis *[b] and Ágúst Kvaran *[a]

Received 12th April 2018,
Accepted 6th June 2018

DOI: 10.1039/c8cp02350f

rsc.li/pccp

The multiphoton dynamics of CH_3Br were probed by Mass Resolved MultiPhoton Ionization (MR-MPI), Slice Imaging and Photoelectron Imaging in the two-photon excitation region of 66 000 to 80 000 cm^{-1}. Slice images of the CH_3^+ and Br^+ photoproducts of ten two-photon resonant transitions to np and nd Rydberg states of the parent molecule were recorded. CH_3^+ ions dominate the mass spectra. Kinetic energy release spectra (KERs) were derived from slice and photoelectron images and anisotropy parameters were extracted from the angular distributions of the ions to identify the processes and the dynamics involved. At all wavelengths we observe three-photon excitations, *via* the two-photon resonant transitions to molecular Rydberg states, forming metastable, superexcited ($CH_3Br^{\#}$) states which dissociate to form CH_3 Rydberg states (CH_3**) along with Br/Br*. A correlation between the parent Rydberg states excited and CH_3** formed is evident. For the three highest excitation energies used, the $CH_3Br^{\#}$ metastable states also generate high kinetic energy fragments of CH_3(X) and Br/Br*. In addition for two out of these three wavelengths we also measure one-photon photolysis of CH_3Br in the A band forming CH_3(X) in various vibrational modes and bromine atoms in the ground (Br) and spin–orbit excited (Br*) states.

I. Introduction

The methyl halides play an important role in the chemistry of the atmosphere.[1–4] Although far less abundant than methyl chloride in the stratosphere, methyl bromide is found to be much more efficient in ozone depletion.[4] Furthermore, bromocarbons are known to have a high global warming potential.[5] This has triggered a considerable interest in the spectroscopy[3,6–11] and photofragmentation dynamics[11–19] of methyl bromide over the last few decades. Additionally, the molecule is a simple prototype of a halogen-containing organic molecule for fundamental studies of photodissociation and photoionization involving formation of the cornerstone fragment CH_3.[15,18,20]

Photofragmentation studies of methyl bromide can be classified into two groups. One group focuses on the characterization of photofragments CH_3 + $Br(^2P_{3/2})$/$Br^*(^2P_{1/2})$ resulting from photodissociation in the A band[13–15,18,21–23] whereas the other group concerns the involvement of higher energy Rydberg and ion-pair states ("the Rydberg state region").[11,16,17,19,20] In the first group, single-wavelength excitation studies (193 and 222 nm,[12,23] 205 nm,[13] 213 and 230 nm,[15,24] and 216 nm[15]) as well as wavelength range excitations (215–251 nm[14] and 240–280 nm[22]) have been performed by the use of time-of-flight[12,22] and imaging[13–15,23,24] techniques. In the second group the emphasis has been on the involvement of Rydberg and ion-pair states in photodissociation processes to form ion pairs.[11,16,17,20] Photoionization studies are focused on the lowest energies of the ion and its breakdown.[11,25,26] Multiphoton dissociation studies focus on excitations to the lowest Rydberg states (5s) of the molecule.[19] The energetics of methyl bromide (CH_3Br) in the Rydberg state region have been studied quite thoroughly to map the Rydberg state structure of the molecule both by absorption spectroscopy[7] and by Resonance Enhanced MultiPhoton Ionization (REMPI),[11,20] as well as theoretically.[27]

Recently we have been exploring the effect of state interactions within the Rydberg state region on photofragmentation processes for the hydrogen halides.[28–33] These studies have revealed effect of Rydberg to valence as well as Rydberg to Rydberg state interactions on both the photodissociation and photoionization mechanisms within the molecules on a rotational and vibrational

[a] *Science Institute, University of Iceland, Dunhagi 3, 107 Reykjavík, Iceland. E-mail: agust@hi.is, arnahaf@hi.is; Fax: +354-552-8911; Tel: +354-525-4800*
[b] *Institute of Electronic Structure and Laser, Foundation for Research and Technology-Hellas, Vassilika Vouton, 71110 Heraklion, Greece. E-mail: sama@iesl.forth.gr, glodic_pavle@yahoo.com, gr.koumarianou@gmail.com; Fax: +30-2810-391305; Tel: +30-2810-391467*

† Electronic supplementary information (ESI) available. See DOI: 10.1039/c8cp02350f

energy level basis. We now expand this approach to polyatomic molecules, starting with methyl bromide (CH_3Br). In this paper we present (1) Mass-Resolved MultiPhoton Ionization (MR-MPI) for both Resonance Enhanced MPI (REMPI) and Non-Resonant MPI, (2) slice imaging and (3) photoelectron imaging data for excitation of CH_3Br involving two-photon resonant excitation to np and nd Rydberg states of the molecule for the two-photon wavenumber region of 66 000–80 000 cm^{-1} by a one-color excitation scheme. Despite the use of two-photon resonances, three-photon excitations followed by dissociations to form Rydberg states of CH_3 are found to dominate the dynamics. For the three highest energy excitations an additional three-photon channel opens, generating translationally hot $CH_3(X)$ and Br/Br* and for two of these three excitations one-photon processes are also observed. These results are discussed in view of previous work on the low and high energy excited state dynamics of CH_3Br.

II. Experimental

The Velocity Map Imaging (VMI)/Slicing setup used in this work has been described in detail before.[34,35] Hence, only a brief description will be given here. A supersonic molecular beam, typically a mixture of 20% CH_3Br in He, was formed by expansion through a home-made piezoelectrically-actuated nozzle valve (∅ 1 mm orifice) and skimmed (∅ 1.5 mm, Beam Dynamics) prior to entering the interaction region of a slice imaging setup. A stagnation pressure of $P_0 \sim 1$ bar was used. A photolysis/photofragment ionization laser beam was focused (f = 30 cm) on the geometric focal point of a single-electrode repeller-extractor plate arrangement where it intersected the collimated molecular beam at right angles. The laser beam (typically 1.5 mJ per pulse) was generated by a pulsed Nd^{3+}:YAG laser (Spectra Physics Quanta Ray Pro 250) pumping a master oscillator–power oscillator system (Spectra Physics MOPO 730-10) set at the appropriate wavelength.

For the slicing experiments, reported here, the repeller is pulsed ON at the appropriate time delay (~300 ns) following the photolysis/ionization. The charged photofragments traverse a field-free time-of-flight region (45 cm) and a gated, position-sensitive detector (dual, imaging-quality Micro-Channel Plates (MCP) array coupled to a phosphor screen) images the center slice of the photofragment sphere. The image frame is recorded asynchronously every second (~10 laser shots) by a Charge-Coupled Device (CCD) camera and several thousand frames are averaged to form images. Each final image is integrated from its center over angle to extract the speed and over radius to extract the angular distributions of the corresponding fragments. For photoelectrons, the repeller is negatively charged and both the repeller electrode and the detector are not gated (*i.e.* they are always ON).

III. Results and analysis

A. Mass resolved MPI

(2 + m) as well as (3 + m) REMPI spectra (where 2 and 3 refer to the number of photons for resonant excitation to CH_3Br Rydberg states and m refers to the number of additional photons needed to generate the observed ions) and spectral assignments for CH_3Br have been reported in ref. 20 and 11. The (2 + m) REMPI spectrum for CH_3^+ ion detection from ref. 11 for the two-photon resonant excitation region of 66 000–80 000 cm^{-1} is reproduced in Fig. 1 along with mass spectra for selected molecular Rydberg state resonances normalized to the CH_3^+ signal intensity. All the mass spectra show the CH_3^+ ion mass signal ($I(CH_3^+)$) to be the strongest and the signal intensities to vary as, $CH_3^+ > CH_2^+ > CH^+ > (Br^+, CBr^+)$. The relative ion intensities, $I(M^+)/I(CH_3^+)$, for $M^+ = CH_2^+$, CH^+ and Br^+ are found to vary with wavenumber and to reach maxima as the wavenumber values get closer to the ion-pair threshold ($CH_3^+ + Br^-$; Fig. 1b). Closer inspection of the REMPI spectra shows that these have two major contributions, an underlying continuum, gradually increasing with excitation wavenumber and superimposed REMPI peaks. The latter are due to transitions to discrete quantum levels and, therefore, by definition, involve resonant transitions (*i.e.* REMPI). They correspond to two-photon resonant transitions to the parent

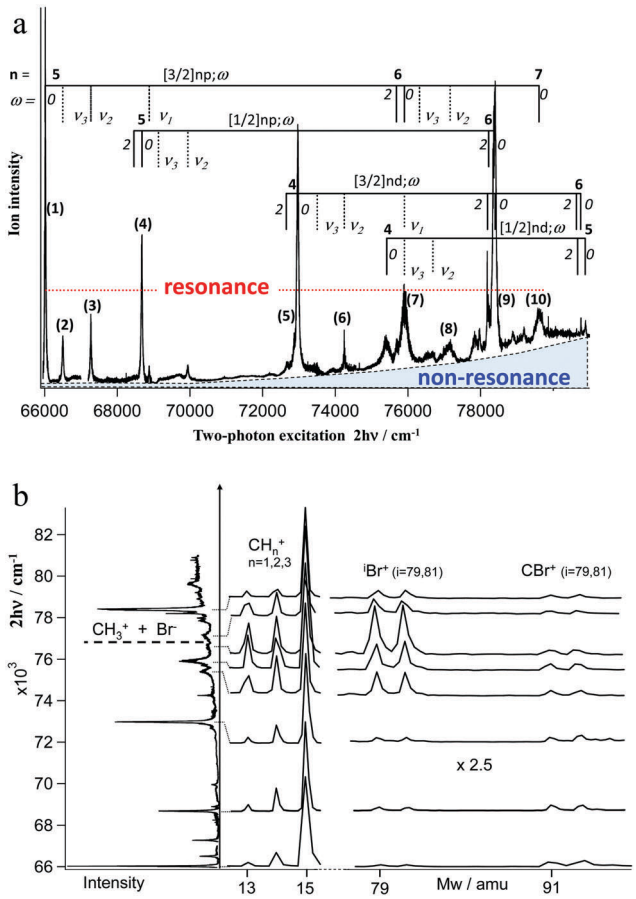

Fig. 1 Mass Resolved (MR) MPI for CH_3Br: (a) CH_3^+ signal (MPI spectrum) for the two-photon wavenumber range of 66 000–80 000 cm^{-1} and CH_3Br Rydberg state (CH_3Br^{**}) assignments. Separation of the spectrum into resonant and non-resonant contributions is indicated. The numbers of slice images recorded are indicated (see Table 1). (b) Mass spectra of selected CH_3Br Rydberg state resonances. Signals for masses larger than 78 amu have been expanded by a factor of 2.5.

molecular Rydberg states as an initial excitation[11,20] prior to further excitation/dissociation/ionization processes (*i.e.* (2 + *m*) REMPI). The continuum, on the other hand, involves transitions to non-quantized energy levels, *i.e.* non-resonant transitions (Fig. 1a), of which initial one-photon transitions to repulsive molecular valence states are the most likely.[14,15,22] Such transitions are followed by dissociation (*i.e.* one-photon photodissociation) to form CH_3 in the ground electronic state (X) and bromine atoms in their ground ($Br(^2P_{3/2})$, henceforth denoted Br) or spin–orbit excited ($Br(^2P_{1/2})$, henceforth denoted Br*) states, which are subsequently ionized by (non-resonant) multiphoton ionization (MPI). From now on these two contributions will be referred to as resonant and non-resonant contributions to the MPI spectrum, respectively.

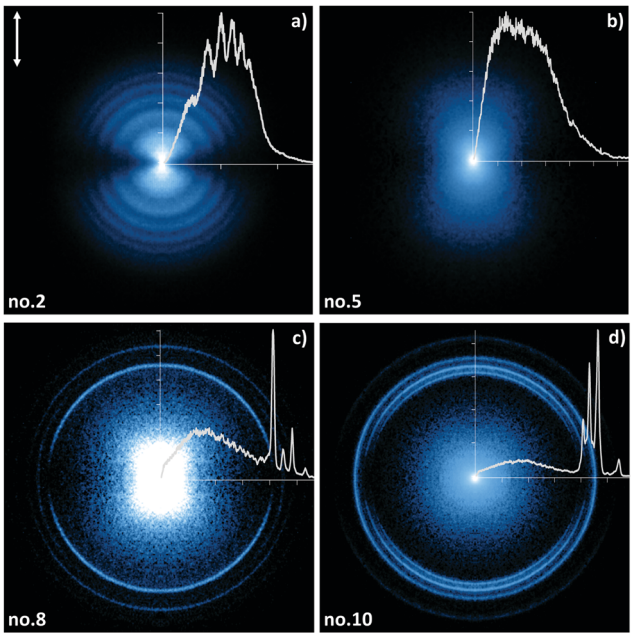

Fig. 2 CH_3^+ slice images and the corresponding kinetic energy release spectra (KERs) for excitation numbers 2 (a), 5 (b), 8 (c) and 10 (d) (see Table 1). The image intensity scale has been adjusted to show all major features. The KERs are normalized to the strongest peak in each spectrum. The laser polarization is indicated by the double arrow in panel (a).

B. Slice images and kinetic energy release spectra (KERs)

CH_3^+. CH_3^+ ion slice images (Fig. 2) were recorded for MPI of CH_3Br corresponding to (2 + *m*) REMPI for resonant excitation to a total of ten molecular Rydberg states (with np and nd Rydberg electron configurations and different vibrational states), converging to both spin–orbit components of the ground ionic states $X(^2\Pi_{3/2})$ and $X^*(^2\Pi_{1/2})$ in the two-photon excitation region of 66 000–80 000 cm^{-1} (see Table 1). Kinetic energy release spectra (KERs) were derived from the images (see Fig. 3). Two major spectral components could be identified from the images/KERs corresponding to the non-resonant and resonant contributions mentioned above. Large non-resonant contributions are observed at two of the highest energy two-photon resonant excitations only (77 165 cm^{-1} and 79 610 cm^{-1}; transitions no. 8 and 10 in Table 1). The non-resonant MPI spectral contributions (see Fig. 1a) appear as clear rings in the images/sharp peaks in the KERs (Fig. 2 and 3) as to be expected for direct non-resonant photodissociation processes (see further discussion in Section IV.B). Very small non-resonant spectral contributions were also observed for the excitations 75 905 cm^{-1} (7) and 78 370/78 401 cm^{-1} (9). The MPI spectral contributions (Fig. 1a) due to the resonant transitions are observed for all the data as broad "underlying" KER spectral structures peaking at low KER as to be expected for resonance excitations followed by delayed dissociation processes (see further discussion in Section IV.A. Vibrational structure is exhibited for the lowest four energy excitations (66 019–68 684 cm^{-1}) (Fig. 3).

The non-resonant contributions observed can be assigned to the stepwise processes,

$$CH_3Br + 1h\nu \rightarrow CH_3Br^*; \quad \text{non-resonant transition} \quad (1a)$$

$$CH_3Br^* \rightarrow CH_3(X;\ \nu_1\nu_2\nu_3\nu_4) + Br/Br^*; \quad \text{dissociation} \quad (1b)$$

$$CH_3(X;\ \nu_1\nu_2\nu_3\nu_4) + 3h\nu \rightarrow CH_3^+ + e^-; \quad \text{photoionization} \quad (1c)$$

where $CH_3(X;\ \nu_1\nu_2\nu_3\nu_4)$ refers to the ground electronic state of $CH_3(X)$ and vibrational levels ν_1,ν_2,ν_3,ν_4 and Br/Br* refer to the ground (Br) and spin–orbit excited (Br*) states of bromine, respectively. Since the kinetic energy release by the CH_3^+ ions

Table 1 Velocity map images for CH_3^+ and Br^+ and the corresponding photoelectron images recorded for (2 + *m*) REMPI of CH_3Br *via* resonant excitation to specified molecular Rydberg states

Image no.	CH_3Br Rydberg states; $[\Omega_c]nl$; $\omega,(\nu_1\nu_2\nu_3)^a$	One-photon excitation/nm	Two-photon excitation/cm^{-1}	CH_3 Rydberg states detected
1	[3/2]5p; 0, (000)	302.943	66 019[c]	3p; $^2A_2$
2	[3/2]5p; 0, (001)	300.738	66 503[d]	3p; $^2A_2$
3	[3/2]5p; 0, (010)	297.287	67 275[d]	3p; $^2A_2$
4	[1/2]5p; 0, (000)	291.188	68 684[c]	3p; $^2A_2$
5	[3/2]4d; 0, (000)	274.059	72 977[c]	3d; $^2E/^2A_1$
6	[3/2]4d; 0, (010)	269.364	74 249[d]	3d; $^2E/^2A_1$
7	[3/2]6p; 0, (000)/[3/2]4d; 0, (100)/[1/2]4d; 0, (001)[b]	263.487	75 905[c]	4p; $^2A_2$, 3d; $^2E/^2A_1$
8	[3/2]6p; 0, (010)[b]	259.185	77 165[d]	4p; $^2A_2$, 3d; $^2E/^2A_1$
9	[1/2]6p; 0, (000)/[3/2]5d; 0, (000)	255.199, 255.099	78 370[c], 78 401[c]	4p; $^2A_2$, 3d; $^2E/^2A_1$, 4f; 2E
10	[3/2]7p; 0, (000)	251.225	79 610[c]	4p; $^2A_2$, 3d; $^2E/^2A_1$

[a] $[\Omega_c]$: total angular momentum quantum number for the core ion. *n*: principal quantum number for the Rydberg electron. *l*: Rydberg electron orbital (p,d). ω: total angular momentum quantum number for the Rydberg electron. (ν_1, ν_2, ν_3): vibrational quantum numbers referring to vibrational modes, ν_1 (symmetric stretch), ν_2 (umbrella) and ν_3 (C–Br stretch). [b] Spectral overlap. [c] Ref. 20. [d] Ref. 11.

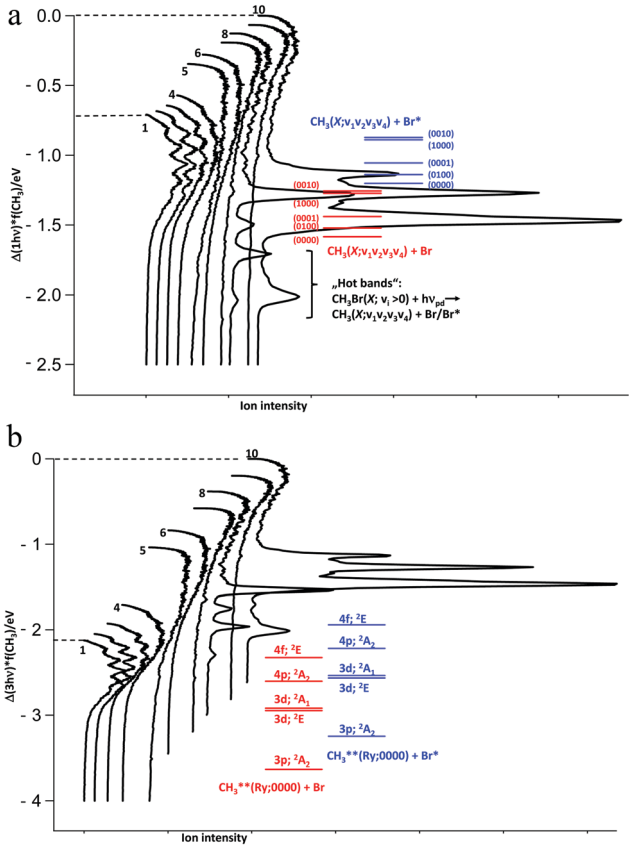

Fig. 3 CH_3^+ kinetic energy release spectra (KERs) derived from images no. 1–10 (see Table 1 and Fig. 1a). The spectra are normalized to the height of the lowest KER spectra contributions, corresponding to resonant contributions (see main text) in each spectrum. The spectra are plotted as a function of a relative scale $\Delta(1h\nu)*f(CH_3)$ (a) and $\Delta(3h\nu)*f(CH_3)$ (for $CH_3^{79}Br$) (b) (see explanation in main text) and tilted to the right (*i.e.* plotted vertically). Common energy thresholds (energy maxima) for the formation of $CH_3(X, \nu_1\nu_2\nu_3\nu_4)$ + Br/Br* after non-resonant one-photon photodissociation of CH_3Br are indicated in (a). Common energy thresholds (energy maxima) for the formation of $CH_3^{**}(Ry, \nu_1\nu_2\nu_3\nu_4)$ + Br/Br* after three-photon photodissociation of CH_3Br *via* resonant excitation to CH_3Br Rydberg states are indicated in (b).

formed is determined by the initial step (1a) it is convenient to compare the corresponding KERs contributions on a relative one-photon energy scale ($\Delta(1h\nu) = 1h\nu_i - 1h\nu_0$, where ν_0 and ν_i are one-photon excitation frequencies of a reference spectrum (ν_0) and a spectrum i (ν_i) for $\nu_0 > \nu_i$) weighted by the mass ratio factor for CH_3, $f(CH_3) = m(^jBr)/m(CH_3{}^jBr)$ (j = 79, 81), to take account of the conservation of momentum. Thus, spectral peaks due to the formation of the same species/thresholds, $CH_3(X; \nu_1\nu_2\nu_3\nu_4)$ + Br/Br*, will match. This has been carried out in Fig. 3a, which shows the KERs shifted by the weighted one-photon energy difference ($\Delta(1h\nu)*f(CH_3)$) where the "zero kinetic energy released" for the two-photon excitation to the [3/2]7p; 0, (000) CH_3Br Rydberg state (image/KER no. 10/79 610 cm^{-1}; see Table 1) has been set to zero (reference spectrum). Thresholds corresponding to the "maximum possible kinetic energy released" for formation of the various $CH_3(X; \nu_1\nu_2\nu_3\nu_4)$ species (along with Br/Br*) are also marked in Fig. 3a. All sharp peaks observed in spectrum no. 8/77 165 cm^{-1} are found to match peaks in no. 10/79 610 cm^{-1}. Some overlap of the peaks is observed in spectrum no. 10/79 610 cm^{-1}. The peaks observed in the region of $\Delta(1h\nu)*f(CH_3)$ = −1.6 to 0.0 eV are due to excitations of $CH_3Br(X)$ in its ground vibrational state, whereas those of $\Delta(1h\nu)*f(CH_3) < -1.6$ eV are due to excitations of vibrationally excited $CH_3Br(X)$ molecules ("hot bands"). We assign the peaks at about $\Delta(1h\nu)*f(CH_3)$ = −1.49 eV (Fig. 3a), both in spectra no. 8 and 10 and at about $\Delta(1h\nu)*f(CH_3)$ = −1.13 eV in no. 10 to the formation of a vibrationally excited $CH_3(X)$ in the out-of-plane bending (umbrella) mode (ν_2 = 1), *i.e.* $CH_3(X; 0100)$ along with Br and Br*, respectively. The peaks at about $\Delta(1h\nu)*f(CH_3)$ = −1.27 eV (Fig. 3a), both in spectra no. 8 and 10 are due to the formation of a vibrationally excited $CH_3(X)$ in stretching modes (ν_1 = 1 and/or ν_3 = 1), *i.e.* $CH_3(X; 1000)$ and/or $CH_3(X; 0010)$, along with Br.

Comparison of the KERs of the resonant contributions as well as analysis of the corresponding photoelectron spectra (PES, see below) reveals that the kinetic energy released by the CH_3^+ ions is determined by a dissociation after an initial three-photon excitation step. Therefore, in Fig. 3b, the corresponding KER spectra are compared on a weighted relative three-photon energy scale ($\Delta(3h\nu)*f(CH_3)$; $\Delta(3h\nu) = 3h\nu_i - 3h\nu_0$). Furthermore, analysis of the PES (see below) suggests that electrons are released by one-photon ionization of Rydberg states of CH_3 (CH_3^{**}). We, therefore, propose that the overall excitation process involves formation of CH_3^{**} along with Br/Br* by three-photon photodissociation (two photons to an intermediate Rydberg state (see Table 1) plus one additional photon to reach one or more "superexcited" repulsive state denoted here as $CH_3Br^{\#}$) followed by one-photon ionization of CH_3^{**} to form CH_3^+ as follows,

$$CH_3Br + 2h\nu \rightarrow CH_3Br^{**}(Ry; \nu_1\nu_2\nu_3); \quad \text{resonant transition} \quad (2a)$$

$$CH_3Br^{**}(Ry; \nu_1\nu_2\nu_3) + 1h\nu \rightarrow CH_3Br^{\#}; \quad \text{photoexcitation} \quad (2b)$$

$$CH_3Br^{\#} \rightarrow CH_3^{**} + Br/Br^*; \quad \text{dissociation} \quad (2c)$$

$$CH_3^{**} + 1h\nu \rightarrow CH_3^+ + e^-; \quad \text{photoionization} \quad (2d)$$

where $CH_3Br^{**}(Ry; \nu_1\nu_2\nu_3)$ represents vibrational levels ν_1, ν_2, ν_3 of a parent molecular Rydberg state and $CH_3Br^{\#}$ represents one or more superexcited state.

The vibrational structure with a progression frequency corresponding to about 1300 cm^{-1} observed for the lowest excitation KERs (no. 1–4; Fig. 3) resembles that to be expected for transitions to vibrational levels of a CH_3^{**} Rydberg state of an out of plane/umbrella mode.[36,37] The position of the thresholds for $CH_3^{**}(3p^2A_2)$ + Br/Br* formation following the three-photon excitation process (Fig. 3b; see also text above) in the tail of the KER spectra on the high energy side of the vibrational structure, as well as analysis of the corresponding photoelectron spectra (see below) suggests that the vibrational structure corresponds to the formation of $CH_3^{**}(3p^2A_2; \nu_1\nu_2\nu_3\nu_4)$ for varying quantum levels of the out-of-plane bending mode (ν_2). Structure analysis of the four lowest excitation energy KER

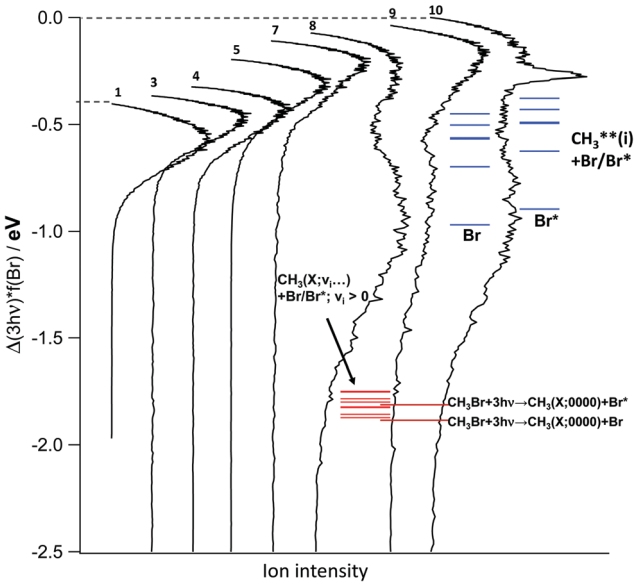

Fig. 4 Br^+ kinetic energy release spectra (KERs) derived from images no. 1, 3–5, and 7–10 (see Table 1 and Fig. 1a). The spectra are normalized to the height of the lowest KER spectra contributions, corresponding to resonant contributions (see main text) in each spectrum. The spectra are plotted as a function of a relative scale $\Delta(3h\nu)*f$(Br) (for $CH_3{}^{79}Br$) (see explanation in main text of Section IV) and tilted to the right (*i.e.* plotted vertically). Common energy thresholds for the formation of CH_3**(Ry, $\nu_1\nu_2\nu_3\nu_4$) + Br/Br* as well as CH_3(X, $\nu_1\nu_2\nu_3\nu_4$) + Br/Br* after three-photon photodissociation of CH_3Br *via* resonant excitation to CH_3Br Rydberg states are indicated.

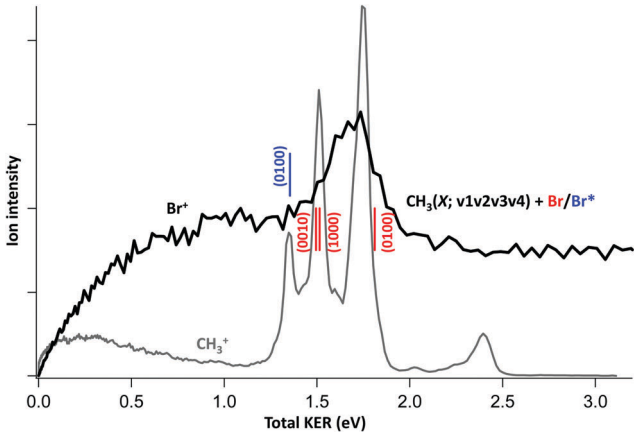

Fig. 5 Br^+ (black, above) and $CH_3{}^+$ (grey, below) kinetic energy release spectra (KERs) as a function of total kinetic energy released. Common energy thresholds for the formation of CH_3(X, $\nu_1\nu_2\nu_3\nu_4$) + Br/Br* after non-resonant one-photon photodissociation of CH_3Br are indicated.

spectra in the two-photon region of 66 019–68 684 cm^{-1} revealed the vibrational constants $\omega_e = 1311 \pm 5$ cm^{-1} and $\omega_e x_e = 11 \pm 1$ cm^{-1} for the out-of-plane (ν_2) vibrational mode of CH_3**($3p^2A_2$). This is to be compared with the vibrational wavenumber value of 1323 cm^{-1} reported for CH_3**($3p^2A_2$) in NIST.[36,37]

Br^+. Br^+ ion slice images were recorded following CH_3Br resonance excitations to Rydberg states in the two-photon excitation region of 66 000–80 000 cm^{-1} listed in Table 1 (except for no. 2/66 503 and no. 6/74 249 cm^{-1}). KERs were derived from the images (see Fig. 4). All the KERs exhibit a broad spectral structure peaking at low kinetic energies in the region of about 0.2 eV KER. The peak shifts to lower KER as the excitation energy increases. An additional broad peak is present at around 1 eV KER for the excitations no. 8/77 165 cm^{-1}, no. 9/78 370 cm^{-1} and no. 10/79 610 cm^{-1} spectra (Fig. 4). For the no. 10/79 610 cm^{-1} spectrum there is also a sharp peak at about 0.27 eV KER.

We attribute the sharp peak in the no. 10/79 610 cm^{-1} KER spectrum to the non-resonant contribution producing Br ground state along with CH_3(X; $\nu_1\nu_2\nu_3\nu_4$) by one-photon dissociation, *i.e.*

$$CH_3Br + 1h\nu \rightarrow CH_3Br^*; \quad \text{non-resonant transition} \quad (3a)$$

$$CH_3Br^* \rightarrow CH_3(X;\ \nu_1\nu_2\nu_3\nu_4) + Br; \quad \text{dissociation} \quad (3b)$$

$$Br + 3h\nu \rightarrow Br^+ + e^-; \quad \text{photoionization} \quad (3c)$$

Comparison of the total KERs (see Fig. 5) derived from the no. 10 images of Br^+ and $CH_3{}^+$ shows a sharp peak for Br to match the strongest sharp peak for CH_3, which corresponds to the formation of CH_3 with one quantum in the umbrella mode (CH_3(X; 0100)).

The broad low kinetic energy peak present in all KERs (Fig. 4) fits energetically the production of Br/Br* along with CH_3** Rydberg states (channels (2a)–(2c)). As discussed for CH_3 this is a three-photon process in two steps: First CH_3Br is excited resonantly with two photons (channel 2a) to a Rydberg state (Table 1), which subsequently absorbs an additional photon towards a superexcited $CH_3Br^{\#}$ state (or states; 2b) dissociating to CH_3** + Br/Br*. The broad, high kinetic energy contribution, only seen in the no. 8/77 165 cm^{-1}, no. 9/78 370 cm^{-1} and no. 10/79 610 cm^{-1} spectra (Fig. 4), on the other hand, is due to Br/Br* formed along with CH_3(X, $\nu_1\nu_2\nu_3\nu_4$) after a three-photon photodissociation process *via* the molecular Rydberg states ((2a) and (2b)). In both cases, Br^+ is subsequently generated by three-photon-MPI of Br/Br*. Relevant energy thresholds for these two processes are shown in Fig. 4 along with the KERs plotted on a $\Delta(3h\nu)*f$(Br) scale.

C. Angular distributions

$CH_3{}^+$. Significant variations in angular distributions are observed for the $CH_3{}^+$ ions depending on the rings/channels involved (see Fig. 2). Signals associated with the resonant excitations mostly display shapes corresponding to parallel or isotropic distributions, whereas those due to the non-resonant excitations are found to display shapes corresponding to both parallel and perpendicular transitions. In an attempt to quantify the anisotropy of the rings, angular distributions, in the form of signal intensities as a function of the angle from 0 to 180°, derived from the images, were fitted by the simplified expression corresponding to a one-step photodissociation,[28]

$$P(\theta) = A[1 + \beta_2 P_2(\cos(\theta)) + \beta_4 P_4(\cos(\theta))] \quad (4)$$

where P_2 and P_4 are the second and fourth order Legendre polynomials and β_2 and β_4 are the corresponding anisotropy

parameters. A is a scaling factor. The β_2 parameter, which can be in the range between +2 (purely parallel transition) and −1 (purely perpendicular transition), can then be related to the overall transition symmetry and the corresponding dynamics. The β_4 parameter is usually associated with vector correlation effects, however considering the complexity of the processes involved (see eqn (1)–(3) above) it is unrealistic to interpret them in this way here, where it is better viewed simply as a fitting parameter. β_2 parameters derived for the various KERs features can be found in the ESI.†[38]

Fig. 6a shows β_2 values plotted for the various rings detected in images no. 8 and 10 (see Table 1) for the non-resonant process. These are shown along with the corresponding KERs plotted on a relative one-photon energy scale. A reasonably good agreement is found between the parameter values derived from the rings/KERs peaks of both images (no. 8 and 10) which have been assigned to common channels (see above), which further supports the validity of the assignments. The β_2's range from a value near +2, corresponding to a purely parallel transition for the CH_3(X; 0100) + Br* intermediates, to a negative value of about −0.2 corresponding to a significant contribution of a perpendicular transition for CH_3(X; 0100) + Br. Positive values of β_2 in the range of +0.8 to +1.6 obtained for CH_3(X; 1000/0010) + Br and high KER hot bands which form CH_3(X; $\nu_1\nu_2\nu_3\nu_4$) + Br suggest dominating parallel transitions mixed with some character of perpendicular transitions. Since the ion formation mechanism involves a simple one-photon photodissociation step, the anisotropy will be largely determined by the symmetry change of the initial photoexcitation step from the ground state of CH_3Br(X; $\nu_1\nu_2\nu_3$) to the repulsive valence states $^3Q_1$, $^3Q_0$ and $^1Q_1$ which correlate with CH_3(X; $\nu_1\nu_2\nu_3\nu_4$) + Br/Br*.[22] Considering symmetry alterations in possible transitions and the known shape of the potential energy surfaces involved[22] the following initial photoexcitation processes are proposed:

(i) Formation of CH_3(X; 0100) + Br*, where CH_3 is vibrationally excited by one quantum in the out-of-plane bending mode (ν_2), mainly occurs by a parallel transition to the $^3Q_0$ state followed by a dissociation on the same (*i.e.* the diabatic) potential curve.

(ii) Formation of CH_3(X; 1000/0010) + Br, where CH_3 is vibrationally excited by one quantum in a stretching mode (ν_1 and/or ν_3), occurs largely by a parallel transition to the $^3Q_0$ state followed by a curve crossing, *i.e.* a dissociation on the adiabatic potential curve.

(iii) Formation of CH_3(X; 0100) + Br, where CH_3 is vibrationally excited by one quantum in the out-of-plane bending mode (ν_2), occurs to a significant extent by perpendicular transitions to the $^3Q_1$ and/or $^1Q_1$ states followed by a dissociation on the same/diabatic potential curve.

(iv) Formation of CH_3(X; $\nu_1\nu_2\nu_3\nu_4$) + Br from vibrationally excited CH_3Br(X; $\nu_1\nu_2\nu_3$) largely occurs by a parallel transition to the $^3Q_0$ state followed by a dissociation on the adiabatic potential curve.

Since the resonant contributions to the CH_3^+ images and KERs mostly involve three-photon excitations *via* molecular Rydberg states prior to dissociation to form CH_3** Rydberg states (channel (2)) the anisotropy of the images will depend on the two-photon resonant step as well as the one-photon dissociation step and possible mixing of states involved. Therefore, it cannot be easily interpreted. We observe a trend (Fig. 6b, grey dots) of decreasing β_2 parameter (more perpendicular contribution) with increasing excitation energy. A correlation with the symmetry of the parent Rydberg state seems to exist: transitions through 5p and 4d Rydberg states of CH_3Br generate CH_3^+ with rather parallel distributions (β_2 ranging between 1.3 and 0.7) whereas 6p and 7p Rydberg states of CH_3Br generate CH_3^+ with almost isotropic distributions.

Br^+. Br^+ images associated with the resonant excitations, both low and high KER components (see above), mostly display shapes corresponding to parallel transitions with positive values of β_2. Fig. 6b (red dots) shows the β_2 values derived for the broad low KER peaks of the resonant transitions along with

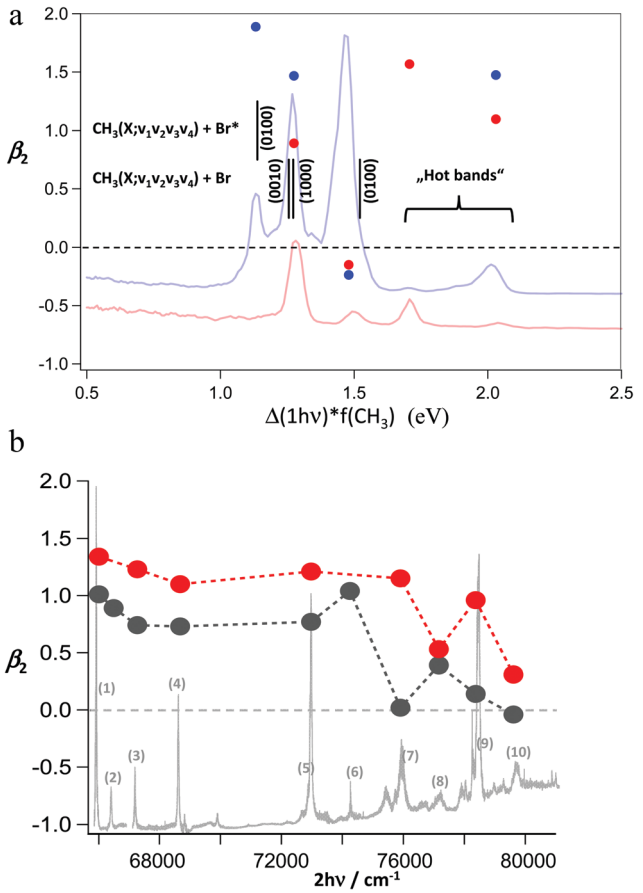

Fig. 6 (a) Effective anisotropy parameters β_2 extracted from CH_3^+ images no. 8 (red dots) and 10 (blue dots) (see Table 1) as a function of the kinetic energy released (eV) along with the corresponding KER spectra plotted on a relative energy scale ($\Delta(1h\nu)*f(CH_3)$) (see main text). Common energy thresholds for one-photon photodissociation processes to form CH_3(X; $\nu_1\nu_2\nu_3\nu_4$) + Br/Br* labelled by ($\nu_1\nu_2\nu_3\nu_4$) are indicated. "Hot bands": see Fig. 3a. (b) Effective anisotropy parameters β_2 extracted from CH_3^+ (grey dots) and Br^+ (red dots) images as a function of two-photon resonant excitations to CH_3Br Rydberg states along with the corresponding CH_3^+ REMPI spectrum. Image numbers are indicated (see Table 1).

the corresponding values for the CH_3^+ signals. Comparison of the β_2 parameters of the signals for Br^+ and CH_3^+ reveals some correlation (common trend and analogous values of β_2) between the signals. This is to be expected for fragments formed by the same channel, prior to ionization, as proposed for CH_3** and Br/Br* (see eqn (2a)–(2c) above). Although close in value they are not identical; this can be attributed to the existence of some additional smaller contributions affecting the CH_3^+ and Br^+ distributions, such as dissociation of CH_3^+ (we do observe CH_2^+, CH^+ and C^+ ions as minor channels; discussion of these results will be dealt with in a separate publication).

The no. 10 excitation Br^+ signal due to the non-resonant transition cannot be separated from the underlying resonant contribution of the same KER (~0.27 eV) which makes up about 2/3 of the signal (Fig. 4 and 5). The total signal however, is found to display a close to isotropic shape (Fig. 2d) with β_2 of about +0.24, suggesting that the non-resonant part of it (1/3 of the total) is significantly perpendicular in nature. This matches the observed angular distribution (and $\beta_2 = -0.2$) of the signal for CH_3^+ due to the formation of the corresponding CH_3(X, 0100) fragment which we believe to be the major fragment produced along with Br prior to ionization (see above and Fig. 5).

C. Photoelectron spectra (PES)

Images of photoelectrons were recorded for the excitations listed in Table 1. No negative ions were found to be present in the time-of-flight KER distributions (Fig. 7) derived from the images. It is convenient to compare the photoelectron spectra with respect to the non-resonant contributions on a relative three-photon energy scale ($\Delta(3h\nu)*f(e)$; $\Delta(3h\nu) = 3h\nu_0 - 3h\nu_i$; $f(e) = m(CH_3^+)/m(CH_3) \sim 1$; see text above for comparison and definitions) and those with respect to the resonant contributions on a relative one-photon energy scale ($\Delta(1h\nu) = 1h\nu_0 - 1h\nu_i$).

Fig. 7a shows the photoelectron spectra plotted on the relative one-photon energy scale, where the zero kinetic energy release of no. 10/79 610 cm^{-1} has been set to zero (reference spectrum). Thresholds corresponding to ionization of specific CH_3** states (formed along with Br/Br*) line up in the plot. One photoelectron peak dominates the four lowest energy excitations (*i.e.* images/KERs no. 1–4; Table 1) which match in Fig. 7a. The peaks correspond to the formation of the CH_3** ($3p^2A_2$) Rydberg state. These PES correspond to the images/KERs which show vibrational structures (see above). Small satellite peaks close by are indicative of vibrational excitations and hot bands as shown in Fig. 7b for excitation no. 4. The next two excitations (no. 5 and 6) generate photoelectron peaks that shift to higher energy but also match each other, corresponding to one-photon ionization of the CH_3** ($3d^2E$) and/or CH_3** ($3d^2A_1$) states, that lie close in energy. Finally, excitations no. 7–10 exhibit several photoelectron peaks corresponding to ionization of different CH_3 Rydberg states ($3p^2A_2$, $3d^2E$, $3d^2A_1$, $4p^2A_2$) as listed in Table 1. The PES structures of no. 8/77 165 and no. 10/79 610 cm^{-1}, which correspond to significant non-resonant contributions, are less clear. However, there are some indications of ionization/formation of CH_3(X; $\nu_1\nu_2\nu_3\nu_4$) species based on weak high kinetic energy electron peaks as shown by the inserted figure expansion for no. 8 in Fig. 7a.

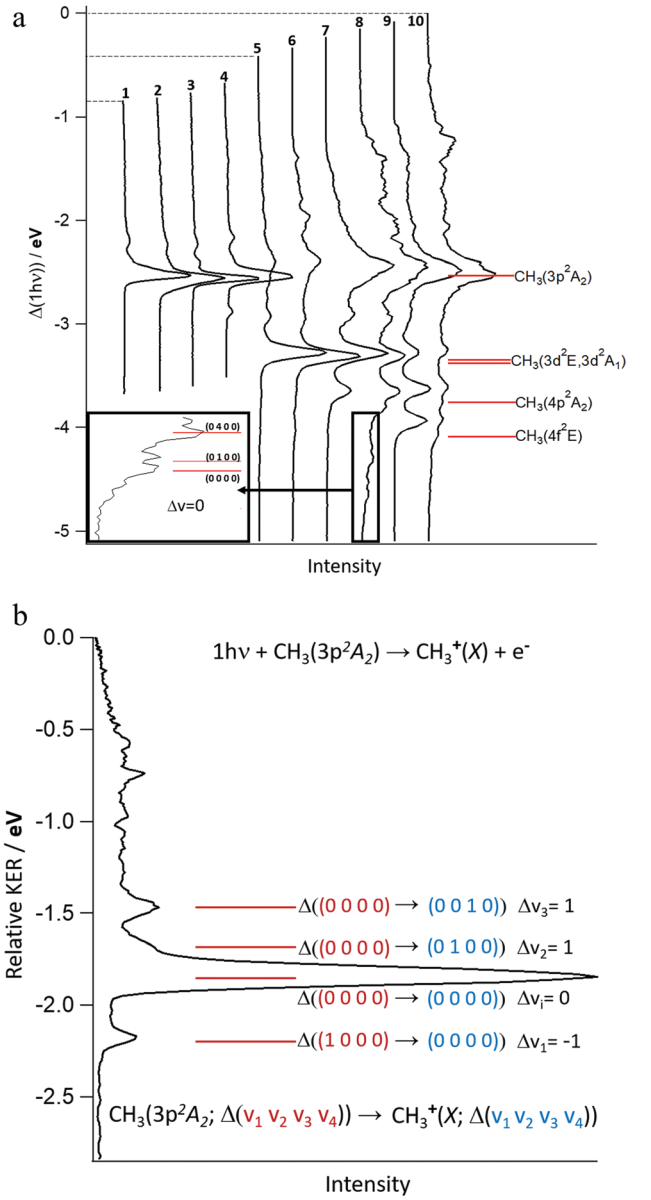

Fig. 7 Photoelectron spectra (PES), (a) derived from images no. 1–10 (see Table 1), plotted as a function of a relative energy scale $\Delta(1h\nu)$ (see explanation in the main text) and tilted to the right (*i.e.* plotted vertically). Common energy thresholds (energy maxima) for ionization of Rydberg states of CH_3 (CH_3**(Ry)) after its formation along with Br/Br* by three-photon photodissociation of CH_3Br are indicated. The inset shows detail of the PES no. (8) at high energy with thresholds for ionization of CH_3(X; $v_1v_2v_3v_4$) and its formation along with Br/Br*. (b) For image no. 4 plotted as a function of the relative kinetic energy released (eV) tilted to the right (*i.e.* plotted vertically). Energy thresholds (energy maxima) for specific one-photon ionization processes of CH_3**($3p^2A_2$; $v_1v_2v_3v_4$) states to form CH_3^+(X; $v_1v_2v_3v_4$), after its formation along with Br/Br* by three-photon photodissociation of CH_3Br, are indicated by ($v_1v_2v_3v_4$) numbers. Assignments of ionization processes with respect to changes in vibrational quantum numbers (Δv_i) are shown, furthest to the right.

IV. Discussion

As noted in the previous section, REMPI, slice and photoelectron imaging data converge on the existence of two major pathways when CH_3Br is excited at wavenumbers corresponding to two-photon transitions to reach rovibrational levels of molecular Rydberg states in the 66 000 to 80 000 cm^{-1} region: (a) two-photon-resonant transitions, followed by one-photon photolysis to give $CH_3(X)/CH_3^{**}$ + Br/Br* and (b) non-resonant, one-photon photolysis towards $CH_3(X)$ + Br/Br*. These two pathways will now be discussed.

A. Resonant processes

The results relevant to the resonant spectra contributions, as presented above, can be interpreted as being due to dissociations on excited state potential energy surfaces to form (a) Rydberg states of CH_3 (CH_3^{**}) along with Br/Br* or (b) ground state $CH_3(X)$ along with Br/Br* prior to ionization of either CH_3 or Br. This occurs after a total of three-photon excitation to metastable superexcited molecular states ($CH_3Br^{\#}$) *via* two-photon accessible Rydberg states (Fig. 8). Formation of $CH_3(X)$ directly following the two-photon resonant excitation (*i.e.* by predissociation of the resonance-excited molecular Rydberg states) was not detected. Whereas a minor contribution of such a channel cannot be ruled out, the results suggest that its probability is low.

In the case of the metastable molecular state(s) ($CH_3Br^{\#}$), prior to a dissociation the excess energy can be redistributed among the molecule's internal degrees of freedom to form fragments of relatively low translational energy but high internal (ro-vibrational) energy, typically appearing as broad KER spectral peaks for the CH_3 and Br fragments. The relatively low KER, broad spectral structures of the KERs observed for the resonant contributions suggests that step (2b) involves such a mechanism. The $CH_3Br^{\#}$ state(s), being higher in energy than the ionization limit, is (are) most likely one or more superexcited state(s) belonging to a Rydberg series converging to an excited ionic state (*i.e.* $CH_3Br^{\#} = [CH_3Br^{+*}]nl;\omega$). This involves a one-photon excitation within the ion core of the resonant Rydberg state ($CH_3Br^{**} = [CH_3Br^{+}]nl;\omega$) to make an overall two-electron transfer to form $CH_3Br^{\#}$.

Looking at a summary of the CH_3^{**} Rydberg states detected (Table 1) there seems to be a correlation between the formation of CH_3^{**}(Ry) and excitations to CH_3Br^{**}(Ry) with respect to the Rydberg electron orbital symmetries (l quantum numbers). Thus, the 3p Rydberg state of CH_3 ($CH_3^{**}(3p^2A_2)$) is primarily

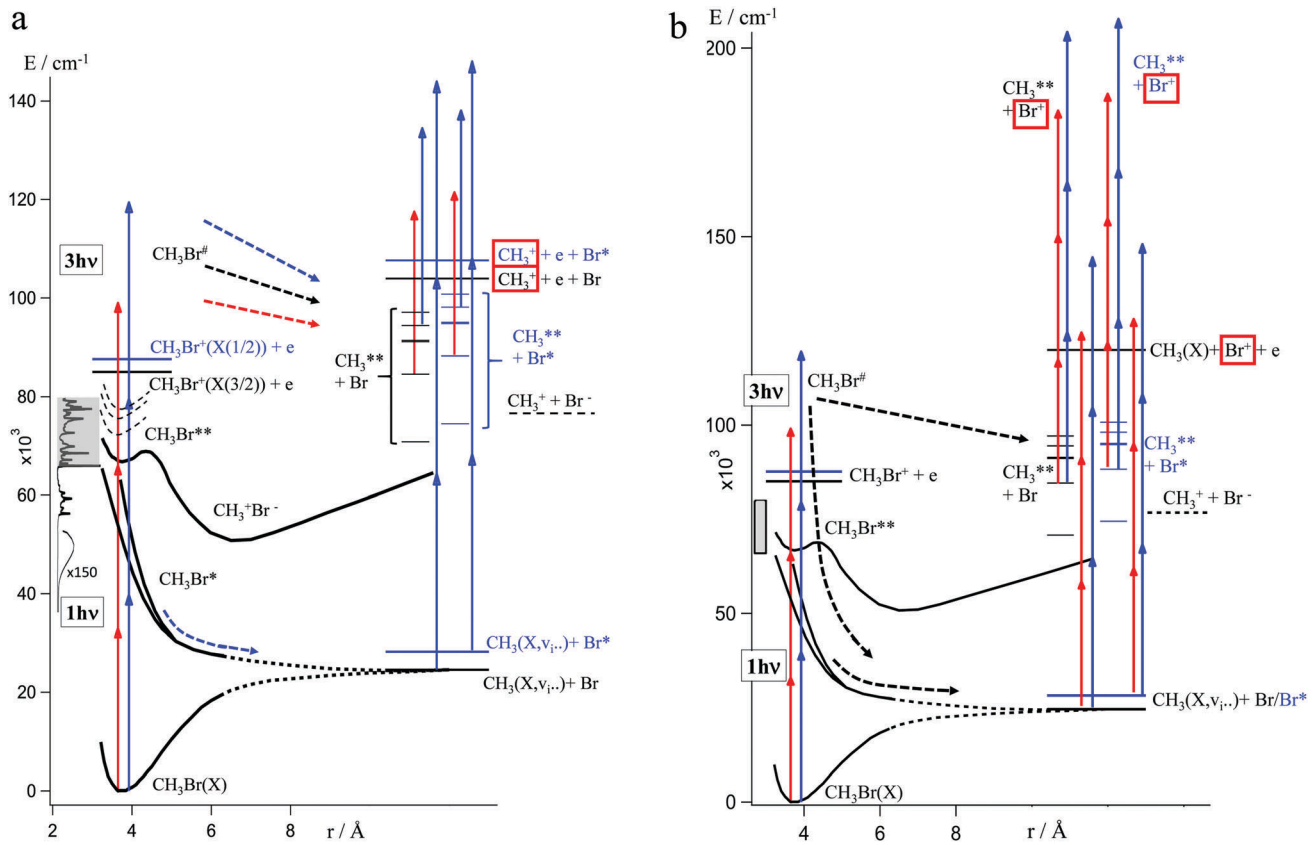

Fig. 8 Schematic energy diagrams for excitation processes of CH_3Br leading to CH_3^+ (a) and Br^+ (b) formation showing calculated potential energies as a function of the CH_3–Br bond distance[18,27] as well as relevant energy thresholds and transitions. Red vertical arrows correspond to the two-photon resonant transition of 66 019 cm^{-1} (excitation no. 1) and blue vertical arrows correspond to the two-photon resonant transition 79 610 cm^{-1} (excitation no. 10) (see Table 1). Broken arrows indicate paths of photodissociation processes as marked in boxes (see main text). The two-photon resonance scanning region is indicated by grey shaded boxes. The one-photon absorption spectrum[3,9] is tilted to the right (*i.e.* plotted vertically) in figure (a).

formed *via* excitation to the 5p Rydberg state of CH_3Br and the 3d Rydberg state(s) of CH_3 (CH_3**(3d^{2}E; 3d^{2}A$_1$)) is (are) largely formed *via* excitation to the 4d Rydberg state of CH_3Br. This must be associated with a conservation of momentum during the combined process of one-photon excitation of CH_3Br** to $CH_3Br^{\#}$ and its dissociation on an excited state potential surface to form CH_3** and Br/Br*. Furthermore, an increasing number and changing proportion of CH_3** states are formed as the excitation energy increases (Table 1 and Fig. 7a). This must be associated with an opening of an increasing number of channels to form CH_3** + Br/Br* and/or changes in transition probabilities along different surfaces as the energy increases. The disappearance of the vibrational structure assigned to the CH_3**(3p^{2}A$_2$) state (see Section III.B) for excitation energies beyond that for no. 4 (Fig. 3) is a further indication of an increasing contribution of CH_3** states and overlapping vibrational structures.

Whereas, no multiphoton dissociation studies for resonant excitations *via* p and d Rydberg states of CH_3Br exist in the literature, Wang *et al.* have reported studies of excitations *via* lower energy 5s Rydberg states.[19] Images and corresponding KERs for CH_3^+ are found to show comparable structures to those reported here, appearing as broad peaks with vibrational structures at low KERs and sharp peaks at medium high kinetic energies. These observations, however, are interpreted differently as being due to photodissociation of the parent molecular ions CH_3Br^+(X) to form CH_3^+(X) along with Br* and Br, respectively. Furthermore, rings/sharp KER peaks observed at still higher KERs are proposed to be due to two-photon resonant photodissociations to form CH_3(X) along with Br and Br*.

B. Non-resonant processes

The results relevant to the non-resonant contributions, as presented above, can be interpreted as being due to one-photon excitations to repulsive electronic valence states (CH_3Br*) followed by dissociation. This agrees with the observed increase in the corresponding spectral continuum with photon energy (Fig. 1a) in accordance with an increasing absorption (*i.e.* one-photon) cross section in the excitation region (see Fig. 8).[3,9] Relatively large signals appearing as rings in the images/sharp KERs peaks, due to the non-resonant contributions were seen for the excitations which show relatively large underlying non-resonant contributions in the REMPI spectra (see Fig. 1a), *i.e.* in images/KERs no. 8 and 10 for CH_3^+ (Fig. 3) and in no. 10 for Br^+ (Fig. 4).

Photodissociation studies in the first continuum absorption band (A band) of CH_3Br have been performed by a number of groups.[13–15,21–24] The reported value for β_2 of 1.9 ± 0.1 for CH_3(X; 0100) formation along with Br* for 251.00 nm excitation[22] agrees with our value (1.9) for the corresponding fragment formation for 251.28 nm one-photon excitation (no. 10/79 610 cm^{-1}) and the value for β_2 of 0.2 ± 0.2 for CH_3(X; 0100) along with Br for 251.00 nm excitation[22] is of an intermediate size analogous to our values of −0.15 and −0.24 for the corresponding fragment formation derived for the 259.23 (no. 8/77 165 cm^{-1}) and 251.28 nm (no. 10/79 610 cm^{-1}) excitations, respectively. Furthermore, our upper limit value of β_2 = +0.24, largely due to the formation of Br along with CH_3(X; 0100) (see Section III.C) for 251.28 nm one-photon excitation can be compared with the values of about zero for excitations in the region of 251–278 nm.[22] Thus, the formation of CH_3(X) in the out-of-plane bending mode along with Br is found to display isotropic to perpendicular fragment angular distributions, whereas its formation along with Br* displays a parallel angular distribution. This is in agreement with previous observations and has been shown to be consistent with a strong non-adiabatic coupling between spin–orbit states of the parent molecule.[22]

V. Summary and conclusions

CH_3^+ and Br^+ ion slice images as well as photoelectron velocity map images were recorded for multiphoton excitation of CH_3Br at ten wavelengths involving two-photon – resonant transitions to np and nd vibrational levels of molecular Rydberg states (CH_3Br**(Ry; $\nu_1\nu_2\nu_3$)) between 66 000 and 80 000 cm^{-1} (Table 1). At all wavelengths CH_3^+ is the majority of the ion signal (Fig. 1). Kinetic energy release spectra (KERs) as well as angular distributions and relevant fit parameters (β_2 and β_4) were derived from the ion slice images. Photoelectron spectra were derived from the photoelectron images.

The majority of the photoelectrons formed are due to one-photon ionization of different Rydberg states of methyl photofragments (CH_3**). These states are formed by two-photon-resonant excitation to an np or nd vibrational levels of parent Rydberg states followed by one-photon excitation to metastable, superexcited molecular states ($CH_3Br^{\#}$) which then dissociate towards CH_3**(Ry; $\nu_1\nu_2\nu_3\nu_4$) + Br/Br*. This contribution dominates all but two excitation wavelengths used in this work. A correlation is found between the angular momentum quantum numbers (l) of the resonantly excited molecular Rydberg states, CH_3Br** and the CH_3 Rydberg states formed.

For the highest excitation energies, two additional channels are found to be present. The first channel is a dissociation of the metastable, superexcited $CH_3Br^{\#}$ states towards CH_3(X; $\nu_1\nu_2\nu_3\nu_4$) + Br/Br* which generates fast CH_3^+ and Br^+ ions. The second channel is the formation of CH_3(X; $\nu_1\nu_2\nu_3\nu_4$) + Br/Br* assigned as a one-photon photolysis *via* the A band with angular distributions of CH_3 and Br/Br* fragments agreeing well with the literature.

The results of this paper add to information relevant to the energetics and fragmentation processes of the methyl halides. It will hopefully render further theoretical interpretation of the characteristic processes involved in the very interesting dynamics observed here. Furthermore, the content of this paper is of relevance to various intriguing fields. The observed involvement of high energy superexcited molecular states in the formation of halogen atom radicals and fragment ions and electrons is of relevance to further understanding of atmospheric photochemistry as well as plasma chemistry/physics. Selective photoexcitation to form the reactive electronically

excited state of the CH_3, as identified, could be of interest for organic photosynthesis purposes.

Conflicts of interest

There are no conflicts to declare.

Acknowledgements

The financial support of the University Research Fund, University of Iceland is gratefully acknowledged. The imaging part of the reported results was carried out at the Ultraviolet Laser Facility at IESL-FORTH, supported in part by the European Union's Horizon 2020 research and innovation programme LASERLAB-EUROPE (Grant Agreement No. 654148).

References

1 D. E. Robbins, Photodissociation of Methyl-Chloride and Methyl-Bromide in Atmosphere, *Geophys. Res. Lett.*, 1976, **3**(4), 213–216.
2 D. E. Robbins, Correction, *Geophys. Res. Lett.*, 1976, **3**(12), 757.
3 L. T. Molina, M. J. Molina and F. S. Rowland, Ultraviolet-Absorption Cross-Sections of Several Brominated Methanes and Ethanes of Atmospheric Interest, *J. Phys. Chem.*, 1982, **86**(14), 2672–2676.
4 N. J. Warwick, J. A. Pyle and D. E. Shallcross, Global modelling of the atmospheric methyl bromide budget, *J. Atmos. Chem.*, 2006, **54**(2), 133–159.
5 Ozone-Depleting Substances. https://www.epa.gov/ozone-layer-protection/ozone-depleting-substances.
6 W. C. Price, The Far Ultraviolet Absorption Spectra and Ionization Potentials of the Alkyl Halides. Part I, *J. Chem. Phys.*, 1936, **4**(9), 539–547.
7 G. C. Causley and B. R. Russell, Vacuum Ultraviolet-Absorption Spectra of Bromomethanes, *J. Chem. Phys.*, 1975, **62**(3), 848–857.
8 S. Felps, P. Hochmann, P. Brint and S. P. McGlynn, Molecular Rydberg Transitions; The lowest-Energy Rydberg Transitions of s-Type in CH_3X and CD_3X, X = Cl, Br, and I, *J. Mol. Spectrosc.*, 1976, **59**, 355–379.
9 R. Locht, B. Leyh, H. W. Jochims and H. Baumgartel, The vacuum UV photoabsorption spectrum of methyl bromide (CH_3Br) and its perdeuterated isotopomer CD_3Br: a Rydberg series analysis, *Chem. Phys.*, 2005, **317**(1), 73–86.
10 R. Locht, B. Leyh, D. Dehareng, H. W. Jochims and H. Baumgartel, The vacuum UV photoabsorption spectrum of methyl bromide (CH_3Br) and its perdeuterated isotopomer CD_3Br: a vibrational analysis, *Chem. Phys.*, 2005, **317**(1), 87–102.
11 A. Kvaran, H. Wang, K. Matthiasson and A. Bodi, Two-Dimensional (2 + n) REMPI of CH_3Br: Photodissociation Channels via Rydberg States, *J. Phys. Chem. A*, 2010, **114**, 9991–9998.
12 G. N. A. Van Veen, T. Baller and A. E. De Vries, Photofragmentation of CH_3Br in the A-Band, *Chem. Phys.*, 1985, **92**(1), 59–65.
13 W. P. Hess, D. W. Chandler and J. W. Thoman, Photofragment imaging: the 205 nm photodissociation of CH_3Br and CD_3Br, *Chem. Phys.*, 1992, **163**(2), 277–286.
14 T. Gougousi, P. C. Samartzis and T. N. Kitsopoulos, Photodissociation study of CH_3Br in the first continuum, *J. Chem. Phys.*, 1998, **108**(14), 5742–5746.
15 V. Blanchet, P. C. Samartzis and A. M. Wodtke, UV photodissociation of methyl bromide and methyl bromide cation studied by velocity map imaging, *J. Chem. Phys.*, 2009, **130**, 3.
16 D. A. Shaw, D. M. P. Holland and I. C. Walker, Ion-pair formation mechanisms in chloromethane, bromomethane and dichlorodifluoromethane, *J. Phys. B: At., Mol. Opt. Phys.*, 2006, **39**(17), 3549–3560.
17 D. D. Xu, J. H. Huang, R. J. Price and W. M. Jackson, Velocity Imaging Studies on Ion-Pair Dissociation of CH_3Br + $h\nu_{VUV} \rightarrow CH_3^+ + Br^-$ as a Function of Wavelength, *J. Phys. Chem. A*, 2004, **108**(45), 9916–9923.
18 C. Escure, T. Leininger and B. Lepetit, Ab initio study of methyl-bromide photodissociation in the A band, *J. Chem. Phys.*, 2009, **130**(24), 244305.
19 F. Y. Wang, M. L. Lipciuc, X. M. Yang and T. N. Kitsopoulos, Multiphoton dissociation dynamics of CH_3Br, *Phys. Chem. Chem. Phys.*, 2009, **11**(13), 2234–2240.
20 T. Ridley, J. T. Hennessy, R. J. Donovan, K. P. Lawley, S. Wang, P. Brint and E. Lane, Evidence for Rydberg doorway states in photoion pair formation in bromomethane, *J. Phys. Chem. A*, 2008, **112**(31), 7170–7176.
21 G. N. A. Vanveen, T. Baller and A. E. Devries, Photofragmentation of Ch_3Br in the A-Band, *Chem. Phys.*, 1985, **92**(1), 59–65.
22 J. G. Underwood and I. Powis, Photofragmentation of CH_3Br in red wing of the first continuum absorption band, *Phys. Chem. Chem. Phys.*, 2000, **1**, 747–756.
23 F. Y. Wang, M. L. Lipciuc, A. Kartakoullis, P. Glodic, P. C. Samartzis, X. M. Yang and T. N. Kitsopoulos, Slice imaging of methyl bromide photofragmentation at 193 nm, *Phys. Chem. Chem. Phys.*, 2014, **16**(2), 599–606.
24 M. L. Lipciuc and M. H. M. Janssen, High-resolution slice imaging of quantum state-to-state photodissociation of methyl bromide, *J. Chem. Phys.*, 2007, **127**, 224310.
25 Y. Song, X. M. Qian, K. C. Lau, C. Y. Ng, J. B. Liu and W. W. Chen, High-resolution energy-selected study of the reaction $CH_3X^+ \rightarrow CH_3^+ + X$: Accurate thermochemistry for the CH_3X/CH_3X^+ (X = Br, I) system, *J. Chem. Phys.*, 2001, **115**(9), 4095–4104.
26 X. Tang, X. Zhou, Z. Sun, S. Liu, F. Liu, L. Sheng and B. Yan, Dissociation of internal energy-selected methyl bromide ion revealed from threshold photoelectron-photoion coincidence velocity imaging, *J. Chem. Phys.*, 2014, **140**, 044312.
27 C. Escure, T. Leininger and B. Lepetit, Ab initio study of valence and Rydberg states of CH_3Br, *J. Chem. Phys.*, 2009, **130**(24), 244306.

28 H. R. Hrodmarsson, A. Kartakoullis, D. Zaouris, P. Glodic, H. Wang, P. C. Samartzis and A. Kvaran, Excitation Dynamics Involving Homogeneous Multistate Interactions: One and Two Color VMI and REMPI of HBr, *Phys. Chem. Chem. Phys.*, 2017, **19**(18), 11354–11365.
29 H. R. Hrodmarsson and Á. Kvaran, Revealing photofragmentation dynamics through interactions between Rydberg states: REMPI of HI as a case study, *Phys. Chem. Chem. Phys.*, 2015, **17**, 32517.
30 H. R. Hrodmarsson, H. Wang and A. Kvaran, State interactions and illumination of hidden states through perturbations and observations of new states: High energy resonance enhanced multiphoton ionization of HI, *J. Chem. Phys.*, 2015, **142**(24), 244312.
31 J. Long, H. Wang and A. Kvaran, Phtofragmentation, state interactions, and energetics of Rydberg and ion-pairstates: Resonance enhanced multiphoton ionization via E and V(B) states of HCl and HBr, *J. Chem. Phys.*, 2013, **138**(4), 044308.
32 P. Glodic, D. Zaouris, P. C. Samartzis, A. Hafliðason and Á. Kvaran, Effect of a triplet to singlet interaction on photofragmentation dynamics: Highly excited states of HBr probed by VMI and REMPI as a case study, *Phys. Chem. Chem. Phys.*, 2016, **18**(37), 26291–26299.
33 D. Zaouris, A. Kartakoullis, P. Glodic, P. C. Samartzis, H. R. Hrodmarsson and A. Kvaran, Rydberg and valence state excitation dynamics: a velocity map imaging study involving the E-V state interaction in HBr, *Phys. Chem. Chem. Phys.*, 2015, **17**(16), 10468–10477.
34 C. R. Gebhardt, T. P. Rakitzis, P. C. Samartzis, V. Ladopoulos and T. N. Kitsopoulos, Slice Imaging: A New Approach to Ion Imaging and Velocity Mapping, *Rev. Sci. Instrum.*, 2001, **72**(10), 3848.
35 V. Papadakis and T. N. Kitsopoulos, Slice Imaging and Velocity Mapping Using a Single Field, *Rev. Sci. Instrum.*, 2006, **77**(8), 5.
36 B. Zhang, J. Zhang and K. Liu, Imaging the ''missing'' bands in the resonance-enhanced multiphoton ionization detection of methyl radical, *J. Chem. Phys.*, 2005, **122**, 104310.
37 NIST Chemistry WebBook - (National Institute of Standards and Technology) https://webbook.nist.gov/chemistry/name-ser/, accessed Jan 2018.
38 See ESI†.